I. Structure-Function Analysis of the Mechanosensitive Channel of Large Conductance. II. Design of Novel Magnetic Materials using Crystal Engineering.

Thesis by

Joshua Ahab Maurer

In Partial Fulfillment of the

Requirements for the Degree of

Doctor of Philosophy

California Institute of Technology

Pasadena, California

2003

(Defended October 2, 2002)

in memory of Teresa Hsu

Acknowledgments

The Dougherty group has been a great place to be over the past six years. As an advisor, Dennis Dougherty has given me the freedom to explore and learn many different things from physical organic chemistry to molecular biology and biochemistry. His direction has taught me how to think about problems and find solutions. Collaboration with Henry Lester on the MscL projects has lead to a wealth of new ideas and different perspectives. He provides the prospective of a biologist and physiologist, which is often necessary as our work leads us from chemistry into these uncharted waters. I have also had the good fortune of working with Doug Rees and Gred Kochendoerfer on the MscL project. Additionally, over the past year or so I have had the opportunity to work with Jay Nadeau and Victor White at JPL doing things that we could never do without their expertise. My committee, Bob Grubbs, Jackie Barton, Dave Tirrell, and Mark Davis. has provided support and direction over the years.

Over the past six years I have been fortunate to work with a large number of really great people and have made a lot of friends. If it were not for the resources in the Lester group many things could not have been accomplished; I am particularly thankful to Purnima Deshpande, Shannan Boss, Vanna Santoro, George Shapovalov, and Kira Kostenko, who have provided many of the resources necessary to do the biology that has been required on day to day basis over the years. The Dougherty group has been filled with a large number of amazing people. Seth Miller helped me get started in the group and was a invaluable resource in my early years at Caltech. Jeff Clites and Jesse Lin rounded out the magnets group and were remarkable people with whom to interact. Scott Silverman,

Anthony West, Wenge Zhong, and Jennifer Ma made the group an enjoyable place to work in my early days. Sarah Ngola was an awesome person with whom to share the back of 256 Cr. Pam England helped me get started in biology. Justin Gallivan and I have spent much time talking with over the years. Marcus Sarofim helped to develop my favorite alphabet game. Lintong Li showed me what the proposal and thesis process would be like, by going through it first. Niki Zacharais has been a fun person with whom to interact. David Dahan has proven that Canadians can be cool. Darren Beene really knows his way around a list and has some pretty cool cats. James Petersson is a really great guy. Steve Spronk knows anything that you want to know (or don't want to know) about sports. Sarah Monahan has a voracious love of science. Tingwei Mu is starting to know his way around the group. I am sure that the Dougherty group will continue to be a great place with the recent arrival of Amanda Cashin, Michael Torrice, Jordan Benjamin, and Lori Lee. I owe a debt of gratitude to Gabe Brandt, with whom I have spent much time commiserating about the process of leaving the Dougherty group. He literally knows something about everything has been a tremendous help to me over the years. Don Elmore has not only been a great collaborator, but also a great friend. He has made much of the MscL project possible. Without his help I don't think that we would have gotten anywhere near as far as we have. He is responsible for much of the work in Chapters 2 and 5.

The chemistry department at Caltech would not function if it were not for the wonderful support staff. I am extremely grateful to Linda Syme, Dian Buchness, Chris Smith, Steve Gould, Debbie Miles, Paul Carroad, and Tom Dunn who have helped me tremendously.

In addition to the wonderful people that have made the Caltech chemistry and Dougherty group a great place to be, many other people have helped me to keep my sanity during my graduate career. I am grateful to Julia Prentice for providing hours of non-scientific fun. I have also enjoyed visits with Chrystena Ewen, Karen Maxcy, and Jim Jeitler over the years.

Finally, I am extremely grateful to my parents, who have always been supportive and helpful.

Abstract

The ability to crystallize and structurally characterize ion channels has made it possible to consider the molecular motions involved in gating these channels. The crystal structure of the mechanosensitive channel of large conductance from *M. tuberculosis* (Tb-MscL) has provided new opportunities to explore mechanosensitive channel function, by providing a high resolution image of the closed state of the channel. The first section of this work describes progress towards the functional characterization of the molecular motions involved in channel gating. A general background to the approaches employed here is given in Chapter 1.

In Chapter 2, sequence analysis of 35 putative MscL homologues was used to develop an optimal alignment for *E. coli* and *M. tuberculosis* MscL and to place these homologues into sequence subfamilies. Using this alignment, previously identified *E. coli* MscL mutants, which displayed severe and very severe gain of function phenotypes, were mapped onto the *M. tuberculosis* MscL sequence. Not all of the resulting *M. tuberculosis* mutants displayed a gain of function phenotype; for instance, normal phenotypes were noted for mutations at A20, the analogue of the highly sensitive G22 site in *E. coli*. A previously unnoticed intersubunit hydrogen bond in the extracellular loop region of the *M. tuberculosis* MscL crystal structure has been analyzed. Cross-linkable residues were substituted for the residues involved in the hydrogen bond, and cross-linking studies indicated that these sites are spatially close under physiological conditions. In general, mutation at these positions results in a gain of function phenotype, which provides strong

evidence for the importance of the loop region in MscL channel function. No analogue to this interesting interaction could be found in *E. coli* MscL by sequence alignment. Taken together, these results indicate that caution should be exercised in using the *M. tuberculosis* MscL crystal structure to analyze previous functional studies of *E. coli* MscL.

A novel fluorescence-based screen for bacterial mechanosensitive ion-channel activity is developed in Chapter 2. This assay is capable of clearly distinguishing the previously observed gain of function and loss of function phenotypes for the *E. coli* mechanosensitive channel of large conductance (Ec-MscL). The method modifies Molecular Probes' Live/Dead® *Bac*Light™ bacterial viability assay to monitor MscL channel activity as a function of bacterial survival from osmotic downshock.

Chapter 3 describes the random mutagenesis of the mechanosensitive channel of large conductance from *E. coli* coupled with the high-throughput functional screen developed in Chapter 2. This mutagenesis and screening has provided new insights into channel structure and function. Complementary interactions of conserved residues proposed in a computational model for gating have been evaluated, and important functional regions of the channel have been identified. Mutational analysis shows that the proposed S1 helix, despite having several highly conserved residues, can be heavily mutated without significantly altering channel function. The pattern of mutations that make MscL more difficult to gate suggests that MscL senses tension with residues located near the lipid

headgroups of the bilayer. The range of phenotypical changes seen has implications for a proposed model for the evolutionary origin of mechanosensitive channels.

Chapter 5 further investigates structure-function relationships in the mechanosensitve channel of large conductance from *M. tuberculosis*. Intracellular domains are a common regulatory motif among eukaryotic ion channels. Here, we show that the carboxyl terminal domain of the mechanosensitive channel of large conductance from *M. tuberculosis* is such a regulatory domain. A combination of structural stability, measured by circular dichroism thermal denautration, and channel function, measured by *in vivo* channel assays, were used to characterize multiple single point mutations in both the *E. coli* MscL and Tb-MscL carboxyl terminal regions. As seen previously for other regions of the channel, this work clearly highlights differences between the two channel homologues, as the carboxyl terminal domain plays no functional role in Ec-MscL. Recent Tb-MscL gating models have ignored this region of the channel, however these studies clearly indicate that the carboxyl terminus plays a central role in channel gating and therefore should be incorporated into gating models.

The second section of this work describes attempts to develop novel molecular magnetic materials using a variety of approaches. These approaches and a background to molecular magnetism are described in Chapter 6.

In chapter 7, a new class of magnetic materials that was prepared using the guanidinium sulfonate motif and 5,5'-salendisulfonic acid is described. These materials exhibit

massive magnetic frustration. The copper-manganese material has been extensively characterized using dc magnetic analysis and displays the classic signs of magnetic frustration. Although it is difficult to quantitate the extent of frustration in this system, the copper-manganese complex seems to display significant long-range frustration. The generality of the guanidinium sulfonate motif, using 5,5'-salen disulfonic acid as a bridging sulfonate, for the formation of magnetically frustrated materials was verified by the creation of family of six different magnetically frustrated bimetallic complexes.

Table of Contents

List of figures

Chapter 1: Introduction to the Mechanosensitive Channel of Large Conductance

1.1 Using Bacterial Ion Channels as Models for Eukaryotic Ion Channels

Understanding how the human mind works remains a major challenge in many fields. At the chemical and biological level it has been said that, " The human brain is … the most complex structure, natural or artificial, on earth" (Green et al., 1998). Only in the past 50 years have we even begun to understand on the chemical level, what molecules are involved in neurobiology. Currently, the forefront of molecular neurobiology is busy mapping an enormous number of signaling and regulatory pathways.

As chemists, we look to understand the molecular mechanisms than underlie these complex pathways. The proteins of neurobiology provide complex and interesting targets to be understood at the chemical level. Understanding these molecules is an interesting and important feat within itself; however, it also allows us opportunities to develop new and specific pharmaceuticals.

Ion channels are one of the major classes of molecules involved in molecular neurobiology. These molecules are capable of converting an external stimulus into an electrochemical gradient. Ion channels open a pore in the cell membrane in response to large variety of stimuli, including external or internal application of agonist molecules, an electrical field, and mechanical stress. The pores that are opened are then capable of selectively letting molecules or ions in or out of the cell and also distinguishing between cations and anions.

Ion channels have received a great deal of attention over the past few years, since they have been implicated to play critical roles in many genetic and neurodegenerative diseases, including MS, epilepsy, Alzheimer's, Parkinson's, and schizophrenia (Barchi, 1998; Paterson and Nordberg, 2000). Much of the focus has been on finding pharmaceuticals that modulate the behavior of these channels.

In the process of trying to understand ion channels, good experimental systems have been developed to study ion channel proteins and many important ion channels have been cloned. Today, even the most complex ion channels can be routinely expressed in model systems, such as *Xenopus* oocytes, and their properties monitored electrophysiologically.

Understanding the structure and function of these channels is critical for developing an understanding of neurobiology and for development effective drugs. Traditionally, chemists have approached understanding structure-function relationships in these channels by developing pharmacological models, and molecular neurobiologist have approached understanding structure-function relationships in these channels through detailed electrophysiological analysis and mutational analysis. Recently, the Dougherty/Lester labs have developed more subtle ways to probe structure-function relationships in ion-channels using *in vivo* unnatural amino acid mutagenesis (Dougherty, 2000).

Ion-channel structure-function is hindered by the lack of high-resolution structures for these proteins. For many classes of proteins good atomic resolution structures exist, which are invaluable for understanding how these proteins function at the molecular level. However, for the ion-channels, which are important in mammalian neurobiology, no complete atomic resolution structures exist. Recently several extracellular domains of these channels and related proteins have been crystallized (Armstrong and Gouaux, 2000; Armstrong et al., 1998; Brejc et al., 2001), which have both confirmed many of the observations determined mutagenically and electophysiologically, and opened new doors for structure-function analysis.

In 1998, the first atomic resolution structures of bacterial ion-channels were determined (Chang et al., 1998; Doyle et al., 1998). Traditionally, these channels have received less attention than their eukaryotic counterparts; however, they are capable of serving as model systems for eukaryotic ion channels. In general, bacterial ion channels are physically smaller and considerably less complicated than eukaryotic ion channels. This makes them particularly amenable to biochemical and biophysical studies.

High-resolution structure of bacterial ion channels was possible because these channels can be easily overexpressed and purified in milligram quantities. Since 1998, four bacterial ion-channel crystal structures have been determined; three closed-state structures and one open state structure. The closed-state structures are for a potassium channel (Doyle et al., 1998), a chloride channel (Dutzler et al., 2002), and a mechanosensitive channel (Chang et al., 1998), and the open state structure is for a

potassium channel (Jiang et al., 2002a; Jiang et al., 2002b). These structures have provided new insights into how ion channels function.

These atomic resolution structures raise the question of whether structure is sufficient to understand ion-channel function, especially for the case of potassium channels, where both closed and open state structures are known. Clearly the answer to this is no, since function is a dynamic process and the obtained structures are static pictures. These structures, however, provide a platform from which biochemical and biophysical studies can be used gain a complete picture of ion-channel function.

With some structures in hand, it may be possible to gain a complete picture of how bacterial ion channels function. Although these channels are less complicated than their eukaryotic homologues, it is clear that some functional aspects are conserved between prokaryotic and eukaryotic ion channels. Understanding bacterial ion channel function will lead to a better functional understanding of the ion channels involved in mammalian neural biology.

In the remaining chapters of this section, detailed biochemical and biophysical studies on the mechanosensitive channel of large conductance (MscL) will be described. The *M. tuberculosis* homologue of this channel is one of the first bacterial ion channel high-resolution structures to be determined, and the studies described here are based on that structure. The remaining portion of this chapter provides a brief introduction to MscL and its structure.

1.2 The Mechanosensitive Channel of Large Conductance

1.2.1 Mechanosensation

Mechanosensation is a critical function of all organisms from single celled bacteria to humans (Hamill and McBride, 1993; Hamill and McBride, 1994; Hamill and McBride, 1996). Clearly the purpose of mechanosensation varies from organism to organism; however, some similarities exist in the mechanisms of mechanosensation. Mechanosensitive ion channels in all organisms are capable of converting a mechanical stimulus into an electrical signal. These channels work by sensing a force applied to a cellular membrane.

The actual roles of mechanosensitive ion channels vary from organism to organism. In humans, mechanosensitive ion channels play many critical roles. These channels are responsible for such varied tasks as blood pressure regulation and pain sensation (Hamill and McBride, 1994). Proprioception and gravitropism are major roles of mechanosenstive ion channels in plants (Hamill and Martinac, 2001). Bacteria utilize mechanosensitive channels to senses changes in their osmotic environments and prevent bursting upon osmotic downshock (Wood, 1999).

A major breakthrough in the field of mechanosensation occurred in 1994 when the bacterial mechanosensitive channel of large conductance was cloned (Sukharev et al., 1994). Although mechanosensitive ion channels from a large number of organisms had been observed by patch clamp analysis, no specific molecules of mechanosensation were

known. The first mammalian mechanosensitive ion-channel, TREK-1, was cloned in 1996 (Fink et al., 1996).

1.2.2 Pre-structural Analysis MscL

The mechanosensitive channel of large conductance is one of three mechanosensitive ion channels that have been identified electrophysiologically in bacteria. These channels were named according to their observed single channel conductances. Channels with a conductance greater than 1 nS were termed mechanosensitive channels of large conductance (MscL), channels with conductances between 0.3 nS and 0.5 nS were termed mechanosenstive channels of small conductance (MscS), and channels with conductances between 0.1 and 0.15 nS were termed mechanosenstive channels of mini conductance (MscM) (Martinac et al., 1987). MscS (YggB) was cloned by the Booth labs in 1999 and is the gene product of the yggb ORF in *E. coli* (Levina et al., 1999).

MscL was first identified by the Alder and Kung labs in 1987, using a modification of the patch clamp technique that allowed them to patch clamp the periplasmic membrane of *E. coli* (Martinac et al., 1987). The Kung labs subsequently cloned MscL by generating enriched active membrane fractions and obtaining a partial protein sequence that was then used to fish out the MscL gene (Sukharev et al., 1994). Since its initial cloning from *E. coli*, eight MscL homologues have been cloned and characterized by electrophysiology (Moe et al., 1998; Moe et al., 2000). Additionally, over thirty other homologues have been identified by sequence analysis (Maurer et al., 2000).

Even prior to a high-resolution structure, detailed electrophysiology and biochemical analysis provided useful information about the structure and function of MscL. Electrophysiology on isolated protein that was purified and reconstituted into lipid vesicles showed that MscL is necessary and sufficient to achieve channel activity in response to bilayer tension (Figure 1.1) (Sukharev et al., 1994). The tension required to open MscL has been quantitatively determined, and electrophysiology has predicted that there are several discreet steps on the opening pathway (Sukharev et al., 1999b).

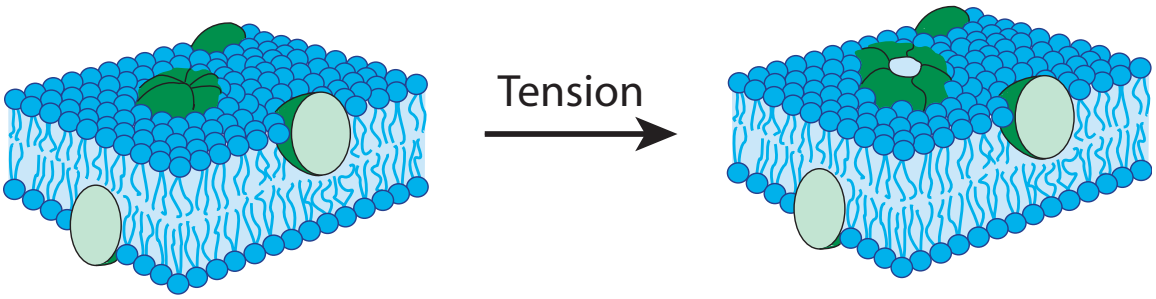

Figure 1.1: The mechanosensitive channel of lager conductance gates in response to bilayer tension.

The single channel conductance of MscL predicted the open pore of the channel to be around 40Å (Sukharev et al., 1997). This large pore was confirmed by molecular sieving experiments that suggested that molecules on the order of 30Å in diameter could pass through the pore of MscL, while molecules of on the order of 37Å in diameter were excluded (Cruickshank et al., 1997). Further evidence for this enormous open state comes from experiments in which small proteins, such as GFP and thioredoxin, have been shown to efflux through MscL upon osmotic downshock (Ajouz et al., 1998; Jones et al., 2000).

The ability of MscL alone to rescue bacteria from osmotic downshock was initially confirmed by introduction of *E. coli* MscL into *V. alginolyticus*, an osmotically sensitive bacterial strain (Nakamaru et al., 1999). This was later confirmed in *E. coli*, after the cloning of MscS and the production of MscS knockout *E. coli* strains (Levina et al., 1999). These experiments provided further evidence that the physiological role of MscL is to prevent bacteria from bursting upon osmotic downshock. This is a desirable attribute for bacteria, since it is likely that they will experience a variety of different osmotic conditions over their life cycle.

Mutagenesis of MscL produced channels with altered gating tensions (Blount et al., 1997; Blount et al., 1996b; Ou et al., 1998; Yoshimura et al., 2001; Yoshimura et al., 1999). Mutations that made MscL easier to gate than wild type MscL were termed gain of function mutations (GOF), while mutations that made MscL harder to gate than wild type MscL were termed loss of function mutations (LOF). Random mutagenesis of *E. coli* MscL revealed a series of gain of function mutations along one face of the helix making up the first transmembrane domain and identified the plug of the closed channel (Ou et al., 1998).

Initial biochemical analysis and two-dimensional crystallographical analysis suggested that MscL was a homohexamer (Blount et al., 1996a; Hase et al., 1997; Saint et al., 1998). The high-resolution crystal structure of MscL revealed the actual multimerization of the channel to pentameric (Chang et al., 1998). The multimerization state of MscL observed in the crystal structure was confirmed by subsequent biochemical analysis

(Maurer et al., 2000; Sukharev et al., 1999a). The multimerization state of the channel is the only biochemical or biophysical analysis of MscL that was proven to be inaccurate by the high-resolution structure.

1.2.3 The Crystal Structure of MscL

In late 1998, the Rees lab obtained a high-resolution crystal structure of the M. tuberculosis homologue of MscL (Tb-MscL) (Chang et al., 1998). Crystalization of Tb-MscL was obtained under acidic conditions (pH 3.0) and in dodecylmaltoside (DDM). The structure was refined to 3.5 Å by soaking the crystals in $Na_2Au(S_2O_3)_2$. Figure 1.2 shows side, top, and bottom views of the Tb-MscL crystal structure.

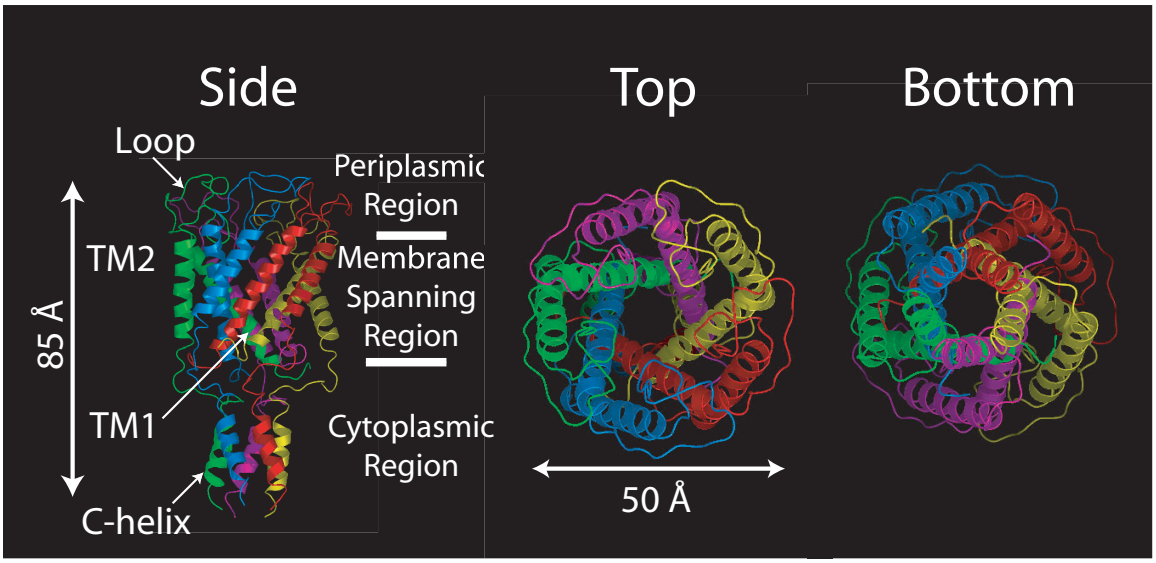

Figure 1.2: The Tb-MscL crystal structure viewed from side, top, and bottom.

As predicted, MscL consists of two transmembrane domains and a long carboxyl terminus. The proteib is 85 Å in length with hydrophobic membrane spanning region of

approximately 35 Å. The two transmembrane helices are tilted approximately 28˚ with respect to the membrane, and the cytoplasmic helix is tilted approximately 15˚ with respect to the membrane. The pore of the channel ranges in diameter from approximately 2 Å to 18 Å with a plug formed by V21.

Despite providing an impressive view of the MscL structure, significant portions of the structure could not be resolved. As a result the crystal structure is missing the first nine residues and the last thirty-three residues of Tb-MscL. Additionally there was insufficient electron density to build in the side chains for residues I56, L57, R58, I59, L97, K100, Q105, and R118.

1.2.4 Post-Structure Analysis of MscL

The high-resolution structure of Tb-MscL has opened up new and exciting opportunities to examine structure-function relationships using the crystal structure as a starting point. With the crystal structure in hand, a variety of techniques, which previously would have provided only minimal information or would not have been possible, are now applicable. These techniques are starting to explain the molecular function of MscL.

Computer modeling has been employed to gain insight into the molecular motions associated with channel function. Molecular dynamics has been applied to the Tb-MscL crystal structure (Bilston and Mylvaganam, 2002; Elmore and Dougherty, 2001; Gullingsrud et al., 2001; Kong et al., 2002). These simulations have provide some

interesting results; however, at present it is not possible to run molecular dynamics simulations long enough to see the transition from the closed to the open state.

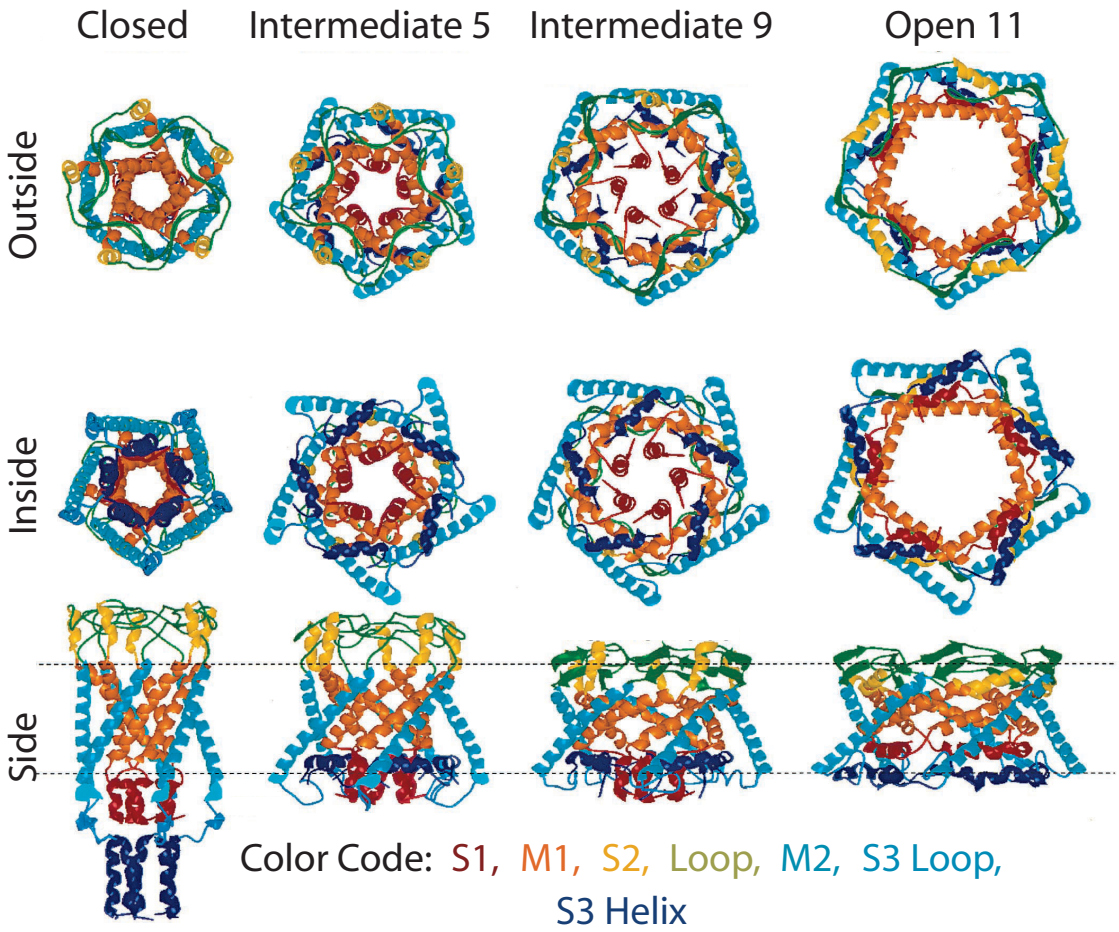

Figure 1.3: The de novo gating model for *E. coli* MscL developed by Sukharev, Guy, and co-workers.

Since the open state structure of MscL is unknown, de novo construction of molecular models for the open state and various intermediates on the opening pathway has been attempted (Sukharev et al., 2001a; Sukharev et al., 2001b). Figure 1.3 shows the atomic level gating model developed by Sukharev, Guy, and co-workers for the *E. coli*

homologue of MscL. Although the crystal structure is of the *M. tuberculosis* homologue of MscL, Sukharev, Guy, and co-workers chose to model the *E. coli* homologue so that they could make use of the large collection of experimental data that exists for *E. coli* MscL.

Recently, Perozo, Martinac, and co-workers have applied cysteine mutatagenesis and site specific spin labeling coupled with electron paramagnetic resonance spectroscopy to *E. coli* MscL (Perozo et al., 2002a; Perozo et al., 2001; Perozo et al., 2002b). Using these techniques, Perozo and co-workers have confirmed that the *E. coli* MscL homologue is structurally similar to the *M. tuberculosis* homologue. Additionally, they have developed a technique to image the open state and an intermediate state of *E. coli* MscL on the EPR time scale. Using this technique, they have been able to obtain a limited number of constraints for the open state of *E. coli* MscL. From these constraints they have developed a computational model for the transmembrane domains of E. coli MscL in the closed, intermediate, open state. Their model is shown if Figure 1.4.

Chapter 2 provides verification of the Tb-MscL crystal structure and a comparison of the *E. coli* and *M. tuberculosis* homologues of MscL. Here we show that the Tb-MscL crystal structure can be used as a starting point for structural design and that Tb-MscL is pentameric under physiological conditions. Additionally, we show that there are significant differences between the *E. coli* and *M. tuberculosis* homologues of MscL. These differences are shown by sequence analysis, circular dichroism studies, and mutational profiling.

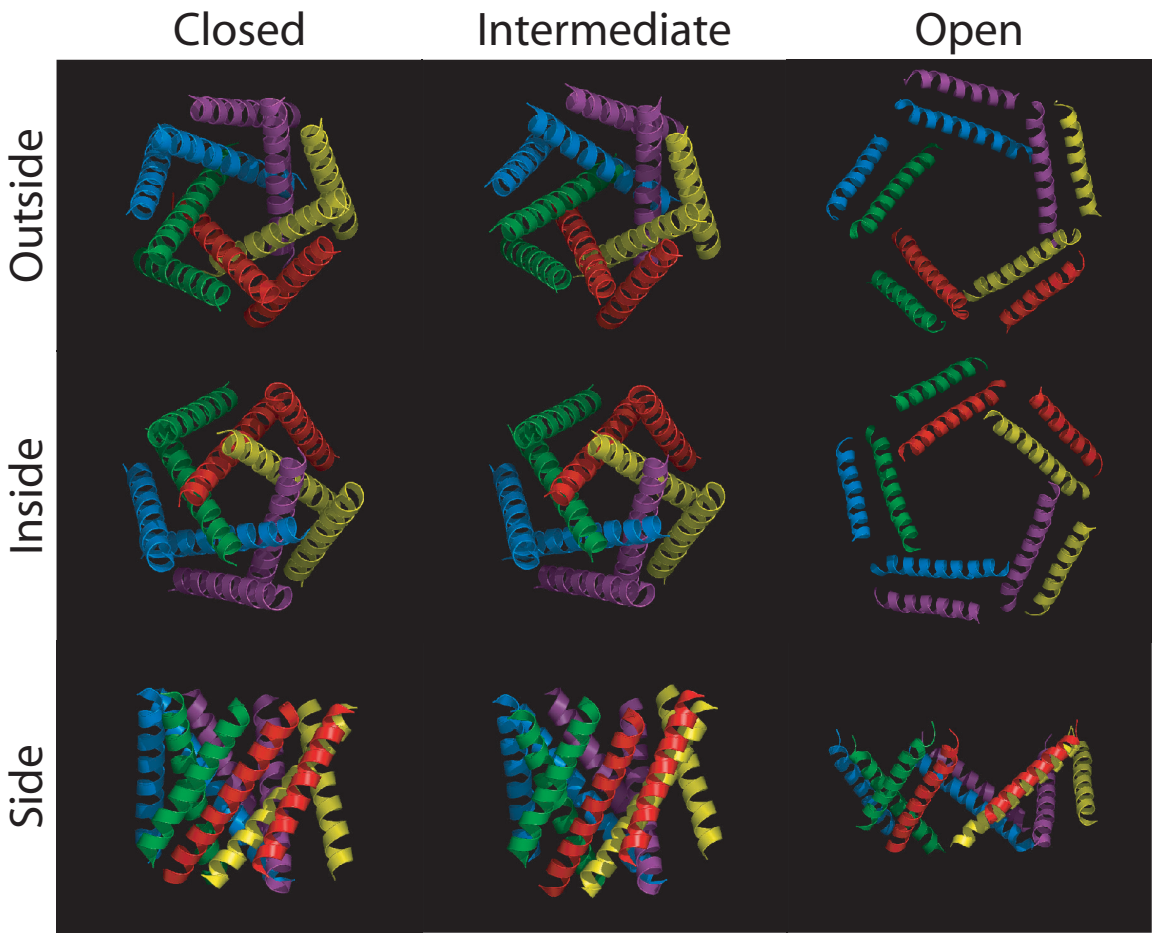

Figure 1.4: Computational model for the transmembrane domains of *E. coli* MscL developed by Perozo, Martinac, and co-workers using EPR constraints.

In Chapter 3, a high throughput fluorescent screen for mutagenic analysis of *E. coli* MscL is developed. This screen allows for rapid mutational phenotyping of mutant MscL channels. Application of this screen, in Chapter 4, to a large library of random MscL mutations provides data to evaluate the de novo *E. coli* MscL gating model. Although it is difficult to use point mutations to comment on the general mechanism of gating proposed by the model, these mutations highlight some regions of the model that need modification. Additionally, the clustering of loss of function mutations observed in the

library suggests that the tension sensor for MscL may be located in the transmembrane domains near the lipid headgroups.

Chapter 5 analyses the carboxyl terminal region of MscL. Once again significant differences are observed between *M. tuberculosis* and *E. coli* homologues of MscL. The carboxyl terminus of Tb-MscL has a significant function role, while the carboxyl terminus of *E. coli* MscL has no functional role. Strikingly, the thirty-three amino acid residues that could not be resolved in the Tb-MscL crystal structure dramatically affect channel function. Even a charge neutralization two residues from the end of the Tb-MscL protein is observed to have afunctional effect on the channel.

1.3 Literature Cited

Ajouz, B., Berrier, C., Garrigues, A., Besnard, M., and Ghazi, E. (1998). Release of thioredoxin via the mechanosensitive channel MscL during osmotic downshock of *Escherichia coli* cells. Journal of Biological Chemistry *273*, 26670-26674.

Armstrong, N., and Gouaux, E. (2000). Mechanisms for activation and antagonism of an AMPA-sensitive glutamate receptor: crystal structures of the GluR2 ligand binding core. Neuron *28*, 165-181.

Armstrong, N., Sun, Y., Chen, G. Q., and Gouaux, E. (1998). Structure of a glutamate-receptor ligand-binding core in complex with kainate. Nature *395*, 913-917.

Barchi, R. L. (1998). Ion channel mutations affecting muscle and brain. Current Opinion in Neurology *11*, 461-468.

Bilston, L. E., and Mylvaganam, K. (2002). Molecular simulations of the large conductance mechanosensitive (MscL) channel under mechanical loading. Febs Letters *512*, 185-190.

Blount, P., Schroeder, M. J., and Kung, C. (1997). Mutations in a bacterial mechanosensitive channel change the cellular response to osmotic stress. Journal of Biological Chemistry *272*, 32150-32157.

Blount, P., Sukharev, S. I., Moe, P. C., Schroeder, M. J., Guy, H. R., and Kung, C. (1996a). Membrane topology and multimeric structure of a mechanosensitive channel protein of *Escherichia coli*. Embo Journal *15*, 4798-4805.

Blount, P., Sukharev, S. I., Schroeder, M. J., Nagle, S. K., and Kung, C. (1996b). Single residue substitutions that change the gating properties of a mechanosensitive channel in *Escherichia coli*. Proceedings of the National Academy of Sciences of the United States of America *93*, 11652-11657.

Brejc, K., van Dijk, W. J., Klaassen, R. V., Schuurmans, M., van Der Oost, J., Smit, A. B., and Sixma, T. K. (2001). Crystal structure of an ACh-binding protein reveals the ligand-binding domain of nicotinic receptors. Nature *411*, 269-276.

Chang, G., Spencer, R. H., Lee, A. T., Barclay, M. T., and Rees, D. C. (1998). Structure of the MscL homolog from *Mycobacterium tuberculosis*: A gated mechanosensitive ion channel. Science *282*, 2220-2226.

Cruickshank, C. C., Minchin, R. F., LeDain, A. C., and Martinac, B. (1997). Estimation of the pore size of the large-conductance mechanosensitive ion channel of *Escherichia coli*. Biophysical Journal *73*, 1925-1931.

Dougherty, D. A. (2000). Unnatural amino acids as probes of protein structure and function. Current Opinion in Chemical Biology *4*, 645-652.

Doyle, D. A., Morais Cabral, J., Pfuetzner, R. A., Kuo, A., Gulbis, J. M., Cohen, S. L., Chait, B. T., and MacKinnon, R. (1998). The structure of the potassium channel: molecular basis of K+ conduction and selectivity. Science *280*, 69-77.

Dutzler, R., Campbell, E. B., Cadene, M., Chait, B. T., and MacKinnon, R. (2002). X-ray structure of a ClC chloride channel at 3.0 A reveals the molecular basis of anion selectivity. Nature *415*, 287-294.

Elmore, D. E., and Dougherty, D. A. (2001). Molecular dynamics simulations of wild-type and mutant forms of the *Mycobacterium tuberculosis* MscL channel. Biophysical Journal *81*, 1345-1359.

Fink, M., Duprat, F., Lesage, F., Reyes, R., Romey, G., Heurteaux, C., and Lazdunski, M. (1996). Cloning, functional expression and brain localization of a novel unconventional outward rectifier K+ channel. Embo J *15*, 6854-6862.

Green, T., Heinemann, S. F., and Gusella, J. F. (1998). Molecular neurobiology and genetics: investigation of neural function and dysfunction. Neuron *20*, 427-444.

Gullingsrud, J., Kosztin, D., and Schulten, K. (2001). Structural determinants of MscL gating studied by molecular dynamics simulations. Biophysical Journal *80*, 2074-2081.

Hamill, O., and McBride, D. (1993). Molecular clues to mechanosensitivity. Biophys J *65*, 17-18.

Hamill, O. P., and Martinac, B. (2001). Molecular basis of mechanotransduction in living cells. Physiological Reviews *81*, 685-740.

Hamill, O. P., and McBride, D. W., Jr. (1994). The cloning of a mechano-gated membrane ion channel. Trends Neurosci *17*, 439-443.

Hamill, O. P., and McBride, D. W., Jr. (1996). The pharmacology of mechanogated membrane ion channels. Pharmacol Rev *48*, 231-252.

Hase, C. C., Minchin, R. F., Kloda, A., and Martinac, B. (1997). Cross-linking studies and membrane localization and assembly of radiolabelled large mechanosensitive ion channel (MscL) of *Escherichia coli*. Biochemical and Biophysical Research Communications *232*, 777-782.

Jiang, Y., Lee, A., Chen, J., Cadene, M., Chait, B. T., and MacKinnon, R. (2002a). Crystal structure and mechanism of a calcium-gated potassium channel. Nature *417*, 515-522.

Jiang, Y., Lee, A., Chen, J., Cadene, M., Chait, B. T., and MacKinnon, R. (2002b). The open pore conformation of potassium channels. Nature *417*, 523-526.

Jones, S. E., Naik, R. R., and Stone, M. O. (2000). Use of small fluorescent molecules to monitor channel activity. Biochemical and Biophysical Research Communications *279*, 208-212.

Kong, Y. F., Shen, Y. F., Warth, T. E., and Ma, J. P. (2002). Conformational pathways in the gating of Escherichia coli mechanosensitive channel. Proceedings of the National Academy of Sciences of the United States of America *99*, 5999-6004.

Levina, N., Totemeyer, S., Stokes, N. R., Louis, P., Jones, M. A., and Booth, I. R. (1999). Protection of *Escherichia coli* cells against extreme turgor by activation of MscS and MscL mechanosensitive channels: identification of genes required for MscS activity. Embo Journal *18*, 1730-1737.

Martinac, B., Buechner, M., Delcour, A. H., Adler, J., and Kung, C. (1987). Pressure-sensitive ion channel in *Escherichia coli*. Proceedings of the National Academy of Science of the United States of America *84*, 2297-2301.

Maurer, J. A., Elmore, D. E., Lester, H. A., and Dougherty, D. A. (2000). Comparing and contrasting *Escherichia coli* and *Mycobacterium tuberculosis* mechanosensitive channels (MscL) - New gain of function mutations in the loop region. Journal of Biological Chemistry *275*, 22238-22244.

Moe, P. C., Blount, P., and Kung, C. (1998). Functional and structural conservation in the mechanosensitive channel MscL implicates elements crucial for mechanosensation. Molecular Microbiology *28*, 583-592.

Moe, P. C., Levin, G., and Blount, P. (2000). Correlating a protein structure with function of a bacterial mechanosensitive channel. J Biol Chem *275*, 31121-31127.

Nakamaru, Y., Takahashi, Y., Unemoto, T., and Nakamura, T. (1999). Mechanosensitive channel functions to alleviate the cell lysis of marine bacterium, *Vibrio alginolyticus*, by osmotic downshock. Febs Letters *444*, 170-172.

Ou, X. R., Blount, P., Hoffman, R. J., and Kung, C. (1998). One face of a transmembrane helix is crucial in mechanosensitive channel gating. Proceedings of the National Academy of Sciences of the United States of America *95*, 11471-11475.

Paterson, D., and Nordberg, A. (2000). Neuronal nicotinic receptors in the human brain. Progress in Neurobiology *61*, 75-111.

Perozo, E., Cortes, D. M., Sompornpisut, P., Kloda, A., and Martinac, B. (2002a). Open channel structure of MscL and the gating mechanism of mechanosensitive channels. Nature *418*, 942-948.

Perozo, E., Kloda, A., Cortes, D. M., and Martinac, B. (2001). Site-directed spin-labeling analysis of reconstituted Mscl in the closed state. J Gen Physiol *118*, 193-206.

Perozo, E., Kloda, A., Cortes, D. M., and Martinac, B. (2002b). Physical principles underlying the transduction of bilayer deformation forces during mechanosensitive channel gating. Nat Struct Biol *9*, 696-703.

Saint, N., Lacapere, J. J., Gu, L. Q., Ghazi, A., Martinac, B., and Rigaud, J. L. (1998). A hexameric transmembrane pore revealed by two-dimensional crystallization of the large mechanosensitive ion channel (MscL) of *Escherichia coli*. Journal of Biological Chemistry *273*, 14667-14670.

Sukharev, S., Betanzos, M., Chiang, C. S., and Guy, H. R. (2001a). The gating mechanism of the large mechanosensitive channel MscL. Nature *409*, 720-724.

Sukharev, S., Durell, S. R., and Guy, H. R. (2001b). Structural models of the MscL gating mechanism. Biophysical Journal *81*, 917-936.

Sukharev, S. I., Blount, P., Martinac, B., Blattner, F. R., and Kung, C. (1994). A Large-Conductance Mechanosensitive Channel in *E. Coli* Encoded by Mscl Alone. Nature *368*, 265-268.

Sukharev, S. I., Blount, P., Martinac, B., and Kung, C. (1997). Mechanosensitive channels of *Escherichia coli*: The MscL gene, protein, and activities. Annual Review of Physiology *59*, 633-657.

Sukharev, S. I., Schroeder, M. J., and McCaslin, D. R. (1999a). Stoichiometry of the large conductance bacterial mechanosensitive channel of *E. coli*. - A biochemical study. Journal of Membrane Biology *171*, 183-193.

Sukharev, S. I., Sigurdson, W. J., Kung, C., and Sachs, F. (1999b). Energetic and spatial parameters for gating of the bacterial large conductance mechanosensitive channel, MscL. Journal of General Physiology *113*, 525-539.

Wood, J. M. (1999). Osmosensing by bacteria: Signals and membrane-based sensors. Microbiology and Molecular Biology Reviews *63*, 230.

Yoshimura, K., Batiza, A., and Kung, C. (2001). Chemically charging the pore constriction opens the mechanosensitive channel MscL. Biophysical Journal *80*, 2198-2206.

Yoshimura, K., Batiza, A., Schroeder, M., Blount, P., and Kung, C. (1999). Hydrophilicity of a single residue within MscL correlates with increased channel mechanosensitivity. Biophysical Journal *77*, 1960-1972.

Chapter 2: Comparing and Contrasting the Mechanosenstive Channels of Large Conductance (MscL) from *E. coli* and *M. tuberculosis* and Verification of the *M. tuberculosis* Crystal Structure.

2.1 Introduction

Recent work has attempted to rationalize the extensive functional studies on *E. coli* MscL (Ec-MscL) in light of the crystal structure, which was obtained for the *M. tuberculosis* homologue (Tb-MscL) (Batiza et al., 1999; Blount and Moe, 1999; Chang et al., 1998; Oakley et al., 1999; Rees et al., 2000; Spencer et al., 1999). Additionally, several different models for channel opening have been proposed by considering *E. coli* gain of function (GOF) mutations in terms of the *M. tuberculosis* crystal structure (Batiza et al., 1999; Chang et al., 1998; Sukharev et al., 2001b). To critically evaluate these efforts, it is essential to assess the underlying assumption of the portability of Ec-MscL functional data to the Tb-MscL structure. While the function of the *E. coli* channel has been extensively probed by site-directed and random mutagenesis, analogous studies of the *M. tuberculosis* channel have not been reported (Batiza and Kung, 2000; Blount et al., 1998; Blount et al., 1997; Blount et al., 1996b; Liu et al., 1999; Ou et al., 1998; Yoshimura et al., 1999). Preliminary data have shown that wild-type *E. coli* and *M. tuberculosis* MscL are similar electrophysiologically. Both channels exhibit a large single channel conductance, approximately 3.5 nS, and gate with similar tensions in reconstituted liposomes (Moe et al., 2000; Shapovalov and Lester, 2000). However, the Tb-MscL channel exhibits twice the gating tension of Ec-MscL in *E. coli* spheroplasts (Moe et al., 2000). This difference may result from protein structural differences, a difference in interactions with lipids, or both.

Sequence alignment is essential to map previously studied *E. coli* GOF mutations onto the *M. tuberculosis* MscL sequence. In this work we report an optimal sequence

alignment of 35 MscL homologues and an information on regions of conservation and variability. Consistent with previous studies, we find greater conservation in the transmembrane regions than in the loop or intracellular regions. Interestingly, the various channels clearly fall into subfamilies based on sequence similarity, with Ec-MscL and Tb-MscL in different subfamilies.

Circular dichroism is a method of obtaining crude structural analysis of proteins and provides another estimate of overall similarity between homologous proteins. Here we present circular dichroism spectra of nine MscL homologues. As with the sequence analysis, MscL homologues fall into subfamilies based on their observed helicity. Surprisingly, the subfamilies obtained from circular dichroism analysis are different than those obtained from sequence analysis.

Using the optimal alignment, we have prepared Tb-MscL analogues of several critical Ec-MscL GOF mutations (Figure 2.1-A). Perhaps surprisingly, we find that several well-established Ec-MscL GOF mutants do not translate to the Tb-MscL system. We also directly evaluate a predicted intersubunit hydrogen bond in the Tb-MscL crystal structure (Figure 2.1-B). Cross-linking studies establish that these residues are indeed close in the reconstituted channel, and firmly establish the pentameric nature of the channel. Mutations of this pair generally lead to GOF mutants, suggesting an important functional role for this specific region of the channel. Interestingly, no analogous interaction is apparent in the Ec-MscL alignment. Our results indicate that the functional

studies performed on the Ec-MscL channel may not map directly onto the Tb-MscL crystal structure.

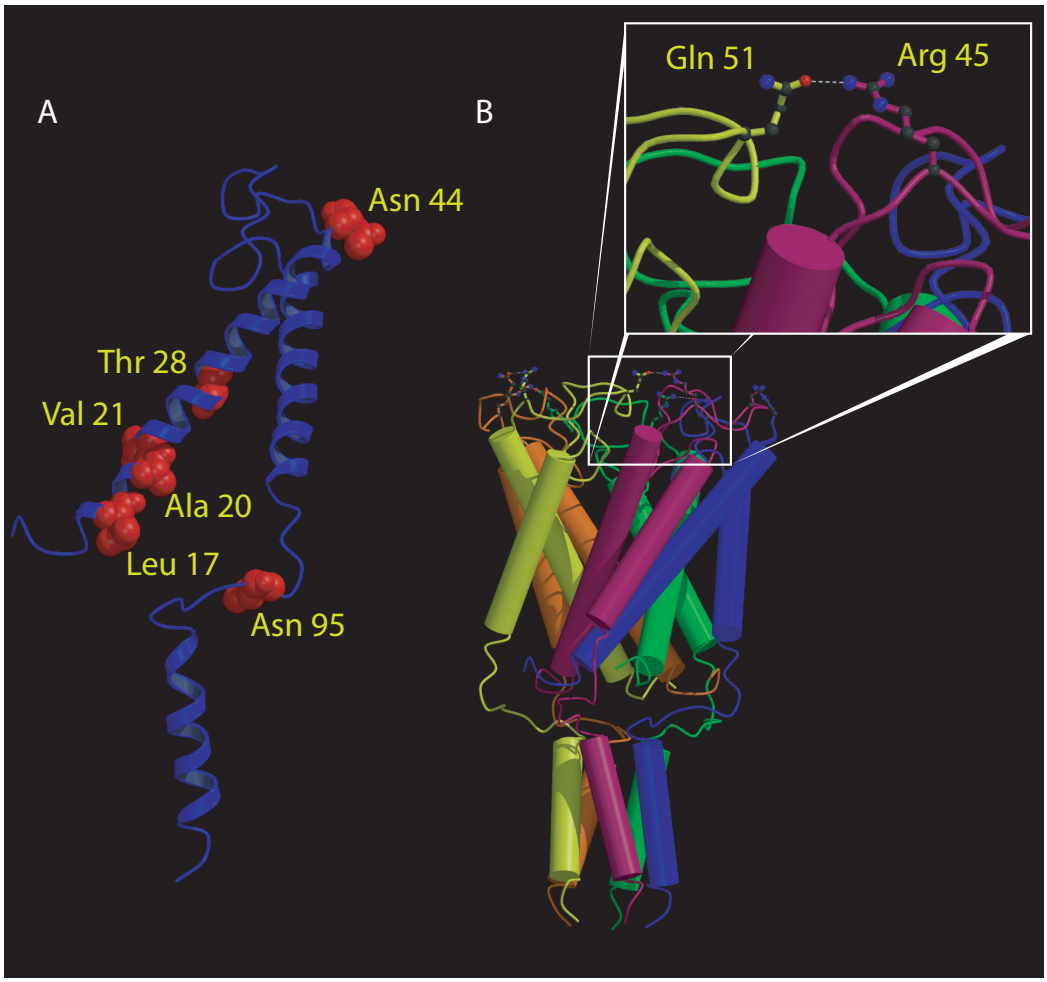

Figure 2.1: *M. tuberculosis* MscL crystal structure. **(A)** Severe and very severe GOF mutations from Ec-MscL are mapped onto one subunit of the Tb-MscL crystal structure. **(B)** The R45•••Q51 hydrogen bond. The box shows a closeup of the hydrogen bond between the yellow and purple subunits. Figures were generated with MOLSCRIPT and Raster3D.

2.2 Results

2.2.1 Sequence Analysis

Although clearly related, the mechanosensitive channels from various organisms show moderate to low sequence identities. For example, the sequence identity of Tb-MscL compared to Ec-MscL is 37%, while the sequence identity of *B. bronchiseptica* MscL compared to *M. leprae* MscL is 15%. Therefore, development of an optimal alignment is not straightforward. For this reason, we have augmented sequence alignment approaches with MEME analysis (Bailey and Elkan, 1994; Bailey and Gribskov, 1998), which identifies conserved regions within a group of sequences. Figure 2.2 shows an AMPS multiple sequence alignment and MEME group analysis of 35 putative MscL sequences. The MEME group analysis was used to make slight adjustments to the AMPS multiple sequence alignment using the indicated areas of conservation within the sequences. This alignment was further analyzed to determine which regions of MscL were most divergent using AMPS pairwise alignment of the full sequences and of selected regions, such as the first and second transmembrane domains, the extracellular loop, and the carboxy terminus. Regional divisions were made by applying the previous definitions from the Tb-MscL crystal structure to the multiple sequence alignment (Chang et al., 1998). These alignments indicate general overall similarity for all regions of the protein; however, the loop region clearly shows the most variability. Contour plots showing scores for the AMPS pairwise alignments of the first transmembrane domain, the extracellular loop, and the carboxy terminus are shown in Figure 2.3.

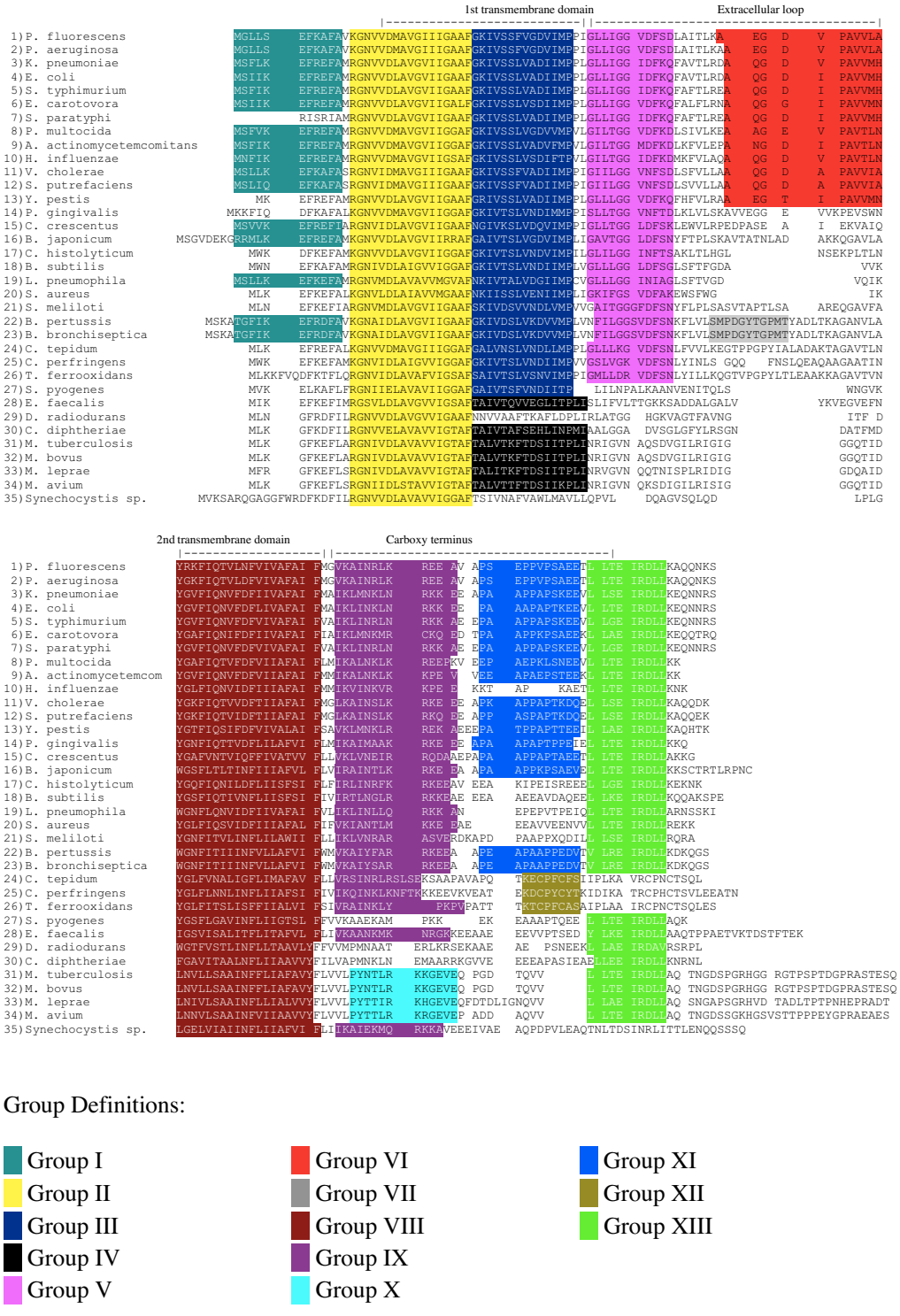

Figure 2.2: MEME consensus group analysis shown on the AMPS multiple sequence alignment. The AMPS multiple sequence alignment of 35 putative MscL sequences is shown. The colored regions on the sequence alignment indicate MEME consensus groups.

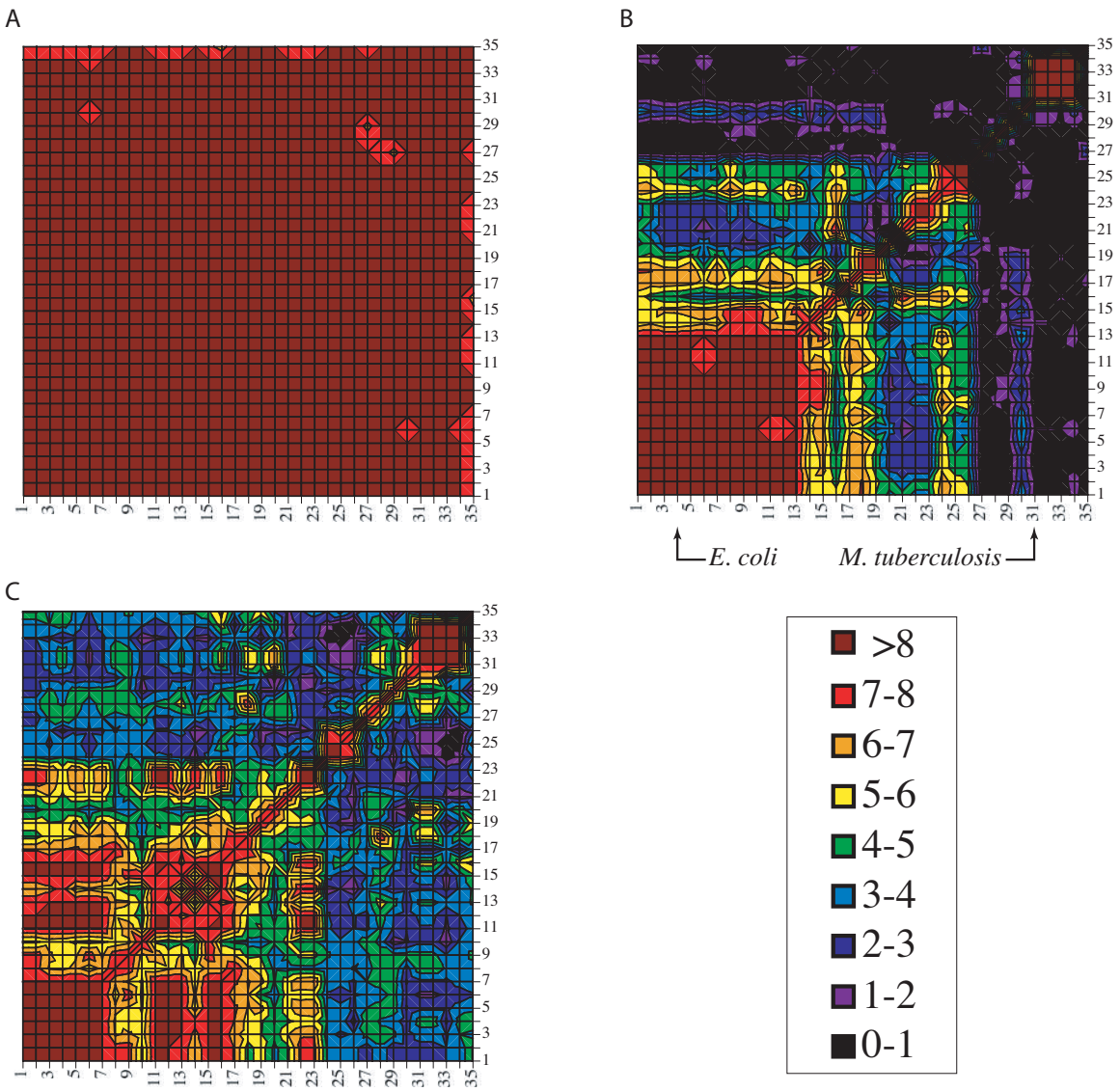

Figure 2.3: Regional AMPS pairwise alignments for the first transmembrane domain, the loop region, and the carboxyl terminus. Numbers on axes correspond to the sequence numbers in Figure 2. (A) The contour plot for the first transmembrane domain shows that this region of the MscL protein is almost completely conserved. (B) The loop region shows much more diversity than seen in the first transmembrane domain. Very low scores are observed for some pairs of proteins in this region. The contour plot shows groupings of sequences, with a large subfamily containing *E. coli* and a smaller subfamily containing *M. tuberculosis*. (C) The contour plot of the carboxyl terminal region shows more diversity than observed for the first transmembrane domain, however less diversity than observed for the loop region.

2.2.2 Comparative Circular Dichroism Studies

Circular dichroism was used to compare the subset of MscL homologues that have been functionally characterized (Moe et al., 1998). The spectra obtained for these homologues are shown in Figure 2.4, and selected features are listed in Table 2.1. As observed with the sequence alignment of MscL homologues, the homologues fall into two distinct families. The families resulting from the circular dichroism studies are different than those observed from the sequence alignment data. Based on the observed circular dichroism spectra, the first family is composed of *E. coli*, *H. influenza*, and *P. fluorescens* and the second family is composed of *M. tuberculosis*, *E. carotovora*, *C. perfringens*. *S. aureus*, *B. subtilis*, and *Synechocytis sp*.

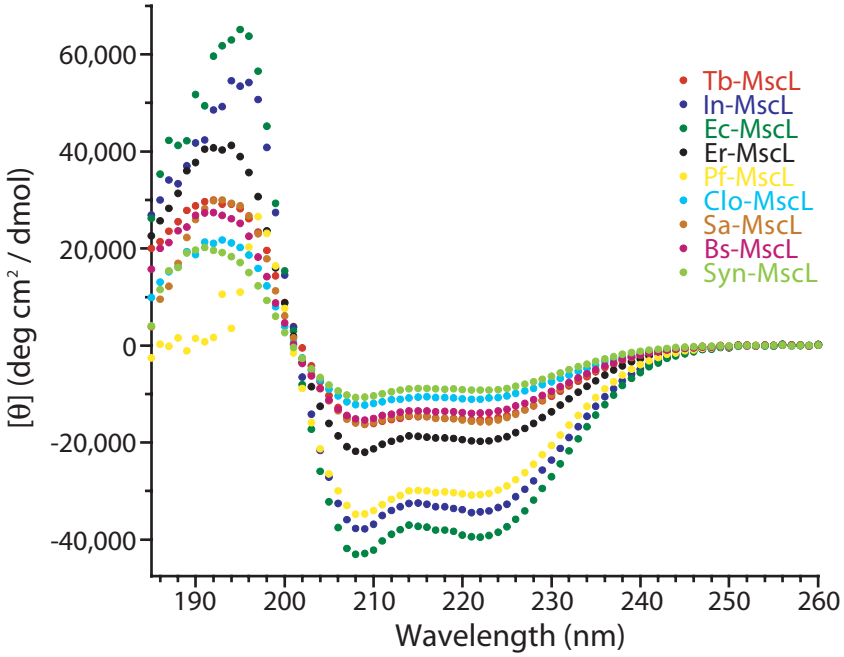

Figure 2.4: Circular dichrosims spectra for nine different homologues of the mechanosenitive channel of large conductance. Two groupings of channels are observed from the CD data with Ec-MscL and Tb-MscL lying in different groups.

Using the elipticity at 222 nm observed in the circular dichrosim spectra, the percent helicity of each MscL homologue was estimated as previously described for Ec-MscL (Brunger Method) (Arkin et al., 1998). Additionally, the percent helical content for each sequence was predicted using Jpred (Cuff and Barton, 1999). These data are shown in Table 2.1.

Species	Abbreviation	Sequence number	Helical Content from CD	Helical Content from Jpred
P. fluorescens	Pf	1	85-51%	48%
H. influenza	In	10	95-57%	56%
E. coli	Ec	4	110-66%	53%
E. carotovora	Er	6	55-33%	49%
M. tuberculosis	Tb	31	42-25%	45%
C. perfringens	Clo	25	31-18%	35%
S. aureus	Sa	20	44-26%	50%
B. subtilis	Bs	18	39-23%	52%
Synechocystis sp.	Syn	35	25-15%	50%

Table 2.1: A summary of the circular dichroism specra for various homologues of MscL. Jpred predictions of helical content are based on sequence analaysis. Helical content fro the various MscL homologues was determined from the abosorbance in the CD spectrum at 222 nm using the method previously described for Ec-MscL

Since MscL homologues vary considerably in length from 143 amino acids to 175 amino acids, the observed helicity as a function of protein length was examined. Figure 2.5 shows a plot of the maximal helicity predicted for each homologue as a function of homologue length. No correlation is observed between these quantities.

2.2.3 Mutational Mapping

With an optimal alignment in hand (Figure 2.2), we were able to map some of the very severe and severe mutations from Ec-MscL onto Tb-MscL (Oakley et al., 1999). The

most extensively probed type of mutation has been the so-called gain of function (GOF) mutation. This is observed in growth studies of *E. coli* expressing the mutant channel. It is assumed that a mutation that increases channel opening probability will, in effect, put a hole in the cell membrane, which is deleterious to growth. The screen thus identifies channels that have a higher open probability at ambient pressure, which is considered a gain of function. (Blount et al., 1997; Ou et al., 1998; Yoshimura et al., 1999)

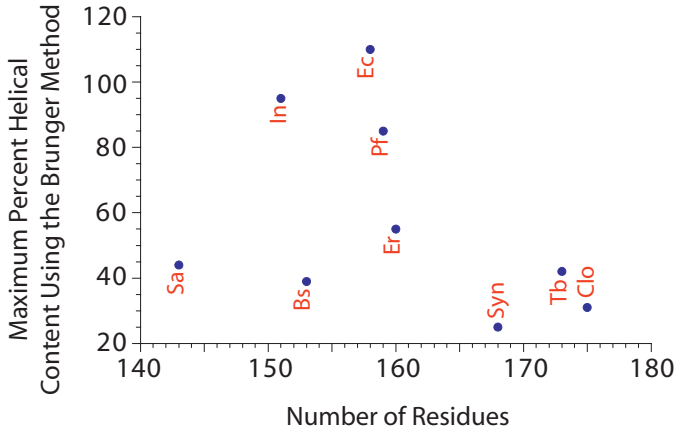

Figure 2.5: Comparison of protein length to the maximal predicted helical content for the various homologues of MscL . No clear trends between protein length and helical content are observerd.

Figure 2.1-A shows the positions of these mutationally sensitive sites mapped onto the Tb-MscL structure. In all cases the alignment we obtain for these residues is the same as others have reported previously. Site directed mutagenesis of Tb-MscL at these positions was performed, converting the wild-type amino acid to a residue shown in *E. coli* to give a GOF phenotype. The resulting mutations were analyzed using plate growth studies and scored using the system described in the Methods section.

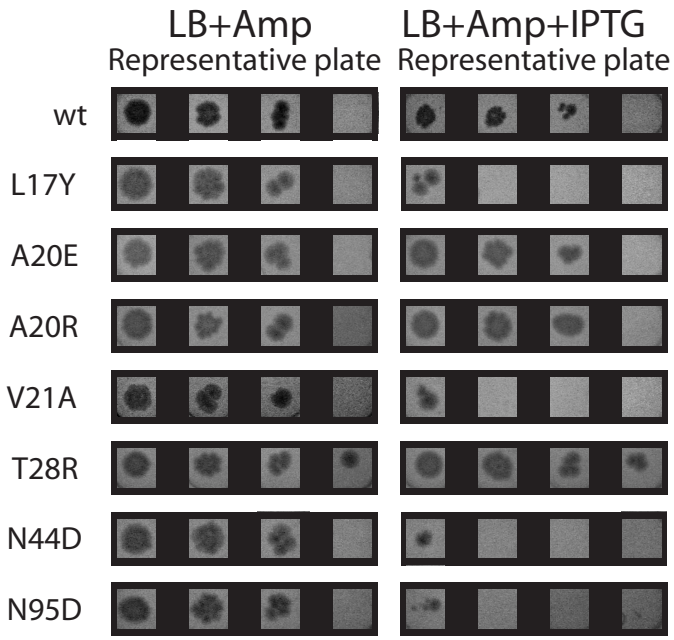

Figure 2.6: Representative plate growth for mutations mapped from *E. coli* MscL to *M. tuberculosis* MscL. The left panel shows the uninduced control and the right panel shows growth in the presence of IPTG. In both panels samples were plated (left to right) from high concentration to low concentration. A GOF phenotype is observed for L17Y, V21A, N44D, and N95D. No difference from wild-type growth is seen for A20E, A20R, and T28R.

Typical plate growth results are shown in Figure 2.6, and all results are gathered in Table 2.2. A GOF phenotype was observed in L17Y, V21A, N44D, and N95D. Unexpectedly, normal growth was observed for A20E, A20R, and T28R, even though the aligned positions, especially A20, were shown to be very sensitive to mutation in Ec-MscL (Batiza and Kung, 2000; Ou et al., 1998; Yoshimura et al., 1999). That mutants displaying normal growth were indeed expressing a MscL channel was verified by SDS-PAGE analysis and Western blotting, which showed levels of protein expression within the variation seen for wild-type Tb-MscL.

Mutant	Number of plates		Average score after 20 h		Average score after 40 h	
	Uninduced	Induced	Uninduced	Induced	Uninduced	Induced
Wild type	51	52	3.38	2.64	3.29	2.75
L17Y	11	11	3.10	0.70	3.19	0.70
A20E	13	13	3.38	3.47	3.38	3.47
A20R	13	13	3.32	3.52	3.32	3.52
V21A	11	11	2.85	1.10	2.85	1.10
T28R	13	13	3.79	3.47	3.79	3.47
N44D	11	11	3.27	0.57	3.27	0.57
N95D	11	11	3.12	0.20	3.20	0.60

Table 2.2: Summarized growth data for GOF mutants mapped from *E. coli* MscL to *M. tuberculosis* MscL.

2.2.4 Verification of the Tb-MscL Structure

Examination of the Tb-MscL structure revealed an intersubunit hydrogen bond, R45•••Q51, located in the loop region of the channel (Figure 2.1-B). Suspecting that such a specific intersubunit contact may be important to function, we mutated this interaction to R45K/Q51E and R45C/Q51C to determine the proximity of these residues under physiological conditions by cross-linking analysis.

The R45K/Q51E mutation was overexpressed and purified from *E. coli*. Cross-linking studies were performed in DDM micelles using EDC or DCC, with or without NHS activators. A typical SDS-PAGE Western blot of cross-linking products is shown in Figure 2.7. Cross-linking is always seen, and in some cases it is quite efficient. After treatment with 10 mM EDC and 10 mM sulfo-NHS, the majority of the observed cross-linked product is tetrameric or pentameric, establishing the high efficiency of this rationally designed cross-linking system.

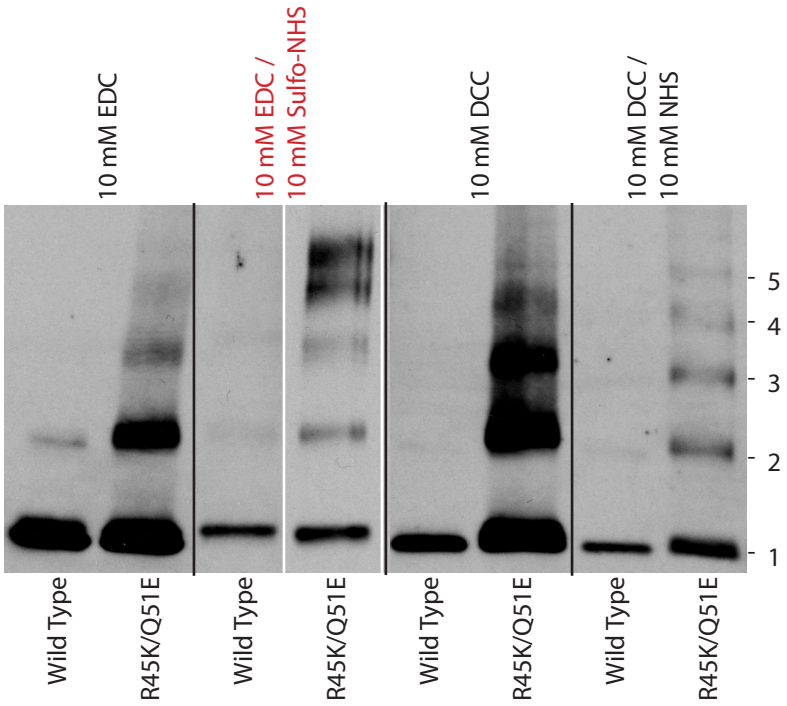

Figure 2.7: Cross-linking of the R45K/Q51E mutant of *M. tuberculosis* MscL. Purified R45K/Q51E *M. tuberculosis* MscL and wild-type protein were cross-linked for 2 hours at 4°C using EDC, DCC, EDC with sulfo-NHS, and DCC with NHS. The reactions were quenched with β-mercaptoethanol, run on a 4-15% SDS-polyacrylamide gel and visualized by Western blotting with 6-His antibody.

Cross-linking of the R45C/Q51C mutant produced similar results to the standard cross-linking of the salt-bridge mutant, but in no instance was highly efficient formation of tetramer and pentamer observed. Disulfide bond formation was induced in the R45C/Q51C mutant by oxidation with copper phenathroline or covalent bond formation was induced using a series of bis-malimide reagents of various tether lengths. The bis-malimide reagents are shown in Figure 2.8, with their associated tether lengths indicated.

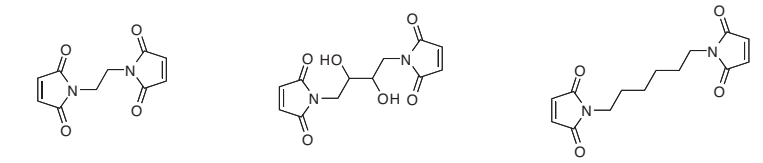

Figure 2.8: Bis-malimide cross-linking reagents with spacer arms of vary lengths.

Typical SDS-PAGE Western blots of the cross-linking reactions are shown in Figure 2.9. Variation in the tether length of the cross-linking reagent from 8.0 Å to 16.1 Å did not affect the cross-linking efficiency of R45C/Q51C Tb-MscL. The variations observed in Figure 2.9 are represntative of variations for a given reaction over several trials.

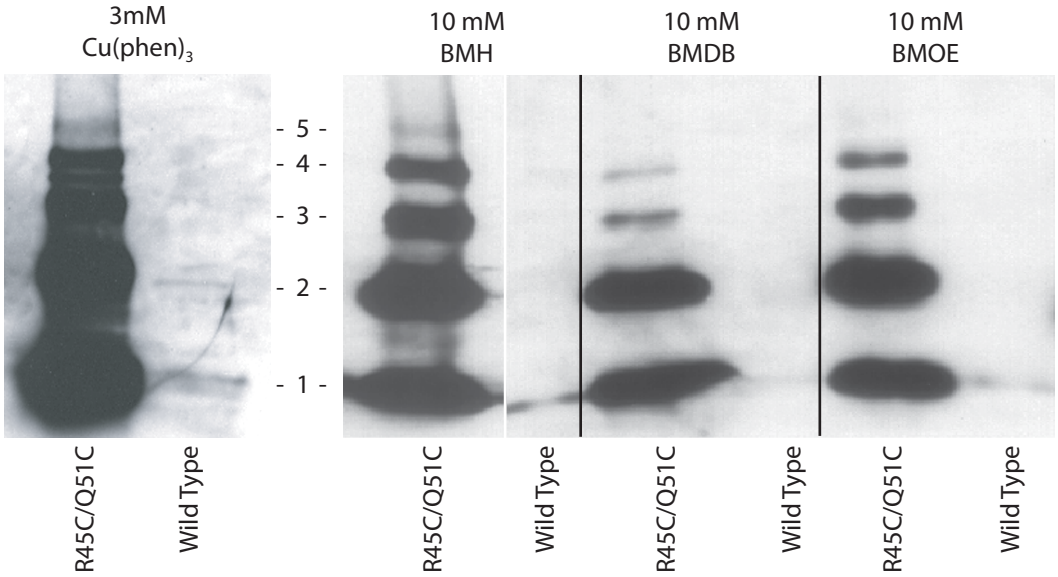

Figure 2.9: Cross-linking of the R45C/Q51C mutant of *M. tuberculosis* MscL. Purified R45C/Q51C *M. tuberculosis* MscL and wild-type protein were cross-linked for 2 hours at 4°C using copper phenanthroline, BMH, BMDB, of BMOE. The reactions were run on a 4-15% SDS-polyacrylamide gel and visualized by Western blotting with 6-His antibody. The copper phenathroline reactions were run in the absence of β-mercaptoethanol.

2.2.5 Functional Characterization of Loop Mutations

Since cross-linking studies confirmed the close proximity of R45 and Q51 under physiological conditions, growth studies were used to assess the effects of mutations at these positions on channel function. The results of growth studies for some single and double mutants at these positions are summarized in Table 2.3, and a representative plate for these mutations is shown in Figure 2.10. All mutations at these positions, with the exception of R45K/Q51K, show a GOF phenotype.

Mutant	Number of plates		Average score after 20 h		Average score after 40 h	
	Uninduced	Induced	Uninduced	Induced	Uninduced	Induced
K45/E51	12	13	3.57	0.00	3.14	0.00
R45K	12	12	3.35	0.00	3.35	0.00
Q51E	12	12	3.07	0.00	3.07	0.00
E45/E51	14	14	3.26	0.64	3.26	0.64
K45/K51	14	14	3.41	3.00	3.62	3.14
C45/C51	12	13	3.65	0.27	3.29	0.43
R45C	12	12	3.59	0.00	3.59	0.00
Q51C	12	12	3.56	0.00	3.56	0.00

Table 2.3: Summarized growth data for mutations of the R45/Q51 hydrogen bond in *M. tuberculosis* MscL.

2.3 Discussion

2.3.1 Sequence Analysis

The MEME sequence analysis has provided insight into the overall similarity of the MscL homologues. Not surprisingly, the homologues are most similar in the transmembrane regions and most divergent in the loop and carboxy terminus regions. The strong similarities in the transmembrane domains are highlighted by the fully conserved groups, II and VIII, and the highly conserved group III. Additionally,

members of the MscL family which lack group III in the first transmembrane region tend to have a similar conserved group IV in this region.

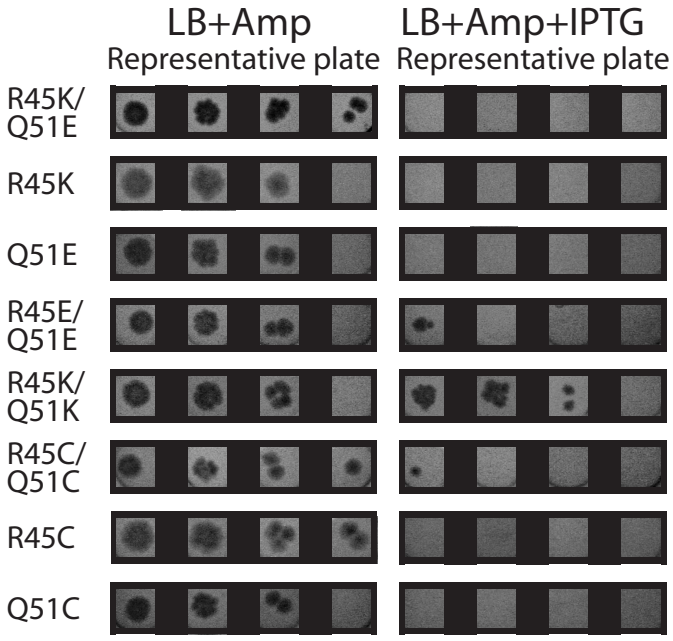

Figure 2.10: Representative plate growth for loop mutations to *M. tuberculosis* MscL. The left panel shows the uninduced control and the right panel shows growth in the presence of IPTG. In both panels samples were plated (left to right) from high concentration to low concentration. A GOF phenotype is observed for R45K/Q51E, R45K, Q51E, R45E/Q51E, R45C/Q51C, R45C, Q51C. No difference from wild-type growth is seen for R45K/Q51K.

The carboxy terminus and loop region are much less conserved. Despite the appearance of three consensus groups in the loop region — V, VI and VII — these groups are clearly not universal. The carboxy terminus is more highly conserved than the loop region, but it is clearly not as well conserved as the transmembrane helices. The carboxy terminus contains two very highly conserved groups — IX and XIII — and the less conserved group XI. Mycobacteria do not contain group IX, but an analogous charged region is evident (group X). Previously it has been shown that a large portion of the carboxy

terminus in Ec-MscL can be deleted without affecting protein function.(Blount et al., 1996b) This is consistent with the lack of sequence conservation in this region.

To further examine the similarities and differences among MscL homologues, a pairwise alignment of the various regions was employed (Figure 2.3). The pairwise alignments showed the same general trends observed with MEME analysis. In general, all regions of the MscL sequence are conserved, however the loop region has pairs of sequences with poor alignment. To some extent the sequence pairs within the loop region can be used to group the homologues into subfamilies. The largest and most obvious subfamily includes *E. coli* MscL and other sequences containing MEME group VI. Another distinctive subfamily includes the Mycobacteria. Thus, by this analysis Ec-MscL and Tb-MscL are in different subfamilies.

2.3.2 Circular Dichroism Studies

As with the sequence analysis, the circular dichroism studies point to two distinct MscL families. However, the families observed by circular dichroism are not the same families that were identified from sequence analysis of putative MscL homologues. In contrast to the results obtained from sequence analysis, Tb-MscL lies in the circular dichroism family with more members and Ec-MscL lies in the circular dichroism family with fewer members.

The helical content of each of the homologues was predicted in an analogous way to that previously used to predict the helical content of Ec-MscL.(Arkin et al., 1998) The two

sequence families show dramatic differences in their predicted helical content, with the first family exhibiting helical contents of 110% to 85% and the second family having a helical content between 55% and 25%.

To determine if the helicity values could be associated with gross differences in secondary structure, the amount of helix in each homologue was predicted using Jpred, a secondary structure prediction program. The predicted helicity values obtained for the MscL homologues using Jpred are quite similar (Table 2.1). It is true that the highest predicted value is for In-MscL, which lies in the Ec-MscL family, and the lowest predicted value is for Clo-MscL, which lies in the Tb-MscL family. However, in general, there is no trend between predicted helical secondary structure and the helical content determined by circular dichroism. In fact, it should be noted that Pf-MscL, which is in the Ec-MscL family, exhibits one of the lowest values for predicted helicity.

The number of amino acids in the homologues examined by circular dichroism varies significantly from 143 to 175 amino acids. However, the predicted helicity from circular dichroism does not correlate with protein length. This is clearly shown in Figure 2.2. The longest and shortest homologues both lie in the Tb-MscL family that displays lower helicity than the Ec-MscL family.

If the Ec-MscL and Tb-MscL families that result from circular dichroism are considered in terms of the sequence analysis, some interesting comparisons result. On the surface, the Tb-MscL family from circular dichroism is composed of seemingly poorly related

sequences. For example, some of the sequences in the Tb-MscL family contain MEME group V and/or MEME group XII, while other members lack these groups. Nonetheless, an interesting similarity between the members of the Tb-MscL family is that all members, other than Er-MscL, lack MEME group VI. In contrast, all of the members of the Ec-MscL family contain MEME group VI, which is located in the loop region. Additionally, Er-MscL has the largest helicity of the Tb-MscL family.

The differences in loop sequence between the two circular dichroism families suggested that it might be possible to identify structural differences from the sequences of this region. To look for structural difference in the loop sequences of the two different families, a FASTA search of the protein structure database (PDB) was performed using the loop regions of the various MscL homologues. This search yielded more helical structures for the Ec-MscL family than for the Tb-MscL family. Sample structures obtained from the search are shown in Figure 2.11. The structural search suggests that members of the Ec-MscL family have dramatically different loop structures than members of the Tb-MscL family. Interestingly these structural differences are reflected in a recent closed state homology model of Ec-MscL (Sukharev et al., 2001a; Sukharev et al., 2001b). Taken together all of the data suggest that the observed differences in the circular dichroism spectra of the MscL homologues may arise from differences in their loop regions.

A

E. coli loop
Initiation factor 4A; 1QVA

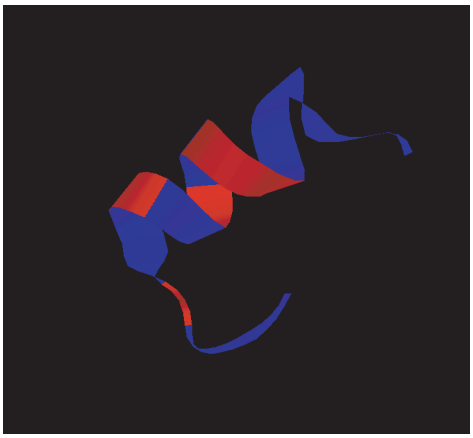

```
GLLIGGIDFKQFAVTLRDAQGDIPAVVMH
   ::: .: . :  :::::
HACIGGTSFVEDAEGLRDAQIVVGTPGRV
```

B

P. fluorescens loop
Flig (Flagellar motor component); 1QC7

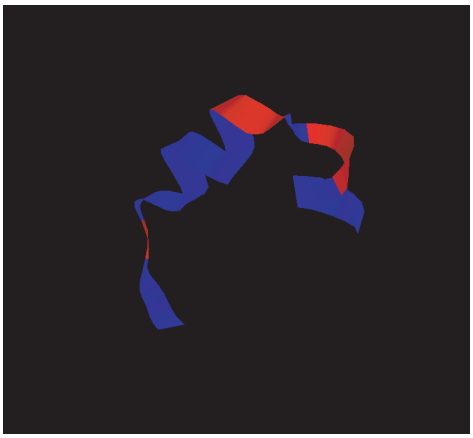

```
GLLIGGVDFSDLAITLKAEGDVPAVVLA
 :..  ::  :::..::. .:
QLVLREVDTRDLALALKGASDELKEKIF
```

C

M. tuberculosis loop
Serratia Metallo Proteinase; 1SMP

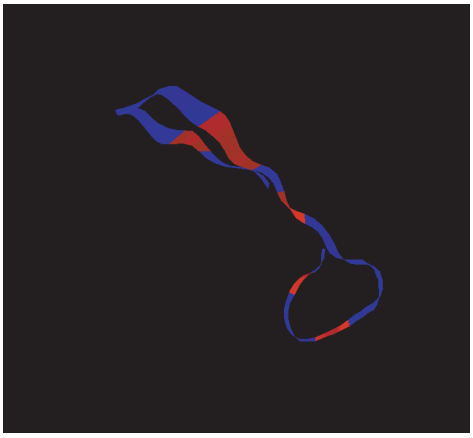

```
NRIGVNAQSDVGILRIGIGGGQTID
  .. ::.:.:  : ..::: :. :
ALLSYNASSNVTDLSVNIGGHQAPD
```

D

C. perfringens loop
C-Src Tyrosine Kinase; 1A1C

```
GSLVGKVDFSNLYINLSGQQFNSLQEAQAAGAATIN
   . :.: ...::. :  ::::::.
HYKIRKLDSGGFYIT-SRTQFNSLQQLVAYYSKHAD
```

Figure 2.11: Sample structures from PDB FASTA searches with MscL loop regions. Only well aligned regions of the loops are shown. Identical and similar residues between the loop and the aligned region of the structure are shown in red.

2.3.3 Mutational Mapping

Previous random mutational analysis of Ec-MscL has focused mainly on the highly conserved transmembrane regions, with only a few mutations in the loop.(Batiza and Kung, 2000; Blount et al., 1997; Blount et al., 1996b; Ou et al., 1998; Yoshimura et al., 1999) For the transmembrane regions, one would expect the sequence homology mapping of the previously obtained GOF *E. coli* mutants onto Tb-MscL to give mutants with a GOF phenotype, due to the high sequence homology in these regions. Note that all alignments, the one reported here and those published previously, agree as to which residues in Tb-MscL correspond to previously studied GOF sites in Ec-MscL.(Batiza et al., 1999; Chang et al., 1998; Oakley et al., 1999; Spencer et al., 1999)

For the majority of mutations studied (L17Y, V21A, N44D, and N95D), the GOF phenotype seen in Ec-MscL is also seen in Tb-MscL (Table 1, Figure 4). Surprisingly, however, mutations at A20 and T28 do not yield a GOF phenotype. The production of Tb-MscL protein for these mutants was confirmed by SDS-PAGE analysis. The lack of GOF phenotype for the A20E and A20R mutants is particularly surprising in light of recent work, which shows that all charged residues at this site give a very severe GOF phenotype in Ec-MscL.(Yoshimura et al., 1999) In fact, only Ala and Gly at these sites produce Ec-MscL with normal function.(Batiza and Kung, 2000)

2.3.4 Tb- MscL Loop Intersubunit Hydrogen Bond

Previous studies of mutations at G46 in Ec-MscL showed the GOF phenotype.(Ou et al., 1998) We have seen similar behavior at the aligned N44 site in Tb-MscL. On examining

the Tb-MscL crystal structure, we observed an intersubunit hydrogen bond involving the adjacent R45 site, with Q51 serving as the partner (Figure 2.1-B). This significant intersubunit interaction suggested an interesting starting point to explore loop function.

Initially, the intersubunit hydrogen bond in the crystal structure was mutated to crosslinkable residues to examine whether these residues are in close proximity under more physiological conditions. The subtle mutation of R45K/Q51E converts the hydrogen bond to a salt bridge. This should still be a favorable intersubunit contact, but the mutant is now susceptible to cross-linking by peptide bond-forming reagents. After overexpression and purification, the protein was exposed to a variety of cross-linking reagents and activators for 2 hours at 4°C. All reagents showed at least a weak pentameric band in the mutant with slight background cross-linking in wild type (Figure 5). The background cross-linking is most likely due to cross-linking in the carboxy terminus of the protein, which contains a number of glutamates, aspartates and lysines.

The most interesting cross-linking results were seen with EDC and Sulfo-NHS. This combination gives mainly pentamer and tetramer for cross-linked products. The strong pentameric band in this designed system provides the best evidence to date that Tb-MscL is pentameric under physiological conditions. Other cross-linking studies typically show progressively weaker band intensities on going from monomer to dimer to trimer, etc., analogous to our results with just EDC and other non-optimal conditions (Figure 2.7) (Blount et al., 1996a; Hase et al., 1997; Sukharev et al., 1999). Such observations always leave open the possibility that a hexamer band is present, but is too weak to be seen as the

intensity progressively falls off with higher oligomerization. Under some conditions, a weak band assigned to hexamer has been seen. However, with the designed double mutant under appropriate conditions (EDC/Sulfo-NHS), very strong tetramer and pentamer bands are seen, but no hexamer band is visible. This provides compelling evidence that no significant fraction of Tb-MscL is present in hexameric (or higher oligomerization) states when reconstituted in DDM micelles.

Cross-linking studies using R45C/Q51C Tb-MscL did not produce the quantitative results observed with R45K/Q51E Tb-MscL. However, high molecular weight bands were observed upon cross-linking, either by oxidation of the free thiols to disulfides or by reaction with bis-malimide reagents (Figure 2.9). Interestingly, when R45C/Q51C Tb-MscL was cross-linked using bis-malimide reagents of varying tether lengths, no distance dependence was observed for cross-linking efficiency. This observation is consistent with the nearly quantitative cross-linking observed for R45K/Q51E Tb-MscL and implies that these side chains are in close proximity.

2.3.5 Functional Studies of the Tb-MscL Loop

After confirming that the residues R45 and Q51 were within interaction distance, we performed growth studies on both single and double mutants to examine channel function. All single mutants (R45K, Q51E, R45C, and Q51C) and all double mutants (R45K/Q51E, R45E/Q51E, and R45C/Q51C) except R45K/Q51K displayed a GOF phenotype (Table 2.3). The lack of a GOF phenotype for the R45K/Q51K mutant is surprising and merits further study. Nevertheless, this region appears to be quite

mutationally sensitive. Note that the R45K mutation is subtle, suggesting that the loop plays a central role in channel gating. Recently it has been shown that proteolytic cleavage of the loop significantly alters channel gating (Ajouz et al., 2000), supporting our view of a critical functional role for this region.

2.4 Conclusions and Future Directions

These studies suggest that although *M. tuberculosis* and *E. coli* MscL are similar, there are important differences. Thus, caution should be exercised when employing the Tb-MscL crystal structure to explain functional results for Ec-MscL. Most strikingly, mutations at A20 in Tb-MscL do not exhibit a GOF phenotype, despite the extreme sensitivity of the aligned G22 in *E. coli*. Additionally, the loop region of Tb-MscL appears highly sensitive to mutations, suggesting that the loop region in general and the R45•••Q51 intersubunit hydrogen bond in particular, merit further investigation.

Using the alignment of Figure 2, there is no obvious Ec-MscL analogue to the R45•••Q51 hydrogen bond seen in Tb-MscL. Technically, the alignment is L47/D53 (Ec-MscL numbering), which is not a favorable interaction. There is no cationic or hydrogen bond donating residue near L47 that could pair with D53. However, residues on either side of D53 are hydrophobic, suggesting that perhaps the ion pair of Tb-MscL is replaced by a hydrophobic contact such as L47/I52 or L47/F54 in Ec-MscL. It would be interesting to investigate this possibility.

The differences between the families of MscL homologues obtained from sequence analysis and those obtained from circular dichroism analysis are quite intriguing. In order to get a clear understanding of observed families, experimental examination of additional MscL homologues is needed. Preliminary comparison of the circular dichrosim data with reported electrophysiology data (Moe et al., 1998) did not yield an explanation of the circular dichrosim family classification. However more detailed electrophysiology may allow for the rationalization of these families.

Significant differences clearly exist between Tb-MscL and Ec-MscL, although further comparisons, such as those described in Chapter 5, are still needed to fully understand the variations in these channels. Structural difference between Tb-MscL and Ec-MscL may exist in the loop as well as other regions of the protein. Designed cross-linking reactions provide clear evidence for the validity of the Tb-MscL crystal structure, and the high homology exhibited between the transmemberane domains of Tb-MscL and Ec-MscL suggest the Ec-MscL has a similar overall architecture.

2.5 Materials and Methods

2.5.1 Sequence Analysis

Multiple sequence alignments were obtained using AMPS (Alignment of Multiple Sequences)(Barton, 1990; Barton and Sternberg, 1987) and consensus group analysis was performed using MEME (Multiple EM for Motif Elicitation).(Bailey and Elkan, 1994; Bailey and Gribskov, 1998) The alignment was broken into regions–extracellular loop, carboxy terminus, and transmembrane regions one and two–using the helix definitions of

Chang *et al*.(Chang et al., 1998) The extracellular loop is defined as the region between the first and second transmembrane domains, and the carboxy terminus is the region from the end of the second transmembrane domain to the end of the carboxy helix. Pairwise alignments of the various regions were performed using AMPS, and scores for each pair were summarized as contour plots. Scores reflect the alignment of sequence A to sequence B relative to a shuffled sequence B and are therefore corrected for length. Scores above 5 indicate very good alignment between two protein sequences, scores between 2 and 5 indicate moderate alignment, and scores below 2 indicate poor alignment.

2.5.2 Constructs, Strains, and Cell Growth

All mutations were generated from a pET 19b (Novagen) construct containing the *M. tuberculosis* MscL open reading frame (Chang et al., 1998) using the QuikChange Method (Stratagene). Mutations were confirmed by enzymatic digest and sequencing. Expression and growth studies were carried out in BL21(DE3) *E. coli* using an MscL knockout mutant (Chang et al., 1998). All bacterial growth was done in the presence of 100 μg/mL ampicillin.

Growth studies were carried out as previously described (Yoshimura et al., 1999). Cells were grown in LB media to an OD_{600} of approximately 0.6 and diluted to an OD_{600} of 0.2±0.02. The cells were further diluted to 10^{-3}, 10^{-4}, 10^{-5}, and 10^{-6} and spotted (5 μL) onto 12-well LB plates in the presence or absence of 1 mM IPTG. Plates were imaged and scored after 20 and 40 hours. A scoring system was developed, in which the score

for a given growth plate was incremented by one for each concentration in which growth was observed (maximum score of 4). A minimum of 11 replications from four separate dilutions were obtained for each mutant.

Protein expression was performed by growing cells to the midpoint of log phase and inducing with 0.1% IPTG and 1% lactose. Following induction, cells were grown for an additional 2 hours, harvested, and solubilized in 1% DDM, 10 mM TRIS, and 10 mM NaCl. Protein was purified on a nickel-chelation column (Qiagen) in the presence of 0.05% DDM. The resulting proteins were verified by MALDI-TOF mass spectral analysis.

2.5.3 Circular Dichroism Studies

Circular dichrosim studies were preformed on an Aviv 42a DS circular dichroism spectrometer using a strain-free circular cuvette with a pathlength of 0.1 cm. Spectra were collected between 260 nm and 185 nm and averaged over three scans. All data was collected at room temperature. Concentrations for conversion to molar elipticy units were obtained using the BioRad DC compatible protein concentration kit or the Peirce BCA protein concentration kit.

2.5.4 Cross-linking Studies

Wild-type or R45K/Q51E protein solubilized in DDM micelles was diluted to a concentration of approximately 25 μg/mL and cross-linked at 4^{o}C for 2 hours using 10 mM EDC, 10 mM DCC, 10 mM EDC/10 mM Sulfo-NHS, or 10 mM DCC/10 mM NHS.

All cross-linking reactions were quenched with SDS-PAGE loading buffer containing β-mercaptoethanol. Reaction products were run on 4-15% gradient polyacrylamide gels and visualized by Western blotting with either a 6-His Antibody (Amersham) or INDIA HisProbe-HRP (Pierce). Cysteine cross-linking reactions were performed and assayed in a similar manner on wild type and R45C/Q51C Tb-MscL. Thioethers were formed with bis-maleimide reagents (Pierce), or disulfide bonds were formed with 3 mM copper phenanthroline. For the copper phenanthroline studies β-mercaptoethanol was omitted from the loading buffer.

2.6 Literature Cited

Ajouz, B., Berrier, C., Besnard, M., Martinac, B., and Ghazi, A. (2000). Contributions of the different extramembranous domains of the mechanosensitive ion channel MscL to its response to membrane tension. Journal of Biological Chemistry *275*, 1015-1022.

Arkin, I. T., Sukharev, S. I., Blount, P., Kung, C., and Brunger, A. T. (1998). Helicity, membrane incorporation, orientation and thermal stability of the large conductance mechanosensitive ion channel from *E-coli*. Biochim Biophys Acta-Biomembr *1369*, 131-140.

Bailey, T. L., and Elkan, C. (1994). Fitting a mixture model by expectation maximization to discover motifs in bioploymers. Paper presented at: Second International Conference on Intelligent Systems for Molecular Biology (Menlo Park, California, AAAI Press).

Bailey, T. L., and Gribskov, M. (1998). Combining evidence using p-values: application to sequence homology searches. Bioinformatics *14*, 48-54.

Barton, G. J. (1990). Protein Multiple Sequence Alignment and Flexible Pattern-Matching. Methods in Enzymology *183*, 403-428.

Barton, G. J., and Sternberg, M. J. E. (1987). A Strategy For the Rapid Multiple Alignment of Protein Sequences - Confidence Levels From Tertiary Structure Comparisons. Journal of Molecular Biology *198*, 327-337.

Batiza, A. F., and Kung, C. (2000). The hydrophobicity of residue 22 is not sufficient for G22X MscL functioning upon hypotonic shock. Biophysical Journal *78*, 473A-473A.

Batiza, A. F., Rayment, I., and Kung, C. (1999). Channel gate! Tension, leak and disclosure. Structure, Folding, and Design *7*, R99-R103.

Blount, P., and Moe, P. C. (1999). Bacterial mechanosensitive channels: integrating physiology, structure and function. Trends in Microbiology *7*, 420-424.

Blount, P., Ou, X., Hoffman, R. J., and Kung, C. (1998). Characterization of randomly generated mutants of MscL, a mechanosensitive channel in bacteria, identifies a functional region of the protein. Biophysical Journal *74*, A324-A324.

Blount, P., Schroeder, M. J., and Kung, C. (1997). Mutations in a bacterial mechanosensitive channel change the cellular response to osmotic stress. Journal of Biological Chemistry *272*, 32150-32157.

Blount, P., Sukharev, S. I., Moe, P. C., Schroeder, M. J., Guy, H. R., and Kung, C. (1996a). Membrane topology and multimeric structure of a mechanosensitive channel protein of *Escherichia coli*. Embo J *15*, 4798-4805.

Blount, P., Sukharev, S. I., Schroeder, M. J., Nagle, S. K., and Kung, C. (1996b). Single residue substitutions that change the gating properties of a mechanosensitive channel in *Escherichia coli*. Proceedings of the National Academy of Sciences of the United States of America *93*, 11652-11657.

Chang, G., Spencer, R. H., Lee, A. T., Barclay, M. T., and Rees, D. C. (1998). Structure of the MscL homolog from *Mycobacterium tuberculosis*: A gated mechanosensitive ion channel. Science *282*, 2220-2226.

Cuff, J. A., and Barton, G. J. (1999). Application of enhanced multiple sequence alignment profiles to improve secondary structure prediction. Proteins *40*, 502-511.

Hase, C. C., Minchin, R. F., Kloda, A., and Martinac, B. (1997). Cross-linking studies and membrane localization and assembly of radiolabelled large mechanosensitive ion channel (MscL) of *Escherichia coli*. Biochemical and Biophysical Research Communications *232*, 777-782.

Liu, W., Deitmer, J. W., and Martinac, B. (1999). Glycine G14, the amino acid essential for electromechanical coupling in gating the MscL of *E. coli* by mechanical force. Biophysical Journal *76*, A203-A203.

Moe, P. C., Blount, P., and Kung, C. (1998). Functional and structural conservation in the mechanosensitive channel MscL implicates elements crucial for mechanosensation. Molecular Microbiology *28*, 583-592.

Moe, P. C., Levin, G., and Blount, P. (2000). Correlating a protein structure with function of a bacterial mechanosensitive channel. Journal of Biological Chemistry *275*, 31121-31127.

Oakley, A. J., Martinac, B., and Wilce, M. C. J. (1999). Structure and function of the bacterial mechanosensitive channel of large conductance. Protein Science *8*, 1915-1921.

Ou, X. R., Blount, P., Hoffman, R. J., and Kung, C. (1998). One face of a transmembrane helix is crucial in mechanosensitive channel gating. Proceedings of the National Academy of Science of the United States of America *95*, 11471-11475.

Rees, D. C., Chang, G., and Spencer, R. H. (2000). Crystallographic analyses of ion channels: Lessons and challenges. Journal of Biological Chemistry *275*, 713-716.

Shapovalov, G., and Lester, H. A. (2000). Unpublished Results.

Spencer, R. H., Chang, G., and Rees, D. C. (1999). 'Feeling the pressure': structural insights into a gated mechanosensitive channel. Current Opinions in Structural Bioliogy *9*, 448-454.

Sukharev, S., Betanzos, M., Chiang, C. S., and Guy, H. R. (2001a). The gating mechanism of the large mechanosensitive channel MscL. Nature *409*, 720-724.

Sukharev, S., Durell, S. R., and Guy, H. R. (2001b). Structural models of the MscL gating mechanism. Biophysical Journal *81*, 917-936.

Sukharev, S., Schroeder, M. J., and McCaslin, D. R. (1999). Re-examining the multimeric structure of the large conductance bacterial mechanosensitive channel, MscL. Biophysical Journal *76*, A138-A138.

Yoshimura, K., Batiza, A., Schroeder, M., Blount, P., and Kung, C. (1999). Hydrophilicity of a single residue within MscL correlates with increased channel mechanosensitivity. Biophysical Journal *77*, 1960-1972.

Chapter 3: A High-Throughput Screen for MscL Channel Activity and Mutational Phenotyping

3.1 Introduction

The crystal structure of the mechanosensitive channel of large conductance from *M. tuberculosis* (Tb-MscL) (Chang et al., 1998) provides unique opportunities to study structure-function relationships for ion channels in general and mechanosensitive ion channels specifically. This structure opens new doors for computational studies and modeling of ion channels. Recently, both open state modeling and molecular dynamics simulations have been applied to MscL (Elmore and Dougherty, 2001; Gullingsrud et al., 2001; Sukharev et al., 2001a; Sukharev et al., 2001b). Despite the great potential of these methods, experimental evidence for the behavior predicted by these methods is essential if these tools are going to play a role in modern ion-channel structure-function analysis. Without extensive experimental testing, the models and simulations, which seek to explain in atomic detail the function of MscL, are of little value.

Current methods for assaying MscL function are either difficult, tedious, or both. As such, obtaining the large amounts of functional data required for a full understanding of the molecular mechanism by which MscL gates seems at this point in time unrealistic. Adler and Kung's adaptation of patch-clamp electrophysiology to the study of mechanosensitve channels in bacteria has proved very valuable for gaining detailed information about MscL gating (Martinac et al., 1987). Electrophysiological characterization of *E. coli* MscL (Ec-MscL) in both bacterial spheroplasts and reconstituted lipid vesicles has demonstrated that MscL is opened by tension from the lipid bilayer (Sukharev et al., 1994); shown quantitatively the tension required to open MscL (Sukharev et al., 1999); predicted the pore size of the open channel(Cruickshank et

al., 1997); and suggested that there are several discreet steps on the opening pathway (Sukharev et al., 1999). This technique has provided exquisite information about both the wild-type channel and many point mutations (Blount et al., 1997; Blount et al., 1996; Ou et al., 1998; Yoshimura et al., 1999). However such data are difficult to obtain and are not amenable to large-scale mutational screening. A screen for large-scale mutational analysis would be advantageous in efforts to understand the specific functions of the different regions of the MscL channel.

3.1.1 Phenotypical Characterization

Electrophysiological characterization of MscL has lead to two distinct mutational phenotypes. These phenotypes have been termed gain of function (GOF) and loss of function (LOF). Gain of function mutations exhibit either a decrease in the tension required to open MscL, increase the probability of spontaneous MscL openings, or both. Loss of function mutations cause MscL to open either with greater tension or cause MscL not to open at all. Idealized electrophysiology as a function of applied tension is shown in Figure 3.1 for MscL forms that are phenotypically wild type, GOF, and LOF.

3.1.2 Classical Growth-based Assays

Since patch clamp analysis is infeasible for mutational screening, growth-based methods have been developed to screen MscL mutations. Two phenotypical screens were designed and correlated with electrophyiological data (Batiza and Kung, 2000; Blount et al., 1997; Maurer et al., 2000; Moe et al., 2000; Ou et al., 1998; Yoshimura et al., 1999). The first screen for gain of function mutations simply observes bacterial growth, while

the second screen for loss of function mutations observes the consequences of osmotic downshock on bacterial growth.

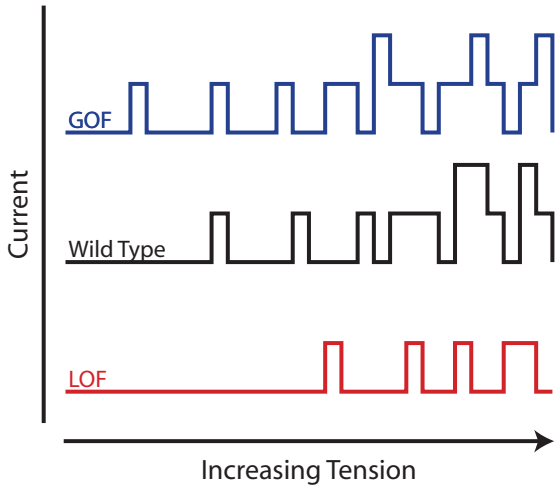

Figure 3.1: Idealized electrophysiological traces showing phenotypically wild type, GOF and LOF MscL mutants.

Gain of function mutations have been phenotypically characterized by decreased bacterial growth, presumably because the leaky channel compromises membrane integrity. Quantitatively, the assay has been performed both in liquid media and on solid media. In all cases the studies are carried out in a MscL null bacterial strain that contains the MscL gene of interest on an inducible plasmid. For liquid media, bacterial growth after induction is monitored by changes in the optical density of the bacterial culture. GOF mutants show both a slight change in the shape of the growth curve and a decrease in the steady state optical density (Blount et al., 1997; Moe et al., 2000; Ou et al., 1998; Yoshimura et al., 1999). If a solid medium is used, a comparison is made between bacterial grown on the medium in the presence and absence of an inducing agent. Gain of function mutations are identified either by poor growth or no growth in the presence of

the inducer.(Blount et al., 1997; Maurer et al., 2000; Ou et al., 1998; Yoshimura et al., 1999) Figure 3.2 shows a schematic representation of the classical gain of function assay.

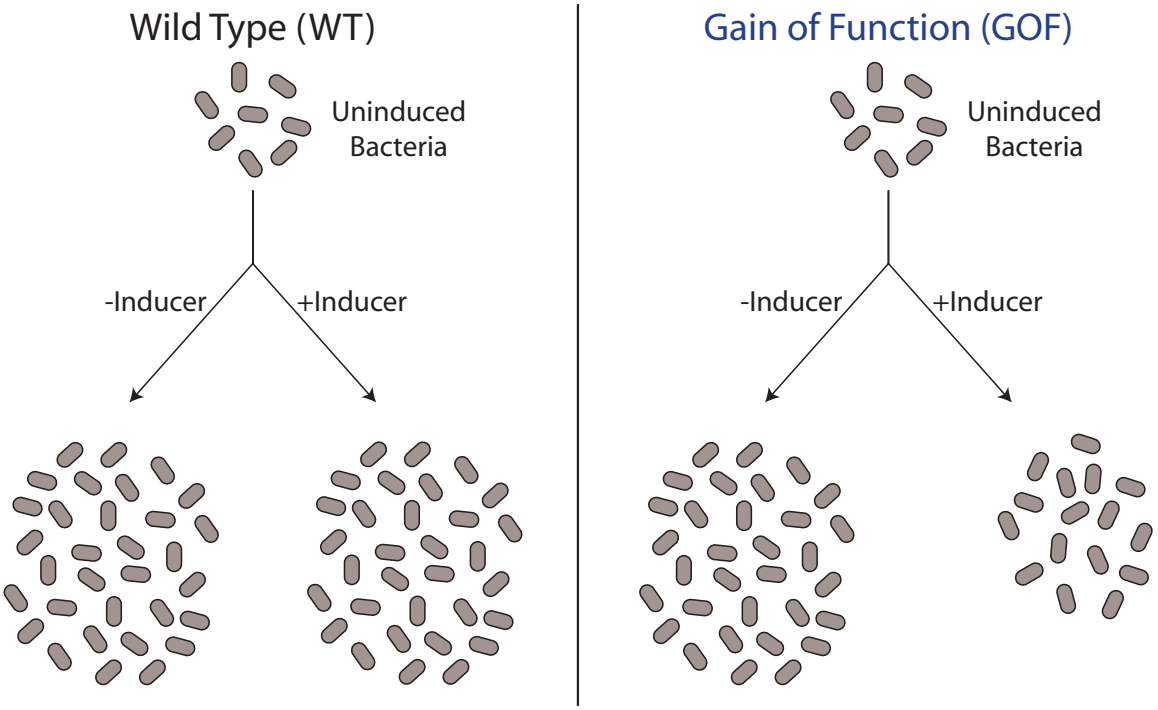

Figure 3.2: Schematic representation of the classical gain of function assay. Gain of function mutations, in an inducible plasmid, show decreased growth in the presence of the inducer when compared to wild type.

Loss of function mutations have been phenotypically characterized by bacterial death upon exposure to hypotonic shock. These experiments must be carried out in bacteria that lack both the MscL gene and the MscS (mechanosenesitive channel of small conductance) gene, since MscS alone has been demonstrated to rescue bacteria from osmotic downshock (Levina et al., 1999). As with the GOF assay the MscL gene of interest is introduced to the bacterial strain on an inducible plasmid. Typically, these experiments are carried out by downshocking both induced and uninduced bacterial

cultures, calculating the number of colony forming units following downshock, and determining the relative survival rate for a particular mutation (Batiza and Kung, 2000; Moe et al., 2000). Figure 3.3 shows a schematic representation of the classic loss of function assay.

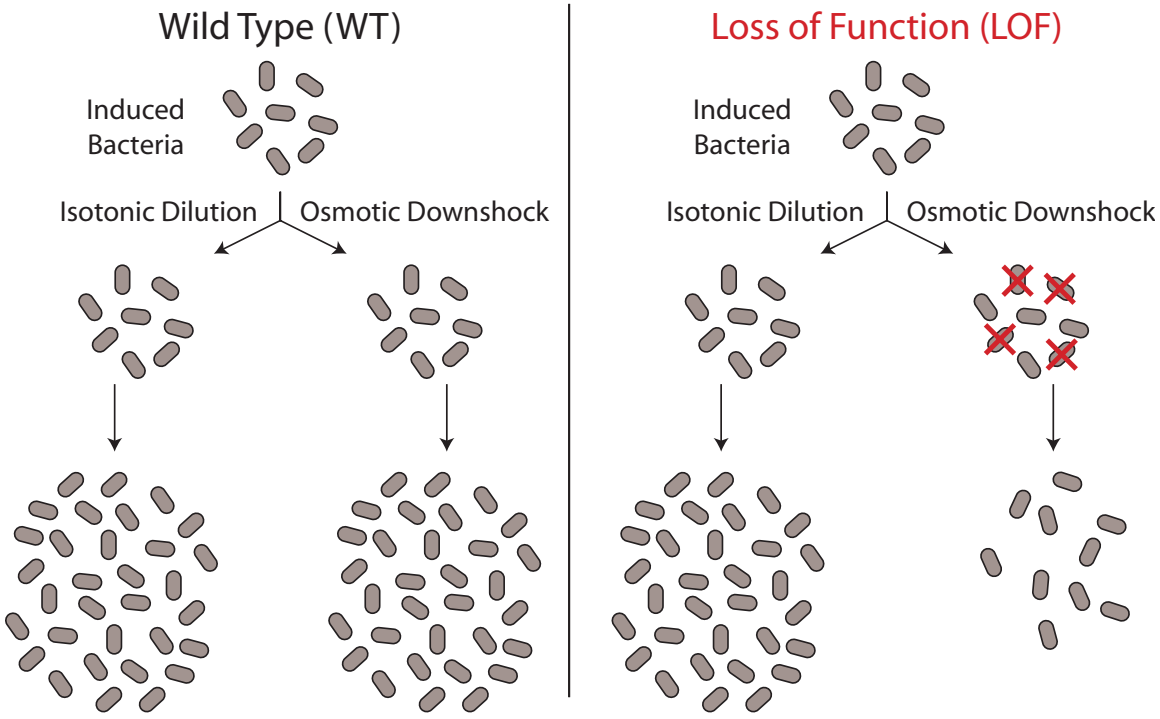

Figure 3.3: Schematic representing that classic growth-based loss of function assay. Loss of function mutations expressing MscL show a decreased survival from osmotic downshock when compared to wild type.

Despite being much easier than patch clamp electrophysiology, these methods are still tedious and time-consuming. To obtain accurate data, in both assays, great care must be taken to properly adjust the optical density of the bacterial cultures prior to the analysis. This is necessary to ensure that all samples contain an equal number of bacteria. Additionally, each mutation must be screened in two separate assays, which require

different sample preparations. In general, these methods are unattractive for screening the large number of mutations needed to fully understand MscL function.

3.2 Results and Discussion

Phenotypical screening for both LOF and GOF MscL mutants can be accomplished in a single step by modifying Molecular Probes' Live/Dead® *Bac*Light™ bacterial viability assay. The assay uses two fluorescent dyes; propidium iodide, and SYTO 9. SYTO 9 is a permeable green fluorescent dye that exhibits an increase in fluorescence upon binding to DNA. Propidium iodide is a cell impermeable, red dye that binds DNA without a fluorescence change. In this assay live bacteria exhibit green fluorescence due to the binding of SYTO 9. Bacteria with compromised cell membranes exhibit red fluorescence, since SYTO 9 is competed off the DNA by propidium iodide. Figure 3.4 shows a schematic representation of the Live/Dead *Bac*Light system and an image of bacteria stained with SYTO 9 and propidium iodide.

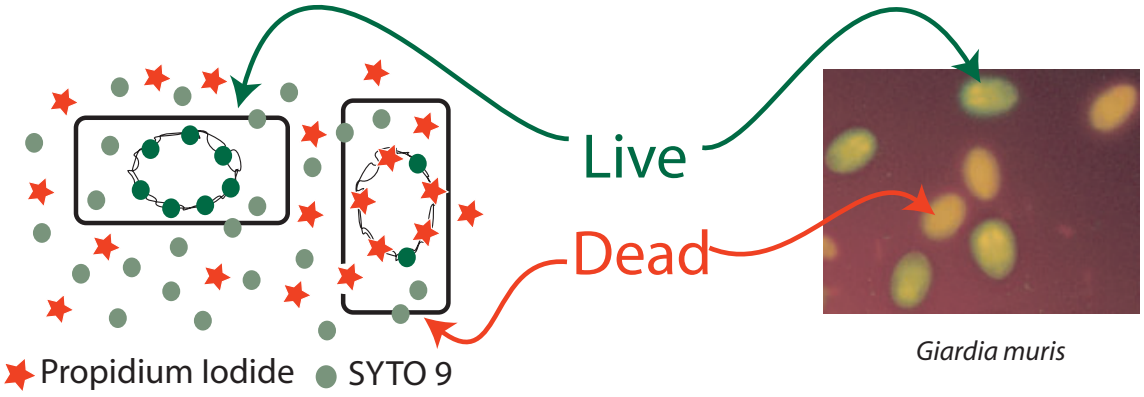

Figure 3.4: Schematic representation of the Live/Dead *Bac*Light bacterial viability assay and a fluorescent microscope image of bacteria stained with the SYTO 9 and propidium iodide (Molecular Probes, Eugene OR).

Typically, what is measured in the Live/Dead® *Bac*Light™ is the ratio of green to red fluorescence. Although this ratio can be measured using a fluorescence microscope, the measurements presented here were obtained on bacterial suspensions using a fluorescence plate reader. The resulting signal is sensitive to both the ratio of live to dead bacteria and the total number of bacteria. Sensitivity to the number of bacteria arises from the presence of excess SYTO 9.

For probing MscL function, two different comparisons of wild type vs. mutant channels are made. The first is a comparison of the relative amounts of bacteria after growth in the presence of an inducing agent; the second monitors the effects of osmotic downshock. A gain of function mutant should grow to a lower density than wild-type MscL, producing a weaker signal in an absolute sense with the Live/Dead® *Bac*Light™ assay. For loss of function mutations, one would expect increased bacterial death upon application of osmotic downshock, and thus a decrease in the green to red fluorescence ratio. These expected phenotypical differences are summarized in Figure 3.5. The great potential of this approach is its compatibility with a fluorescent plate reader. This allows both the GOF and LOF phenotype to be probed quickly and simultaneously.

It was necessary to perform this assay in defined media to prevent the interference observed for DNA binding dyes in the presence of complex media. A high osmolyte enhanced M9 (HOEM) medium consisting of 12.8 g/L $Na_2HPO_4 \bullet 7H_2O$, 3.0 g/L KH_2PO_4, 29.8 g/L NaCl, 1.0 g/ L NH_4Cl, 0.4% glucose, 1 mM $MgSO_4$, 100 μM $CaCl_2$ 10 μg/L thiamine, and 100 mg/L each of the twenty natural amino acids was used. The MJF465

bacterial strain, which is MscL, MscS (YggB), Kef A null provided an *E. coli* strain that was free of mechanosensitive ion channels.(Levina et al., 1999) The MscL constructs used were under the control of an IPTG inducible promoter, in the pB10b vector, which carries the ampicillin resistance gene.(Moe et al., 1998) Fluorescence measurements were performed using a SpectroMax Gemini XS fluorescent plate reader with dual monochrometers from Molecular Devices.

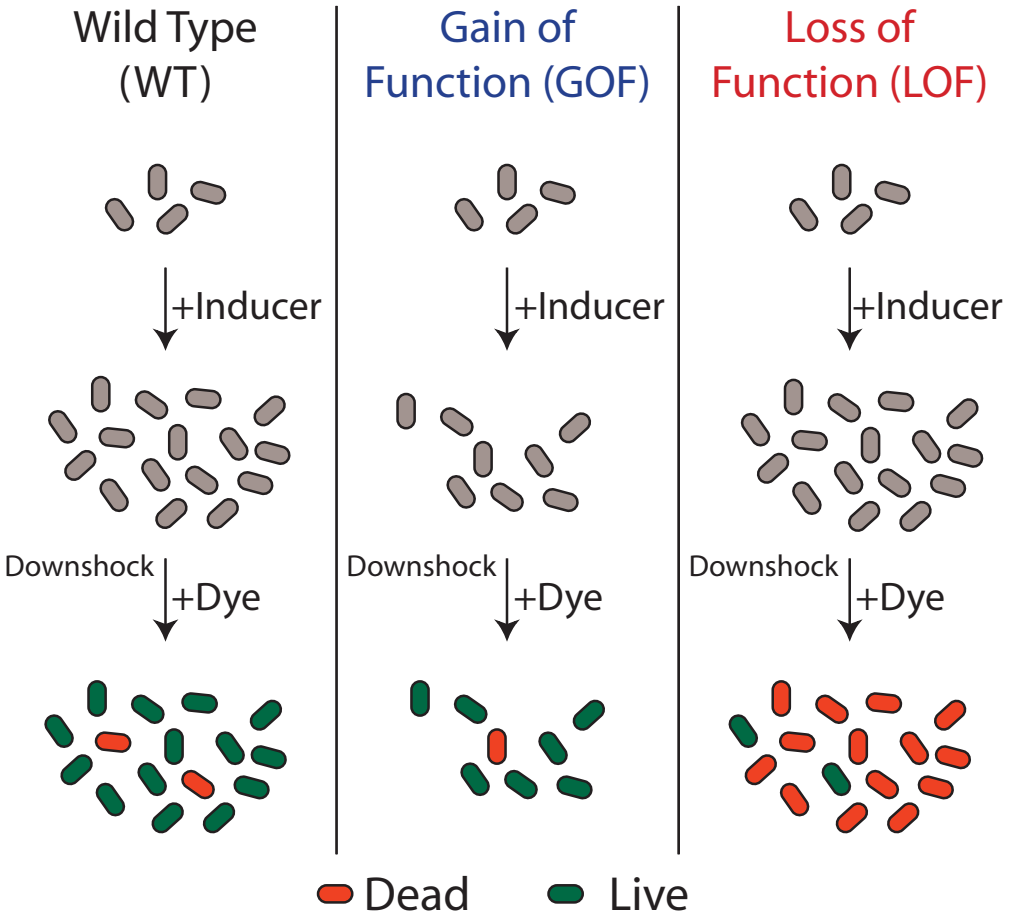

Figure 3.5: A schematic representation of the modified Live/Dead BacLight assay. Gain of function mutations show a decreased green fluorescence both in the presence and absence of an osmotic shock due to the reduced number of bacteria. Loss of function mutations show a decreased green fluorescence following osmotic downshock.

Bacterial cultures in LB medium (2 mL) with ampicillin (100 μg/mL) were seeded either from freshly streaked agar plates or frozen permastocks. The cultures were grown at 37°C for 14 hours without induction. Despite slight differences in the starting concentrations of bacteria used, at steady state the concentration of bacteria in all of the cultures were determined to be essentially equal. The LB cultures (5 μL) were then used to seed cultures in HOEM medium (1 mL) containing ampicillin (100 μg/mL) and IPTG (1mM). The HOEM cultures were grown for 7.5 hours at 37°C. In a 96-well plate the HOEM cultures (10 μL) were diluted twentyfold by addition of solutions (190 μL) of various osmotic strengths containing propidium iodide and SYTO 9 (1x concentration). Each HOEM culture was subjected to eight different downshock solutions. The downshock solutions were prepared by mixing HOEM media with water in the following ratios; 1:0, 4:1, 13:7, 1:1, 3:5, 1:3, 1:7, and 0:1. After mixing, the 96-well plate was incubated at 37°C in a plate incubator for seventy-five minutes. The plates were then read with excitation wavelengths of 480 nm and 490 nm and emission wavelengths of 500 nm and 635 nm, respectively. The assay was also performed using 384-well plates where the total volume was reduced from 200 μL to 100 μL.

The ability of the modified Live/Dead® *Bac*Light™ assay to screen MscL mutational phenotypes was assessed using wild-type Ec-MscL and a series of well characterized mutations. Mutations at G22 in Ec-MscL have been shown to dramatically alter channel gating. Substitution with hydrophilic residues at this position results in gain of function mutations, while substitution of hydrophobic residues results in loss of function mutations(Batiza and Kung, 2000; Yoshimura et al., 1999). The modified Live/Dead®

*Bac*Light™ assay was verified using wild-type Ec-MscL, G22C MscL, G22I MscL, G22N MscL, and G22S MscL. G22C MscL and G22I MscL are loss function mutations, while G22N MscL and G22S MscL are gain of function mutations. In addition, we probed bacteria transfected with the empty vector pET 14b, which provided ampicillin resistance to bacteria lacking all mechanosensitive channels.

Figure 3.6 shows the results obtained for the modified Live/Dead® *Bac*Light™ assay. Each line on the plot represents an average of six trials, starting from different initial bacterial cultures. For each culture the ratio of green to red fluorescence is plotted as a function of the extent of osmotic downshock. Standard errors among trials are shown, although they are often comparable in size to the plot marker.

The assay clearly differentiates the various MscL mutational phenotypes. Wild-type Ec-MscL shows initial upward curvature followed by a down turn at only the greatest osmotic shock. The initial upward curvature is reproducible and may be an effect of osmotic strength on the DNA binding ability of propidium iodide and/or SYTO 9. The loss of function mutations show little or no upturn, followed by a down turn with intermediate downshocks. Bacteria not expressing any mechanosensitive channels show a sharp down turn at still lower osmotic shocks. In clear contrast, the gain of function mutations show a substantially reduced initial fluorescence that is not significantly impacted by downshock.

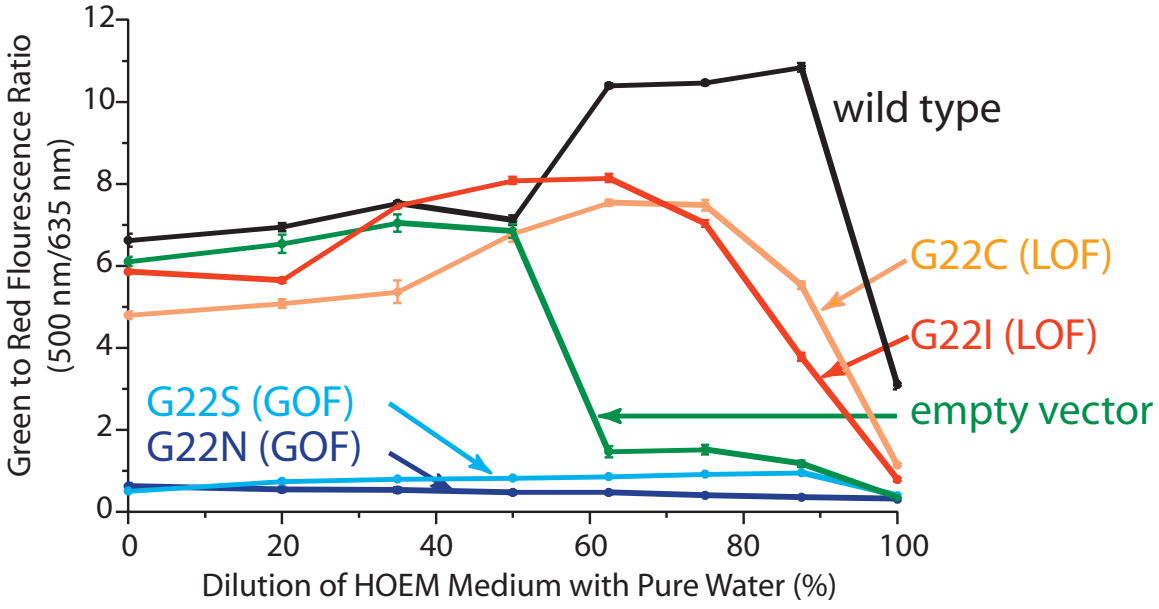

Figure 3.6: Modified Live/Dead BacLight assay for Ec-MscL mutants of known phenotype. Wild-type Ec-MscL shows an increase in the green to red fluorescence ratio with moderate osmotic downshocks followed by a decrease with severe osmotic downshocks. The loss of function mutants and the empty vector control show a decrease in the green to red fluorescence ratio for less severe osmotic downshocks than for wild type. The gain of function mutations show a decreased green to red fluorescence ratio compared to wild type for all downshock conditions.

The data in Figure 3.6 establish that the modified Live/Dead® *Bac*Light™ assay provides a quick fluorescent screen for Ec-MscL function and the differentiation of mutational phenotypes. The three patterns–upturn, followed by down turn only at very high osmotic shock; down turn at significantly less severe osmotic shock; and globally diminished growth–are completely reproducible, such that simple visual inspection allows phenotyping. In practice, though, a parallel study with wild-type MscL is always advisable.

In a 96- or 384-well plate format the assay is convenient and rapid. This assay generates both gain and loss of function data in significantly less time than required to run our

previous GOF assay alone (Maurer et al., 2000). The total time required for the assay is reduced from approximately 63 hours to approximately 23 hours. Furthermore the active working time per sample is reduced over 20-fold when a moderate number of samples is examined. With this assay a single person can easily screen over 75 different mutations in a 23 hour period.

Recently, Jones and co-workers have developed a fluorescent method for analyzing Ec-MscL and St-MscL (*S. typhimurium*) activity by monitoring the release of the fluorescent cobA protein (Jones et al., 2000). However this method is not capable of differentiating mutational phenotypes and requires extensive sample preparation prior to fluorescence analysis. Additionally, recent work suggest that small proteins may not actually efflux through MscL upon osmotic downshock; instead these proteins may leak through the transiently damaged bacterial envelope (Vazquez-Laslop et al., 2001).

3.3 Conclusions and Future Directions

This assay has the potential of generating the large amounts of functional data needed to understand the molecular mechanisms behind MscL gating. Libraries of randomly generated MscL mutants can now be quickly screened for both gain and loss of function phenotypes; the results of such a screening will be described in Chapter 4. Combination of these data with molecular dynamics simulations and molecular modeling will hopefully lead to an accurate picture of the mechanism of opening for MscL. The modified Live/Dead® *Bac*Light™ assay may also be useful in looking for open channel blockers, which could potentially help to elucidate the open state structure of MscL.

The largest drawback of the current method is that it is not compatible with Tb-MscL, since the gating tension of Tb-MscL is similar to that of an Ec-MscL loss of function mutation. Expansion of this method to a *Mycobacterium* strain may allow for analysis of Tb-MscL constructs, since some current evident suggests that membrane environment of the channel is related to gating tension (Hamill and Martinac, 2001). To that end, *Mycobacterium Smegmatis,* mc^2 155, has been identified as a potential candidate for assay development. This strain has the desired property of being non-pathogenic and a vector, pJAM2, containing an inducible promoter has been developed for protein expression (Triccas et al., 1998). Initial efforts should focus on expansion of the current assay system. However, if the live/dead *Bac*Light system is incompatible with this strain, viability can be determined using alamarBlue™ as previously described (Page et al., 1993).

3.4 Literature Cited

Batiza, A. F., and Kung, C. (2000). The hydrophobicity of residue 22 is not sufficient for G22X MscL functioning upon hypotonic shock. Biophysical Journal 78, 473A-473A.

Blount, P., Schroeder, M. J., and Kung, C. (1997). Mutations in a bacterial mechanosensitive channel change the cellular response to osmotic stress. Journal of Biological Chemistry 272, 32150-32157.

Blount, P., Sukharev, S. I., Schroeder, M. J., Nagle, S. K., and Kung, C. (1996). Single residue substitutions that change the gating properties of a mechanosensitive channel in *Escherichia coli.* Proceedings of the National Academy of Science of the United States of America 93, 11652-11657.

Chang, G., Spencer, R. H., Lee, A. T., Barclay, M. T., and Rees, D. C. (1998). Structure of the MscL homolog from *Mycobacterium tuberculosis*: A gated mechanosensitive ion channel. Science 282, 2220-2226.

Cruickshank, C. C., Minchin, R. F., LeDain, A. C., and Martinac, B. (1997). Estimation of the pore size of the large-conductance mechanosensitive ion channel of Escherichia coli. Biophysical Journal 73, 1925-1931.

Elmore, D. E., and Dougherty, D. A. (2001). Molecular dynamics simulations of wild-type and mutant forms of the *Mycobacterium tuberculosis* MscL channel. Biophysical Journal 81, 1345-1359.

Gullingsrud, J., Kosztin, D., and Schulten, K. (2001). Structural determinants of MscL gating studied by molecular dynamics simulations. Biophysical Journal 80, 2074-2081.

Hamill, O. P., and Martinac, B. (2001). Molecular basis of mechanotransduction in living cells. Physiological Reviews 81, 685-740.

Jones, S. E., Naik, R. R., and Stone, M. O. (2000). Use of small fluorescent molecules to monitor channel activity. Biochemical and Biophysical Research Communications 279, 208-212.

Levina, N., Totemeyer, S., Stokes, N. R., Louis, P., Jones, M. A., and Booth, I. R. (1999). Protection of Escherichia coli cells against extreme turgor by activation of MscS and MscL mechanosensitive channels: identification of genes required for MscS activity. Embo J 18, 1730-1737.

Martinac, B., Buechner, M., Delcour, A. H., Adler, J., and Kung, C. (1987). Pressure-sensitive ion channel in Escherichia coli. Proceedings of the National Academy of Science of the United States of America 84, 2297-2301.

Maurer, J. A., Elmore, D. E., Lester, H. A., and Dougherty, D. A. (2000). Comparing and contrasting Escherichia coli and *Mycobacterium tuberculosis* mechanosensitive channels

(MscL). New gain of function mutations in the loop region. Journal of Biolgical Chemistry 275, 22238-22244.

Moe, P. C., Blount, P., and Kung, C. (1998). Functional and structural conservation in the mechanosensitive channel MscL implicates elements crucial for mechanosensation. Molecular Microbiology 28, 583-592.

Moe, P. C., Levin, G., and Blount, P. (2000). Correlating a protein structure with function of a bacterial mechanosensitive channel. J Biol Chem 275, 31121-31127.

Ou, X. R., Blount, P., Hoffman, R. J., and Kung, C. (1998). One face of a transmembrane helix is crucial in mechanosensitive channel gating. Proceedings of the National Academy of Science of the United States of America 95, 11471-11475.

Page, B., Page, M., and Neoel, C. (1993). A new fluorometric assay for cytotoxicity measurements in vivo. International Journal of Oncology 3, 473-476.

Sukharev, S., Betanzos, M., Chiang, C. S., and Guy, H. R. (2001a). The gating mechanism of the large mechanosensitive channel MscL. Nature 409, 720-724.

Sukharev, S., Durell, S. R., and Guy, H. R. (2001b). Structural models of the MscL gating mechanism. Biophysical Journal 81, 917-936.

Sukharev, S. I., Blount, P., Martinac, B., Blattner, F. R., and Kung, C. (1994). A Large-Conductance Mechanosensitive Channel in E. Coli Encoded By Mscl Alone. Nature 368, 265-268.

Sukharev, S. I., Sigurdson, W. J., Kung, C., and Sachs, F. (1999). Energetic and spatial parameters for gating of the bacterial large conductance mechanosensitive channel, MscL. J Gen Physiol 113, 525-539.

Triccas, J. A., Parish, T., Britton, W. J., and Gicquel, B. (1998). An inducible expression system permitting the efficient purification of a recombinant antigen from Mycobacterium smegmatis. FEMS Microbiol Lett 167, 151-156.

Vazquez-Laslop, N., Lee, H., Hu, R., and Neyfakh, A. A. (2001). Molecular sieve mechanism of selective release of cytoplasmic proteins by osmotically shocked *Escherichia coli*. Journal of Bacteriology 183, 2399-2404.

Yoshimura, K., Batiza, A., Schroeder, M., Blount, P., and Kung, C. (1999). Hydrophilicity of a single residue within MscL correlates with increased channel mechanosensitivity. Biophysical Journal 77, 1960-1972.

Chapter 4: Generation and Evaluation of a Large Mutational Library from the *E. coli* Mechanosensitive Channel of Large Conductance, MscL. Implications for Channel Gating and Evolutionary Design.

4.1 Introduction

Since its cloning in 1994 by the Kung labs (Sukharev et al., 1994), the mechanosensitive channel of large conductance (MscL) has developed into a prototype ion channel for understanding cellular mechanosensation (Blount and Moe, 1999; Hamill and Martinac, 2001; Sukharev et al., 1997; Wood, 1999). Much of what is known about the function of MscL has been gained through investigation of the *E. coli* channel using electrophysiology and mutagenesis (Blount and Moe, 1999; Hamill and Martinac, 2001; Sukharev et al., 1997). Electrophysiological characterization of Ec-MscL in both bacterial spheroplasts and reconstituted lipid vesicles has: demonstrated that MscL is opened by tension from the lipid bilayer (Sukharev et al., 1994); quantitated the tension required to open MscL (Sukharev et al., 1999); predicted the pore size of the open channel (Cruickshank et al., 1997); and suggested that there are several discrete steps on the opening pathway (Sukharev et al., 1999). Mutagenesis studies also determined that the first transmembrane region of Ec-MscL lined the pore and established an occlusion of the channel in the vicinity of residue G22 (Blount et al., 1997; Blount et al., 1996; Ou et al., 1998) (Yoshimura et al., 1999).

A breakthrough in the study of MscL came with the report from the Rees labs of the high resolution crystal structure of MscL from *M. tuberculosis* (Tb-MscL) (Chang et al., 1998). This result confirmed many of the essential conclusions of the earlier mutagenesis studies, while also clarifying some confusion concerning the stoichiometry of the channel and providing a wealth of new insights into the molecular details of the structure.

The image of Tb-MscL produced by Rees and coworkers is undoubtedly of the closed state of the channel. Of the many challenges associated with the detailed study of channels and other membrane proteins, a major issue is the elucidation of the several states–open, closed, intermediate, desensitized–associated with such structures and the mechanisms of the transitions among them. For a type of bacterial K^+ channel images of the open and closed state are now available (Doyle et al., 1998; Jiang et al., 2002; Zhou et al., 2001), but this is not the case for MscL nor other channels. As such, other approaches to analyzing the open state of the channel have been employed.

Interesting results have been obtained from molecular dynamics simulations beginning from the closed state of MscL (Elmore and Dougherty, 2001; Gullingsrud et al., 2001; Kong et al., 2002). At present, however, it is not possible to run such simulations long enough to see the transition from closed to open state. As a result, the de novo construction of molecular models for the open state and various intermediates on the opening pathway has been attempted.

In particular, a detailed, atomic-level gating model for Ec-MscL has been developed by Sukharev, Guy, and co-workers (SG) (Sukharev et al., 2001a; Sukharev et al., 2001b). Although the Rees crystal structure is of Tb-MscL, SG chose to model Ec-MscL so that use could be made of the much larger collection of experimental data that exists for this homologue. These data were used extensively in developing the computational model. In addition to emphasizing key residues identified from the mutagenesis studies, the SG model naturally identified a number of other key interactions that make important

contributions in the open state and in a key intermediate state identified along the gating pathway. Recently, spin labeling studies from the Perozo lab have provided some support for the global structural model of the transmembrane domains developed by SG (Perozo et al., 2002a).

In order to test specific features of the SG model, it would be useful to evaluate the many proposed structural contacts by site-directed mutagenesis. However, the protocols for evaluating MscL mutants–either electrophysiology or growth studies–are time-consuming and tedious. Also, two distinct MscL mutant phenotypes have been identified using electrophysiology: gain of function mutations (GOF), which are mutations that open spontaneously or with less tension than required to open wild type MscL; and loss of function mutations (LOF), which are mutations that can not be gated or require more tension than wild type MscL to gate. Previous mutagenic studies, however, have almost exclusively evaluated GOF mutations only, as the LOF assay is especially tedious.

Recently, we have developed a high-throughput, fluorescence-based method for the phenotypical characterization of both LOF and GOF mutations in Ec-MscL (Maurer and Dougherty, 2001). This approach allows for the rapid screening and identification of mutations that are phenotypically wild type, gain of function, or loss of function. We now report the results of an extensive random mutagenesis study of Ec-MscL, looking at mutations with both possible phenotypes. We have greatly expanded the number of MscL mutants with an altered phenotype, especially for the LOF phenotype. These mutagensis results have been used to evaluate several key features of the SG gating

model. In addition, our mutagenesis results implicate particular regions of MscL as being involved in tension sensing and may discriminate between two proposed evolutionary models of MscL.

4.2 Results

4.2.1 The Library

A library of random mutations was created using a standard sloppy PCR protocol, as described in the Methods section. Starting with this library, 408 Ec-MscL constructs were sequenced and phenotypically screened. The resulting constructs had a modal distribution centered at 2-3 nucleotide changes per construct and one amino acid change per construct. The distribution of mutations is shown in Figure 4.1. Of the 408 sequenced constructs, 348 contained at least one amino acid change in the MscL protein.

Of the constructs that contained at least one amino acid point mutation, 64% were phenotypically wild type, 29% were phenotypically loss of function, and 7% were phenotypically gain of function. Looking only at the constructs with a single amino acid change, 74% were wild type, 20% were loss of function, and 6% were gain of function. These results are in striking contrast to previous work, which has primarily identified gain of function mutations.

As expected, increasing the number of mutations increased the probability of a channel showing an altered phenotype (GOF or LOF). Figure 4.2 shows the number of occurrences of a particular phenotype as a function of the number of amino acid point

mutations. The large number of phenotypically wild type mutations observed, coupled with the observation of phenotypically wild type constructs that contain multiple mutations (up to 7), suggests that MscL is relatively tolerant to mutation.

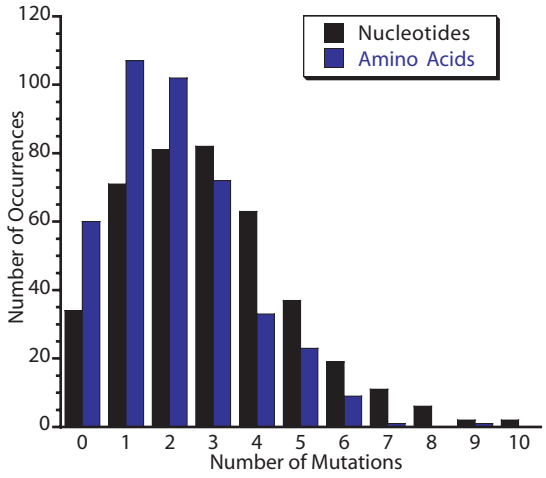

Figure 4.1: Distribution of nucleotide and amino acid mutations observed in the library of 408 sequenced Ec-MscL constructs.

Ninety percent of the amino acids that make up Ec-MscL were mutated at least once in our sequenced random mutation library. A modal distribution centered around 3 amino acid changes per Ec-MscL residue was observed (Figure 4.3). Up to seven different amino acids changes were observed at a single Ec-MscL position. Assuming a single nucleotide change per codon in Ec-MscL, there are 843 possible non-silent point mutations. Forty-six percent (390) of all possible point mutations were observed in our sequenced random mutation library.

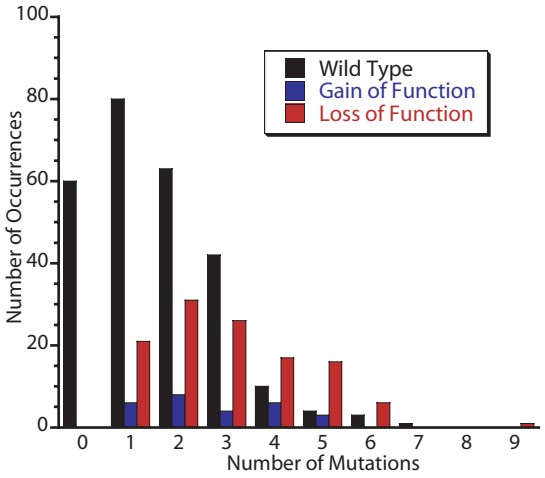

Figure 4.2: Phenotypic distribution of sequenced Ec-MscL constructs.

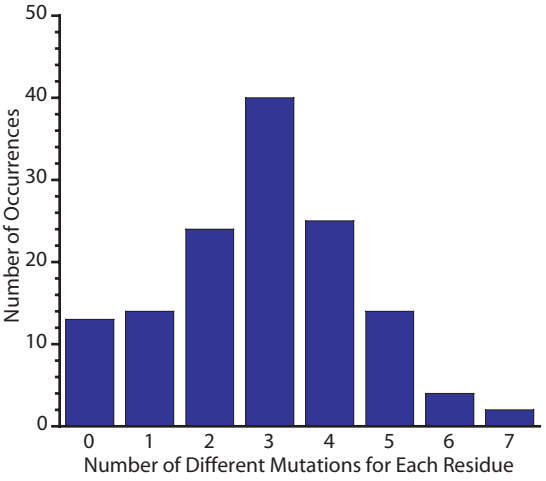

Figure 4.3: Distribution of the number of amino acid mutations observed for a given residue in Ec-MscL.

4.2.2 Evaluating Multiple Mutations

Single-site mutants are, of course, straightforward to interpret, whether they give wild type, GOF, or LOF phenotypes. On the other hand, interpreting the results for structures with multiple mutations can be challenging. If we assume that the occurrence of compensating LOF and GOF mutations is rare, multiple mutations that are phenotypically wild type arise from a collection of phenotypically wild type mutations. To test this assumption we can use the number of single-site, wild type mutations to predict the expected number of multi-site wild type mutations. That is, if 75% of single-site mutants are wild type, then we expect the fraction of double mutants that are wild type to be $(0.75)^2$. The predicted and actual fractions of wild type phenotypes for multiple mutants are shown in Figure 4.4, and the agreement is acceptable. We therefore assume that a mutation that occurs in any wild type construct is a "wild type" mutation and would produce a wild type phenotype if it occurred as a single mutant. This also means that such a mutation does not contribute to GOF or LOF phenotypes.

Constructs with multiple mutations and an altered phenotype are more difficult to interpret, since any single mutation could give rise to the observed phenotype. Pseudo-single-site, altered phenotype mutation data can be generated, however, by subtracting the wild type data from the non-wild type data. In this process, if the same mutation is observed in both a wild type construct and an altered phenotype construct, the mutation is assumed not to give rise to the altered phenotype. For example, the double mutant V23A/K117T is observed to be gain of function, and the mutation K117T is observed in a wild type construct. From this we conclude that the mutation V23A gives rise to the

observed gain of function phenotype. Additional pseudo-single-site data can be obtained by assuming that mutations to Ec-MscL beyond residue 110 are wild type. It has been shown that deletion of residues 110-136 in Ec-MscL does not dramatically alter the gating of the channel.

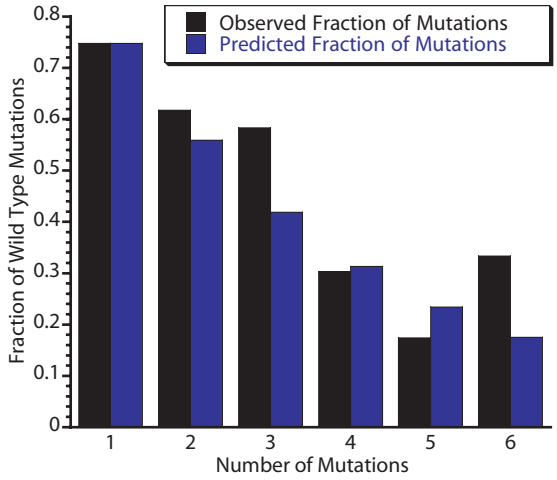

Figure 4.4: Comparisons of the observed number of phenotypically wild type mutations with the predicted number of phenotypically wild type mutations.

Similar to the analysis of wild type mutations, the number of LOF and GOF mutations can be predicted from the number of single-site mutations, using the assumption that one mutation gives rise to a particular phenotype. The number of observed mutations is again similar to the predicted value (data not shown).

The single-site and pseudo-single-site mutations that produce altered phenotypes are shown mapped onto the SG closed state structure in Figure 4.5, and the data are collected in Tables 1 and 2. Interestingly, the phenotypically altered single-site data suggest that

TM2 is functionally significant. Two new gain of function mutations are observed in this region, F83Y and L86Y, along with many loss of function mutations. With the exception of N100D, mutations in TM2 with altered phenotypes had not been observed in previous random screenings of Ec-MscL.

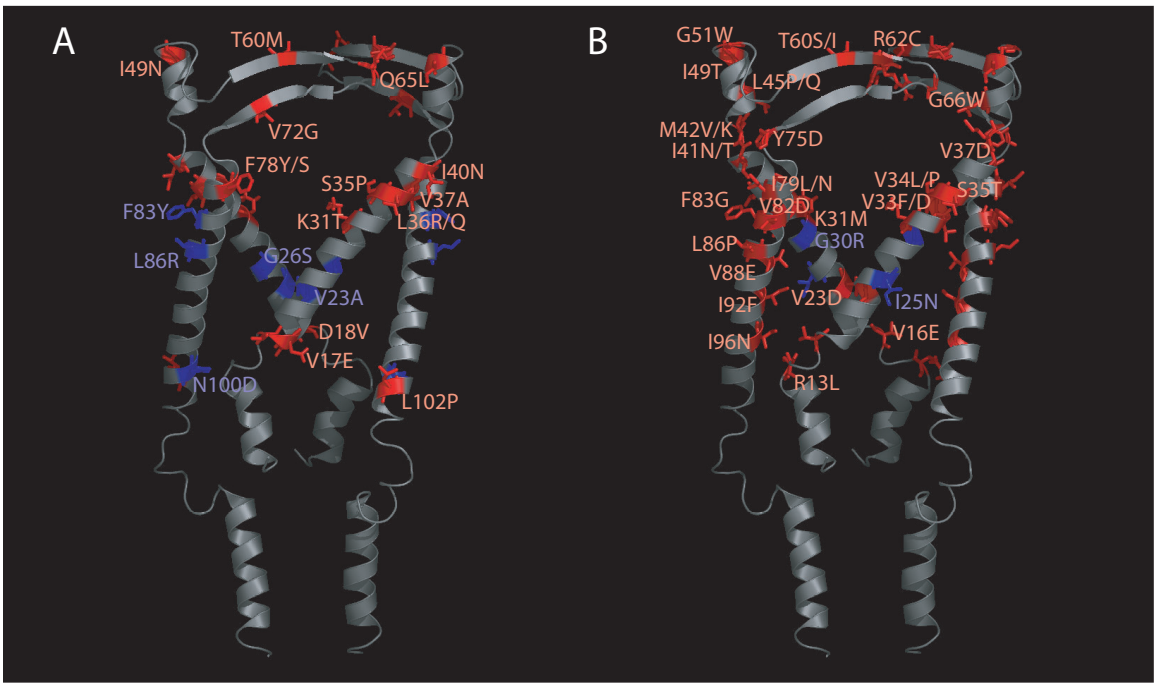

Figure 4.5: Phenotypically non-wild type mutations mapped onto the SG closed state structure. Loss of function mutations are shown in red and gain of function mutations are shown in blue. (A) Observed single-site mutations. (B) Observed pseudo-single-site mutations.

Previous work had identified roughly 30 gain of function mutations in Ec-MscL, and the 7 GOF constructs observed here add 5 new entries to that list. In contrast, previous work had identified only 10 loss of function mutants, and so the discovery of 45 new LOF mutants greatly expands the list and has significant implications for channel function and design, as discussed below. Additionally the 237 single-site wild type mutations or

pseudo-single-site wild type mutations provide additional information that was not previously available.

4.3 Discussion

Using a standard sloppy PCR protocol and a recently developed high-throughput screen, we have been able to evaluate 408 Ec-MscL constructs, of which 348 contained at least one altered amino acid. The coverage of mutations is good and fairly uniform (Figure 3a). We feel the results have significant implications for several aspects of MscL research, including the details of the SG model, possible tension-sensing regions, and some recent speculations on the evolutionary origin of MscL.

An important contribution from these studies has been the discovery of 45 new LOF mutations. Prior to this work, only 10 LOF mutants were known, all of which were variants at the G22 site that also produces GOF mutants.(Yoshimura et al., 1999) Previous studies have primarily focused on GOF mutants, no doubt because of the greater challenge in performing conventional LOF assays. The conventional LOF assay is not amenable to high-throughput screening, therefore all previously identified LOF mutations were discovered using electrophysiology. The fluorescence assay used here overcomes this problem and provides a different perspective on the relative likelihood of GOF vs. LOF mutations. Using this assay 29% of the constructs containing one or more mutations were LOF and 20% of all constructs containing precisely one mutation were LOF (Figure 1b). In sharp contrast, only 7% of all constructs containing at least one mutation were gain of function and only 6% of constructs with precisely one mutation

were GOF (Figure 1b). Of the single-site plus pseudo-single-site mutations 82% were wild type, 16% were LOF and 2% were GOF. The percentage of these mutations that are wild type is slightly higher than when considering all mutations because many of the multi-site LOF and GOF mutations could not be resolved to pseudo-single-site mutations.

4.3.1 Implications for the SG Model

The starting point for the SG model is a modified homology model of the Tb-MscL crystal structure of the closed state. A new helix (S1, see Figure 4.6) was added to the amino terminus of the protein, corresponding to a region that was not resolved in the Tb-MscL crystal structure. Also, since the loop region of MscL is not well conserved between the *E. coli* and the *M. tuberculosis* homologues, a de novo model for the Ec-MscL loop region, not based on the crystal structure of Tb-MscL, was developed. Additionally, the carboxyl terminus of the protein was adjusted to make room for the S1 region. The various regions of the model are shown in Figure 4.6a.

A key feature of the SG model is the presence of an expanded, intermediate state on the gating pathway. In this state the occlusion of the pore seen in the crystal structure is broken, but an occlusion formed by the modeled S1 helices remains. This pre-expanded state was considered necessary to explain the electrophysiology of Ec-MscL. Figure 4.6b, 1.6c, and 1.6d show a top view of the SG model for the closed, expanded intermediate, and open states, respectively.

Table 1 – Conserved Residues in the SG Model

Wild Type Residue	Closed State Interactions	Pre-expanded State Interactions	Open State Interactions	Observed Wild Type Mutations	Observed Gain of Function Mutations	Observed Loss of Function Mutations
S1 Helix						
E6	F7, R8	F7, R8, K130	G22, I25, G26	D		
F7	I3, E6, F7, F10	I3, E6, F7, F10	A89, I92, F93, I96, L129	S, C, L		
R8	E6, E107	E6, D127, K130, E131, Q132	R126, D127, L129, K130, E131			
E9	A11, R13, K106	All, R13, R126, K130	R126, K130	T, G		
F10	F7, F10, N15, D18, L19	F7, F10, All, R13	G14, I25, A28, F29, I32, F85, A89, I92	L, I		
All	E9, R13, N15	E9, F10, R13	I125, R126, L129	V		
R13	E9, A11, G14, N15, V17, D18, N100	E9, F10, A11, D18, L19, I25	D18			L
G14	E9, R13, V16, D18	E9, L19, I25, L122, I125, R126	F10, F29			
First Transmembrane Domain (TM1)						
N15	E9, F10, R13, D18	D18, L122, E118, E119, R126		S, Y, K		
V16	G14, D18, V21, G22, I96	F29, F85, L122, E119	L36, F78	M, A		E
V17	R13, G22, I96, I99	I96, I99, L129	I32, I40	A		E
D18	F10, R13, G14, N15, V16, L19	R13, N15, R126, L129, K117	R13	E		V
L19	F10, L19, D18	R13, G14, I25, F29, F85	G14, F29, V33			
A20	G22, G26, I25	F29	V33, L36, V37, I40	V		
V21	I92, I96	I92, I125, L128, L129	I3, I40, I92			
G22	V17, L19, A20	M12, L129	M1. I3. E6			
V23	V23, G26	F29, G30, V33,	M1, V33, V37	I	A	D
I24	G26, F29, I92, V88	V33, L36, V37, V88, I92	V37, I40, I41, P44	V, T	N	
I25	A20, F85, V88, A89, I92, F93	R13, L19, F85, V88, I92, I125	I3, E6, F7, F10, I92		S	
G26	A20, V23, I24	R13	E6			
A28	F85, V88	V37, V88	F10, F85, V88			
F29	I24, F85, I87, V88, A91	V16, L19, A20, V23, F85	F10, G14, L19	S, V, Y		
K31	S34, Q80, N81, D84	I41, Q80, N81, D84	Q80, N81, D84	R		T
I32	N81, F85	N81, F85	F10, V16, N81, F85	T, V		
V33	D84, I87, V88	V23, I24, A27	L19, A20, V23	A, S. I		F, D
L36	F78, N81	I24, F78, N81	V16, A20, F78, N81	P		R, Q
V37	Q80, F83, D84, I87	I24, A27, A28	A20, V23, I24			A, D
I40	M42, F78	F78, I87, V88	V16, V17, A20, V21, I24			N
Periplasmic Loop (Loop)						
M42	D39, I40, I45	M73	V71, V72, M73	G, T, I		V, K
P43	F54					
P44	F54, K55, I68. Y75	Q80	I24			
L45	M42, I68, V71, V72	V71, V72, M73	P69, A79, V71			P, Q
G51		A64, L61	Q80, F83	V, E, R		W
D53	I47, Q65	I47, K55, Y75	G76, Q80	N, E, G		
F54	P43, P44, Y75	I47, Y75	Y75, G76, I79	S, L		
Second Transmembrane Domain (TM2)						
Y75	P44, F54, I41	F54, K55, D53	F54, K55, Q56	C		D
G76			D53, F54	S		
F78	L36, D39, I40	L36, D39, I40	V16, L36	L, I		Y, S
I79			I52, F54	V		L, N
F85	I25, A28, F29, I32	V16, L19, I25, A28, F29	F10, I32	L		
I87	F29, I33, V37	I40	I47	T, V, F		
A89	I25	L121, L122, I125	F7			
A91	F29			T		
I92	V21, I24, I25	V21, I24, I25, I125	I3, F7, F10, V21, I25	T, V, L		F
F93	I25	L121, E124, I125	F7, L129	L, S		
I96	R13, V16, V17, V21	E124, I125, L128	I3, I4, F7	V, M		N
K97		E124	Q132	E, R		
N100	R13	R104, E108, A111, P113	Q132, N133	Y, S	D	
C-terminal Helix (C-Helix)						
L121	L121, L122, I125	A89, F93	M12	E, I, S		
L122	K117, V120, L121, E124	G14, N15, V16, F85, A89	M12, R13	P, Q, R		
E124	L122, I125, R126	F93, K97		G, D, K		
I125	I121, I125, E124, L128	G14, V21, I25, I92, F93, I96	A11, M12	R, N, F, V, T		
R126	E124, D127	E9, N15, D18, E118	R8, E9, D127	P, H		
D127	R126, L129	R8	R8, R126	V, G		
L128	L128, L129	V17, V21, I96, P113		S, M		
L129	D127, L128	M12, R13, D18, V21, G22	F7, R8, A11, F93	P, Q, R		

Table 2 – Non-Conserved Residues in the SG Model

Wild Type Residue	Observed Wild Type Mutations	Observed Gain of Function Mutations	Observed Loss of Function Mutations
S1 Helix			
S2	L, G, N		
I3	F, N , T, V		
I4	N, T		
K5	N, Q, R		
M12	K, L, R, T, V		
First Transmembrane Domain (TM1)			
A27	V		
G30		R	
S34	T		L, P
S35			P, T
A38	T		
D39	E, N, V		
I41	V		N, T
Loop			
G46			
L47	F		
L48	F, I, S		
I49	F, V		N, T
G50			
I52	N, V		
K55	E, I, N, R		
Q56	L. R		
F57	I, L, S, V		
A58	T		
V59	A, I		
T60	A, E, K		M, S, I
L61			
R62	L		C
D63	G, V		
A64	E, S		
Q65	R		L
G66	V		W
D67	E, G		
I68			
P69			
A70			
V71	A, I		
V72	A, I		G
M73	K, L, T, V		
H74	L, Q, R,		
Second Transmembrane Domain (TM2)			
V77	A, D		
Q80	R		
N81	D, I, S		
V82	A, P		D
F83	I, L, S	Y	G
D84	E, G, V		
L86		R	P
V88	G, L		E
F90	C, L, S, V		
M94	I, L, T, V		
A95	V		
L98			
I99	N, T		
TM2 – C-Helix Linker (Linker)			
K101	E, N, Q, R		
L102	E, Q		P
N103	D, H, K, S		
R104	W		
K105	E, N		
K106	E, R		
E107	K, V		
E108	D, G, K		
P109			
A110	T		
A111			
A112			
P113			
A114	V		
P115	Q, S		
T116	A, S		
K117	R, N		
E118	D, G, Q, V		
E119	A, D, G		
C-terminal Helix (C-Helix)			
V120	A		
T123	A, S		
K130	E, N		
E131	G		
Q132	R, P, V		
N133	D, H, I, S, Y		
N134	D, E, I, S, T		
R135	C		
S136	P, T		

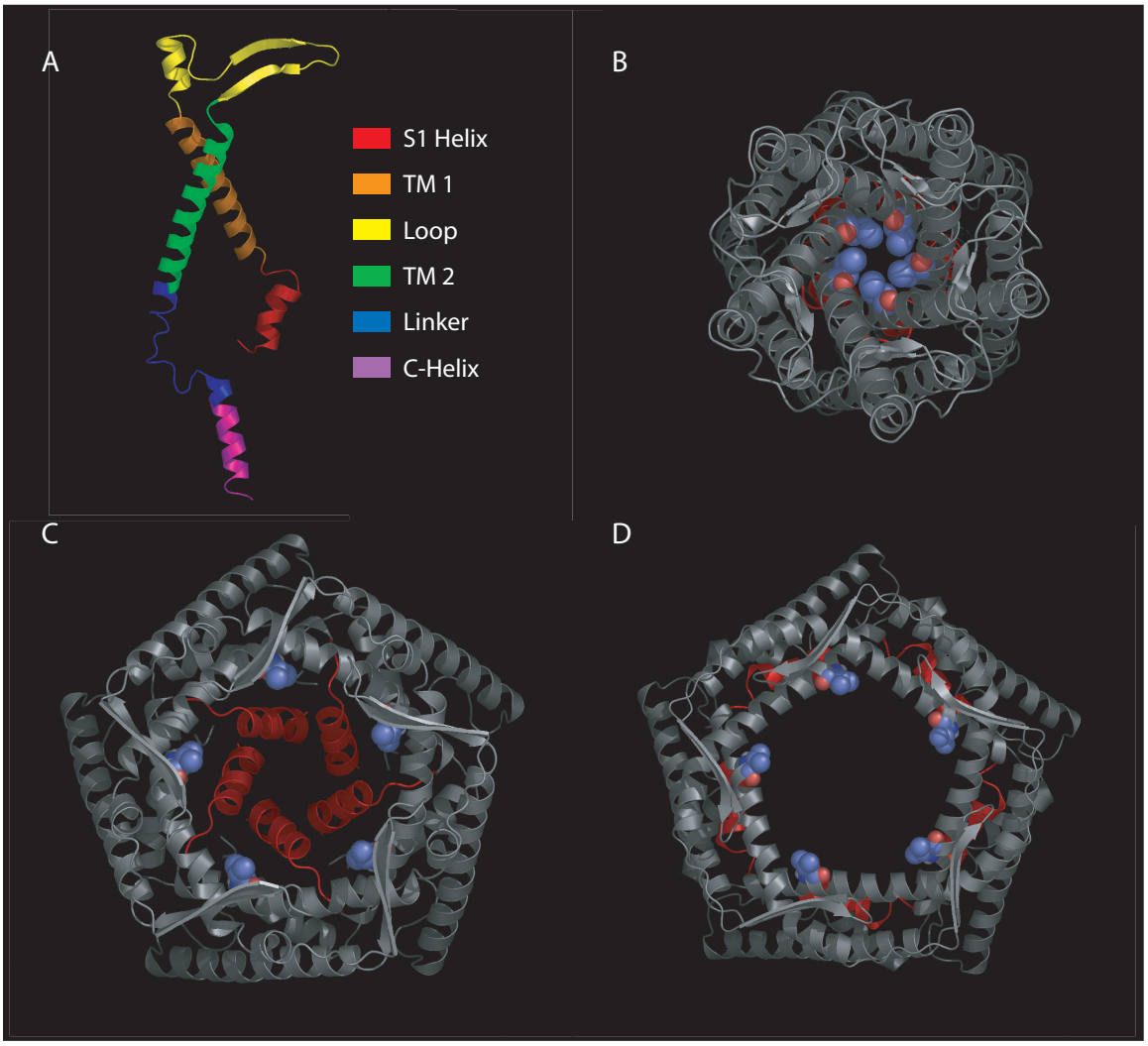

Figure 4.6: (A) A single chain of the SG closed state model highlighting the various regions of the protein. (B-D) Top views of the SG closed state model, intermediate state model, and open state model with the V23 plug shown in CPK and the putative S1 helix shown in red.

In the present work, we use specific point mutations to probe features of the SG model. It is difficult for a study of point mutations to provide compelling evidence in support of or opposed to the global structural changes inherent in the SG model, and we note that the global model for the first and second transmembrane domains has received some experimental support (Perozo et al., 2002a). Still, evaluating particular amino acids is justified by the fact that the SG model was created with a strong reliance on the

assumption that highly conserved residues are important and should be involved in complementary interactions in the closed, pre-expanded, and/or open states (Sukharev et al., 2001b). Relying on sequence conservation is inherently challenging for MscL, because conservation across the family is not nearly as extensive as is typical for homologous proteins. Also, a detailed sequence analysis from our labs (Maurer et al., 2000) produced two distinct MscL subtypes, with Tb-MscL, the sequence for which a crystal structure exists, lying in a different family from Ec-MscL, the sequence modeled by SG.

Table 1 shows the proposed interacting partners for the conserved residues in each state based on the SG model, and the mutations we have observed for these residues. It is clear from this table that many of the residues postulated to be involved in key interactions in the various states of the model can be mutated and yet still produce a wild type phenotype. This calls into question the degree to which a given interaction is essential for proper channel function. Furthermore, no direct correlation is observed between sequence conservation and mutational tolerance for a given residue. As can be seen from Table 1, mutations were observed for most of the conserved residues, with many producing a wild type channel. This is especially true for residues located in the amino and carboxyl termini of the protein. In the non-terminal regions of MscL, the number of sites having mutations that give rise to an altered phenotype is not appreciably different between the conserved (Table 1) and non-conserved residues (Tables 2).

Several attempts to correlate mutational tolerance with sequence conservation were made by applying the Rao physio-chem scoring matrix (Rao, 1986) to the observed mutational data and our sequence alignment. However, in no case was a correlation between mutational tolerance and sequence alignment observed (data not shown). These results highlight the previously noted fact that sequence conservation among the MscL channels is not high, with some tendency for homologues to cluster into specific subtypes.

4.3.1.1 The Role of S1and the Five Conserved Phenylalanines.

The SG model makes many predictions about key interactions involved in various states of MscL. SG observe five highly conserved phenylalanines in the MscL family and assign significant functional roles to all of them. The first two, F7 and F10, are proposed to reside in the hypothetical S1 helix that is not observed in the Tb-MscL crystal structure; the third phenylalanine, F29, resides in the first transmembrane domain; and the final two phenylalanines, F85 and F93, reside in the second transmembrane domain. Our data suggest that none of these residues are critical to channel function.

The SG model postulates that in the closed state F7 and F10 interact with each other to occlude the pore and serve as a secondary gate. We observe mutagenic tolerance at F7 for serine, cysteine, and leucine and mutagenic tolerance at F10 for leucine and isoleucine. While the F10 mutations could be considered conservative, those at F7 are certainly not, arguing against a key F7•••F10 interaction. Note that Sukharev *et al.,* had previously shown, using electrophysiology, that the F7C mutant was functional in the absence of disulfide formation (Sukharev et al., 2001a).

In the pre-expanded states of the SG model, it is postulated that F10 from one subunit interacts with F7, I3, and I4 of the neighboring subunit. Mutations that have been observed to be phenotypically wild type at I3 are threonine, valine, phenylalanine, and asparagine; and at I4 threonine and asparagine give wild type behavior. The significant mutagenic tolerance at these positions is supported by the observation of Blount *et al*. that residues 2-4 of Ec-MscL can be deleted without significantly altering channel function (Blount et al., 1996). These results suggest that the blockage in the pre-expanded state of the channel, which is necessary to explain the electrophysiology of MscL, may not be due to the postulated S1 helices.

As with the closed and pre-expanded states, F7 and F10 are proposed to exert significant influence over the open state. In the open state of the channel, F7 is postulated to interact with F93, and F10 is postulated to dock between F29 and F85. Again mutagenic tolerance is observed for F29, F85 and F93. Mutations of F29 to serine, valine, and tyrosine are tolerated; mutation of F85 to leucine is tolerated; and mutations of F93 to serine and leucine are tolerated. It seems unlikely that the proposed aromatic-aromatic interactions play critical roles in the function of MscL.

While one could argue that mutational tolerance at any given site might not make a compelling case, the range of conserved residues that can in fact be mutated without phenotypical consequences suggests that the S1 helix developed for the SG model may not play a crucial role in MscL function. The lack of an important functional role for the

S1 helix is in agreement with the intermediate proposed by Perozo and co-workers (Perozo et al., 2002a), however the lack of an expanded intermediate in the Perozo model does not fit well with the electrophysiology data (Sukharev et al., 1999).

4.3.1.2 An Important Aspartic Acid.

All conformations of the SG model are proposed to be stabilized by a salt bridge between R13 and D18. Interestingly, D18E is observed to be phenotypically wild type, while D18V is observed to be phenotypically loss of function. This supports the proposed importance of an acidic residue at position 18. Unfortunately, no mutations were observed for R13.

4.3.1.3 Unimportant Salt Bridges.

Two other salt bridges were specifically noted by SG as important for stabilization of the open state: R8•••D127 and E9•••R126. Clearly these salt bridges are not necessary for gating, as E9 can be mutated to glycine and threonine; R126 can be mutated to proline and histidine; and D127 can be mutated to valine and glycine, with all mutants giving a wild type phenotype. The lack of importance of these salt bridges is further highlighted by the fact that Ec-MscL truncated at position 110 is phenotypically wild type (Blount et al., 1996; Hase et al., 1997).

4.3.2 The Tension Sensor

In an effort to gain some insight into which residues are most crucial to channel function, we have mapped onto the proposed closed state structure of Ec-MscL the distribution of single-site and pseudo-single-site loss of function mutations (Figure 4.7). We assume that LOF mutants are more likely associated with key functional regions of the protein than GOF mutants, and the discovery of a large number of new LOF mutants is thus a key feature of this work. LOF mutations are clearly concentrated in the loop region and in the regions of the protein near the headgroups of the lipid bilayer. It is striking that very few loss of function mutations are observed in the middle of the transmembrane domains and that no loss of function mutations are observed in the C-terminal region.

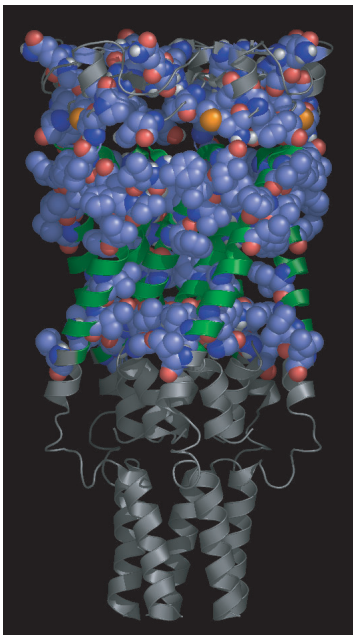

Figure 4.7: Loss of function mutations shown as CPK on the SG closed state structure.

The lipid head groups provide a means for specific protein-lipid interactions. Molecular dynamics simulations of Tb-MscL have established strong interactions between the lipid headgroups and the MscL channel (Elmore and Dougherty, 2001; Elmore and Dougherty, 2002). The same simulations have shown that the number of hydrogen bonds between the protein and the lipid varies as a function of the lipid head group.

Several lines of experimental evidence also point to a key role for lipid-protein interactions in gating mechanisms. Gating tensions for Ec-MscL in native *E. coli* membranes, which are predominately phosphatidylethanolamine, are measurably higher than gating tensions for Ec-MscL reconstituted into phosphatidylcholine (Sukharev et al., 1997), and the hydrogen bonding potentials of these two lipids are substantially different (Elmore and Dougherty, 2001; Elmore and Dougherty, 2002). Matinac and Hamill have shown that small changes in lipid chain length can greatly affect the mechanosensitive gating of gramicidin A (Martinac and Hamill, 2002). Furthermore, Perozo and Martinac have shown that reconstitution of Ec-MscL into vesicles made up of lipids with progressively shorter chain lengths results in a channel that is progressively easier to open (Kloda and Martinac, 2001; Perozo et al., 2002b). Additionally, Martinac and Hamill have argued that changes in bilayer thickness due to tension, which they estimate to be less than 1.5Å, are important for the gating of mechanosensitive channels (Hamill and Martinac, 2001; Martinac and Hamill, 2002).

Further, although less direct, support for key lipid-protein interactions, comes from the observation by Jones *et al*. that Ec-MscL gates upon heat shock (Jones et al., 2000). One

aspect of thermal adaptation for *E. coli* is a change in membrane composition, with shorter lipids being more common at higher temperatures (Bright-Gaertner and Proulx, 1972; Suutari and Laakso, 1994). In addition, significant differences in gating tensions exist between Ec-MscL and Tb-MscL, and the native lipid bilayers of *E. coli* and *M. Tuberculosis* are different (Bright-Gaertner and Proulx, 1972; Lee et al., 1996; Lugtenberg and Peters, 1976; Suutari and Laakso, 1993; Suutari and Laakso, 1994). Taken together, these experimental observations are consistent with our observation that LOF mutants are clustered near the lipid headgroups, where the interactions with the protein are the strongest.

4.3.3 The Loop

A significant number of the single-site and pseudo-single-site loss of function mutations observed for Ec-MscL are located in the loop region (Figure 4). Previous work by us and others has implicated this region as being important in MscL gating (Ajouz et al., 2000; Blount et al., 1996; Gu et al., 1998; Maurer et al., 2000). For Tb-MscL it has been shown that modification of a charged hydrogen bond in the loop results in mutations that are phenotypically gain of function. (Maurer et al., 2000) Martinac and co-works have shown that in Ec-MscL, proteolytic cleavage of the loop results in gain of function behavior for Ec-MscL (Ajouz et al., 2000). Conversely, Blount *et al*. have shown that deletion of a single residue, Q56, from the Ec-MscL loop results in a loss of function phenotype (Blount et al., 1996). This has led to the hypothesis that the loop serves as a spring connecting the first transmembrane domain and the second transmembrane

domain. The observed loss of function mutations in this region further support this hypothesis.

4.3.4 Evolutionary Arguments about Mechanosensitive Channels

Morris and co-workers have proposed two hypotheses to account for the evolution of mechanosensitive ion-channels (Gu et al., 2001; Tabarean and Morris, 2002). The first hypothesis is that mechanosensitive channels have evolved with either specialized mechanogating regions, a global structure that renders them susceptible to bilayer tension, or both. The second, less conventional, hypothesis is that mechanosensitive channels respond to bilayer tension because it has been evolutionarily impossible, undesirable, and/or unnecessary to eradicate intrinsic protein characteristics that result in mechanosensitivity. That is, mechanosensitivity is a natural feature of all membrane channels. Those channels that are not mechanosensitive, or have high tension thresholds like MscL, must have acquired special structural features to *diminish* the innate mechanosensitivity of ion channels. Morris and co-workers have argued that the second hypothesis is more compelling than the first, citing evidence that mechanosensitivity is harder to design out of a protein than to design into a protein. Their evidence for this is the mechanosensitivity of Shaker-IR and the "ample selection of MscL mutants that produce a channel more mechanosusceptible than the wild type"(i.e., GOF mutants) (Gu et al., 2001).

We assert that true mechanosensitive channels arise from the first hypothesis, and that MscL is one of these channels. Our mutational data clearly show that a mutation is much

more likely to create a *loss* of function phenotype than a gain of function. This implies that it is more difficult to design mechanosensitivity into MscL than it is to design mechanosensitivity out of MscL. As noted above, the reason that previous random mutagenesis studies of MscL did not uncover many phenotypically loss of function channels is that the screening assay used was incapable of distinguishing loss of function mutations from wild type. The hypothesis that mechanosensitivity is difficult to design into "true" mechanosensitive channels is further supported by random mutagenesis studies on MscS performed by Blount and co-workers (Okada et al., 2002). These studies show that it is extremely difficult to identify mutations that make MscS easier to gate. Additionally, our single-site and pseudo-single-site loss of function data point to a specialized mechanogating region as required by the first hypothesis. While mechanosensitivity may exist in non-mechanosensitive channels, it seems clear that "true" mechanosensitive channels have been designed to open under very specific conditions.

4.4 Conclusions

Although the general mechanism of gating proposed by SG may or may not describe the opening pathway for Ec-MscL, it seems likely that some details of the model need further refinement. Many of the highly conserved residues, which are assigned important roles in the model, can undergo dramatic mutations while preserving a phenotypically wild type channel. In particular, the putative S1 helix bundle was assigned the important role

of forming a second gate in the closed and intermediate states, but that conclusion is not supported by the data presented here.

The clustering of loss of function mutations along the lipid head groups at the top and bottom of the membrane may indicate that this region is responsible for tension sensing in MscL. Additionally, the identification of many loss of function mutations in the loop region provides further evidence that the loop serves as a transduction domain connecting the first and second transmembrane domains. In general, phenotypically altered mutations occur in the first transmembrane domain, loop, and second transmembrane domains. This argues for the importance of these regions in the gating of MscL. The putative S1 helix, the linker, and the C-terminal helix are relatively tolerant to mutation.

The mechanosusceptibility of Ec-MscL seems to be the evolutionary purpose of Ec-MscL and not just an evolutionary byproduct. MscL has a specific gating tension that can be increased or decreased by mutation. Additionally for MscL, our data show that it is easier to design mechanosensitivity out of the channel than to design mechanosensitivity into the channel.

4.5 Experimental Procedures

4.5.1 Plasmids and Strains

The Ec-MscL protein was encoded under the control of an IPTG inducible promoter in pB10b, as previously described. All experiments were carried out in the MJF465 bacterial strain that is lacking the MscL, MscS (YggB), and KefA genes.

4.5.2 Random Mutagenesis

Random Mutagenesis of Ec-MscL was performed using the Diversify PCR Random Mutagenesis Kit (CLONTECH) under buffer condition six. A standard PCR reaction using TITANIUM *Taq* DNA polymerase was carried out in the presence of 640 μM $MnSO_4$ and 80 μM dGTP. Following PCR, the reaction products were subcloned into fresh pB10b vector using the Bgl II and Xho I restriction sites.

4.5.3 Phenotypical Characterization of MscL Mutations

Phenotypical characterization of Ec-MscL mutations was carried out as previously described with slight modification to allow growth in deep 96-well plates. Single colonies resulting from the subcloned random Ec-MscL mutations were grown in a 2 mL 96-well growth block using 200 μL of LB medium supplemented with ampicillin (100 μg/mL) for fourteen hours at 37˚C in a shaking incubator (400 RPM). To prevent evaporation and allow gas exchange, the plate was covered with two sheets of 0.5 mil polyester. The LB culture (1 μL) was then used to induce a 200 μL culture in HOEM media supplemented with ampicillin (100 μg/mL) and IPTG (1 mM). The cultures were covered with polyester and grown for seven hours and forty-five minutes at 37˚C in a shaking incubator (400 RPM). In a 96-well plate the HOEM cultures (10 µL) were diluted twentyfold by addition of solutions (190 µL) of various osmotic strengths containing propidium iodide and SYTO 9 (Molecular Probes). Each HOEM culture was subjected to eight different downshock solutions. The downshock solutions were prepared by mixing HOEM media with water in the following ratios; 1:0, 4:1, 13:7, 1:1,

3:5, 1:3, 1:7, and 0:1. After mixing, the 96-well plate was incubated at 37°C in a plate incubator for ninety minutes. The plates were then read using a Gemini XS plate reader (Molecular Devices) with an excitation wavelength of 485 nm and emission wavelengths of 530 nm and 630 nm. Phenotypes were determined from the resulting downshock curves as previously described.

4.5.4 DNA Sequencing

For DNA sequencing, the remaining LB cultures were diluted with TB medium supplemented with ampicillin (100 μg/mL) and grown to saturation. Mini-prep DNA was obtained for sequencing using either a spin mini-prep kit (Qiagen), a 96-well mini-prep kit (Millipore), or using a mini-prep robot (Laragen, Inc., Los Angeles, CA or ACGT, Inc., Northbrook, IL). Big dye terminated automated DNA sequencing (ABI) was performed by either the Caltech Sequence Analysis Facility (Pasadena, CA), Laragen, Inc. (Los Angeles, CA), or ACGT, Inc. (Northbrook, IL).

4.6 Literature Cited

Ajouz, B., Berrier, C., Besnard, M., Martinac, B., and Ghazi, A. (2000). Contributions of the different extramembranous domains of the mechanosensitive ion channel MscL to its response to membrane tension. Journal of Biological Chemistry *275*, 1015-1022.

Blount, P., and Moe, P. C. (1999). Bacterial mechanosensitive channels: integrating physiology, structure and function. Trends in Microbiology *7*, 420-424.

Blount, P., Schroeder, M. J., and Kung, C. (1997). Mutations in a bacterial mechanosensitive channel change the cellular response to osmotic stress. Journal of Biological Chemistry *272*, 32150-32157.

Blount, P., Sukharev, S. I., Schroeder, M. J., Nagle, S. K., and Kung, C. (1996). Single residue substitutions that change the gating properties of a mechanosensitive channel in

Escherichia coli. Proceedings of the National Academy of Sciences of the United States of America *93*, 11652-11657.

Bright-Gaertner, E., and Proulx, P. (1972). MEtabolism of phosphoclycerides in Escherichia coli during growth at 37˚C and during a cold-induced lag phase. Biochimica Et Biophysica Acta *270*, 40-49.

Chang, G., Spencer, R. H., Lee, A. T., Barclay, M. T., and Rees, D. C. (1998). Structure of the MscL homolog from *Mycobacterium tuberculosis*: A gated mechanosensitive ion channel. Science *282*, 2220-2226.

Cruickshank, C. C., Minchin, R. F., LeDain, A. C., and Martinac, B. (1997). Estimation of the pore size of the large-conductance mechanosensitive ion channel of *Escherichia coli*. Biophysical Journal *73*, 1925-1931.

Doyle, D. A., Cabral, J. M., Pfuetzner, R. A., Kuo, A. L., Gulbis, J. M., Cohen, S. L., Chait, B. T., and MacKinnon, R. (1998). The structure of the potassium channel: Molecular basis of K+ conduction and selectivity. Science *280*, 69-77.

Elmore, D. E., and Dougherty, D. A. (2001). Molecular dynamics simulations of wild-type and mutant forms of the *Mycobacterium tuberculosis* MscL channel. Biophysical Journal *81*, 1345-1359.

Elmore, D. E., and Dougherty, D. A. (2002). Investigating mechanosensitive channel of large conductance (MscL) protein-lipid interactions with molecular dynamics simulations. Biophysical Journal *82*, 628A-628A.

Gu, C. X., Juranka, P. F., and Morris, C. E. (2001). Stretch-activation and stretch-inactivation of Shaker-IR, a voltage-gated K+ channel. Biophysical Journal *80*, 2678-2693.

Gu, L. Q., Liu, W. H., and Martinac, B. (1998). Electromechanical coupling model of gating the large mechanosensitive ion channel (MscL) of *Escherichia coli* by mechanical force. Biophysical Journal *74*, 2889-2902.

Gullingsrud, J., Kosztin, D., and Schulten, K. (2001). Structural determinants of MscL gating studied by molecular dynamics simulations. Biophysical Journal *80*, 2074-2081.

Hamill, O. P., and Martinac, B. (2001). Molecular basis of mechanotransduction in living cells. Physiol Rev *81*, 685-740.

Hase, C. C., LeDain, A. C., and Martinac, B. (1997). Molecular dissection of the large mechanosensitive ion channel (MscL) of *E. coli*: Mutants with altered channel gating and pressure sensitivity. Journal of Membrane Biology *157*, 17-25.

Jiang, Y. X., Lee, A., Chen, J. Y., Cadene, M., Chait, B. T., and MacKinnon, R. (2002). Crystal structure and mechanism of a calcium-gated potassium channel. Nature *417*, 515-522.

Jones, S. E., Naik, R. R., and Stone, M. O. (2000). Use of small fluorescent molecules to monitor channel activity. Biochemical and Biophysical Research Communications *279*, 208-212.

Kloda, A., and Martinac, B. (2001). Mechanosensitive channels in Archaea. Cell Biochemistry and Biophysics *34*, 349-381.

Kong, Y. F., Shen, Y. F., Warth, T. E., and Ma, J. P. (2002). Conformational pathways in the gating of *Escherichia coli* mechanosensitive channel. Proceedings of the National Academy of Sciences of the United States of America *99*, 5999-6004.

Lee, R. E., Brennan, P. J., and S., B. G. (1996). *Mycobacterium tuberculosis* cell envelope. Current Topics in Microbiology *215*, 1-27.

Lugtenberg, E. J. J., and Peters, R. (1976). Distribution of lipids in cytoplasmic and outer membranes of Escherichia Coli K12. Biochimica Et Biophysica Acta *441*, 38-47.

Martinac, B., and Hamill, O. P. (2002). Gramicidin A channels switch between stretch activation and stretch inactivation depending on bilayer thickness. Proceedings of the National Academy of Sciences of the United States of America *99*, 4308-4312.

Maurer, J. A., and Dougherty, D. A. (2001). A high-throughput screen for MscL channel activity and mutational phenotyping. Biochimica Et Biophysica Acta-Biomembranes *1514*, 165-169.

Maurer, J. A., Elmore, D. E., Lester, H. A., and Dougherty, D. A. (2000). Comparing and contrasting *Escherichia coli* and *Mycobacterium tuberculosis* mechanosensitive channels (MscL) - New gain of function mutations in the loop region. Journal of Biological Chemistry *275*, 22238-22244.

Okada, K., Moe, P. C., and Blount, P. (2002). Functional design of bacterial mechanosensitive channels: comparisons and contrasts illuminated by random mutagenesis. J Biol Chem *in press*.

Ou, X. R., Blount, P., Hoffman, R. J., and Kung, C. (1998). One face of a transmembrane helix is crucial in mechanosensitive channel gating. Proceedings of the National Academy of Sciences of the United States of America *95*, 11471-11475.

Perozo, E., Cortes, D. M., Sompornpisut, P., Kloda, A., and Martinac, B. (2002a). Open channel structure of MscL and the gating mechanism of mechanosensitive channels. Nature *418*, 942-948.

Perozo, E., Kloda, A., Cortes, D. M., and Martinac, B. (2002b). Physical principles underlying the transduction of bilayer deformation forces during mechanosensitive channel gating. Nature Structural Biology *9*, 696-703.

Rao, J. K. M. (1986). New scoring matrix for amino acid residue exhanges based on residue characteristic physical parameters. International Journal of Peptide and Protein Research *29*, 276-281.

Sukharev, S., Betanzos, M., Chiang, C. S., and Guy, H. R. (2001a). The gating mechanism of the large mechanosensitive channel MscL. Nature *409*, 720-724.

Sukharev, S., Durell, S. R., and Guy, H. R. (2001b). Structural models of the MscL gating mechanism. Biophysical Journal *81*, 917-936.

Sukharev, S. I., Blount, P., Martinac, B., Blattner, F. R., and Kung, C. (1994). A Large-Conductance Mechanosensitive Channel in *E. coli* Encoded by Mscl Alone. Nature *368*, 265-268.

Sukharev, S. I., Blount, P., Martinac, B., and Kung, C. (1997). Mechanosensitive channels of *Escherichia coli*: The MscL gene, protein, and activities. Annual Review of Physiology *59*, 633-657.

Sukharev, S. I., Sigurdson, W. J., Kung, C., and Sachs, F. (1999). Energetic and spatial parameters for gating of the bacterial large conductance mechanosensitive channel, MscL. Journal of General Physiology *113*, 525-539.

Suutari, M., and Laakso, S. (1993). Effects of growth temperature on the fatty acid composition of *Mycobacterium phlei*. Archives of Microbiology *159*, 119-123.

Suutari, M., and Laakso, S. (1994). Microbial fatty acids and thermal adaptation. Critical Reviews in Microbiology *20*, 285-328.

Tabarean, I. V., and Morris, C. E. (2002). Membrane stretch accelerates activation and slow inactivation in Shaker channels with S3-S4 linker deletions. Biophysical Journal *82*, 2982-2994.

Wood, J. M. (1999). Osmosensing by bacteria: Signals and membrane-based sensors. Microbiol Mol Biol Rev *63*, 230.

Yoshimura, K., Batiza, A., Schroeder, M., Blount, P., and Kung, C. (1999). Hydrophilicity of a single residue within MscL correlates with increased channel mechanosensitivity. Biophysical Journal *77*, 1960-1972.

Zhou, Y. F., Morais-Cabral, J. H., Kaufman, A., and MacKinnon, R. (2001). Chemistry of ion coordination and hydration revealed by a K+ channel-Fab complex at 2.0 angstrom resolution. Nature *414*, 43-48.

Chapter 5: The Carboxyl Terminus of the *M. tuberculosis* Mechanosensitive Channel of Large Conductance (MscL)

5.1 Introduction

The intercellular regulation of eukaryotic ion channels is a well-established phenomenon and has been observed for sodium channels (Hanlon and Wallace, 2002; Trimmer, 1998; Volk et al., 2001), potassium channels (Hanlon and Wallace, 2002; Trimmer, 1998; Vanoye et al., 2002), calcium channels (Hanlon and Wallace, 2002; Sandoz et al., 2001; Trimmer, 1998), and P2X receptors (Denlinger et al., 2001). Regulation of these channels is achieved in two fashions: through interaction of terminal regions of the channel (typically the carboxyl terminus) with an intracellular β-subunit, or through direct carboxyl terminal modulation of the channel. Interestingly, the carboxyl terminal region of TREK-1, a mechano-gated mammalian two pore potassium channel, modulates channel response to bilayer tension (Maingret et al., 1999; Maingret et al., 2000). In particular, deletion of the TREK-1 carboxyl terminus greatly decreases the response of the channel to tension.

The cytoplasmic carboxyl terminal region of the mechanosensitve channel of large conductance (MscL) is generally considered to be unimportant for channel function. Carboxyl terminal deletion studies of the *E. coli* MscL homologue (Ec-MscL), the best studied MscL isoform, showed that extensive portions of this region could be removed without altering channel function (Blount et al., 1996; Hase et al., 1997). As well, extensive mutagenesis studies, including random mutagenesis, have uncovered no functionally interesting mutants in the Ec-MscL carboxyl terminal region (Blount et al., 1997; Blount et al., 1996; Ou et al., 1998). Recently developed gating models for Ec-

MscL and *M. tuberculosis* (Tb) MscL proposed no functional role for the carboxyl terminal region of either channel (Sukharev et al., 2001a; Sukharev et al., 2001b).

However, it is unclear that carboxyl terminal results are fully generalizable between Ec-MscL and Tb-MscL. Although the overall alignment between the channels is relatively high, an early sequence analylsis by our group indicated that their carboxyl terminal regions showed little homology (Maurer et al., 2000). As well, the Ec and Tb-MscL mutagenic profiles are not identical even in regions of high homology, such as the transmembrane domains (Maurer et al., 2000).

The carboxyl terminal region in the Tb-MscL high resolution crystal structure has two intriguing features (Figure 5.1) (Chang et al., 1998). First, the 33 terminal residues are missing, since insufficient electron density was collected to build chain traces for those amino acids. Second, the portion of the Tb-MscL carboxyl terminus that is visible in the crystal structure forms a highly charged pentameric helical bundle. Computational work has implied that if all ionizable residues are charged, the helical bundle would be electrostatically unstable (Elmore and Dougherty, 2001). As well, these computations predicted that charge neutralization might allow the formation of a helical bundle. TASP studies have shown that the formation of helical domains in the Tb-MscL carboxyl terminal region may be promoted by entropic restraints imposed by the overall assembly of the channel (Kochendoerfer et al., 2002). Nonetheless, the TASP studies do not highlight which portions of the region are involved in this helical structure. Thus, both

the structure and functional relevance of the Tb-MscL C-terminal region remain ambiguous.

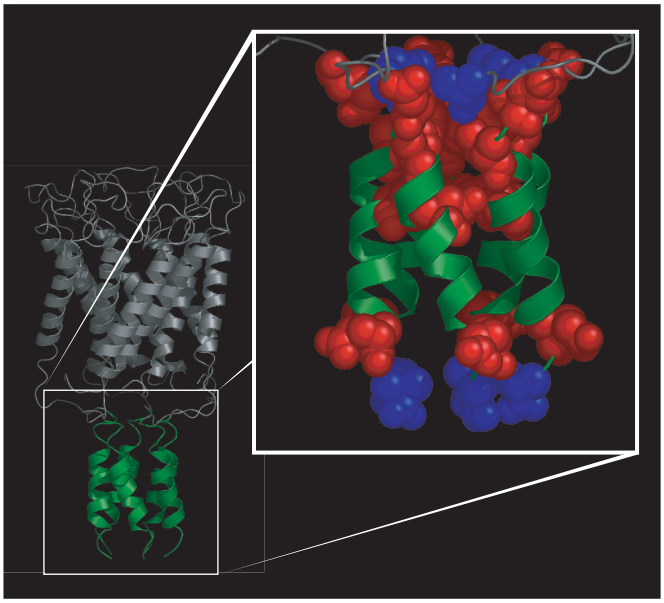

Figure 5.1: The carboxyl terminal region of the Tb-MscL crystal structure is highlighted, with all ionizable residues shown in spacefilling. Basic residues are depicted in blue and acidic residues are depicted in red.

Here we investigate the Tb-MscL carboxyl terminal region through a combination of site-directed mutagenesis, *in vivo* functional assays, and circular dichroism (CD) measurements. The utility of such *in vivo* assays in efficiently determining overall changes in MscL function upon mutagenesis has been well-established (Blount et al., 1997; Blount et al., 1996; Ou et al., 1998). In particular, mutations that reduce the tension threshold of channel gating show greatly decreased bacterial viability. These mutations commonly have been termed gain of function (GOF). Functional analysis of point mutations, in conjuction with CD measures of structural stability, establishes that

the Tb-MscL carboxyl terminal region plays an integral role in both channel structure and function.

5.2 Results

5.2.1 Growth Analysis

5.2.1.1 Deletion studies

Previous studies have shown that the carboxyl terminus of Ec-MscL can be deleted without affecting gating tension of the channel and with only minor effects on channel kinetics (Blount et al., 1996; Hase et al., 1997). However, the substantial sequence differences between MscL homologues in this region led us to investigate the carboxyl terminus of Tb-MscL (Maurer et al., 2000). Strikingly, deletion of the carboxyl terminus of Tb-MscL significantly affects channel function. Severe gain of function muations were observed upon deletion of the Tb-MscL carboxyl terminus region. The deletions and their pheotypical characterization are shown in Figure 5.2.

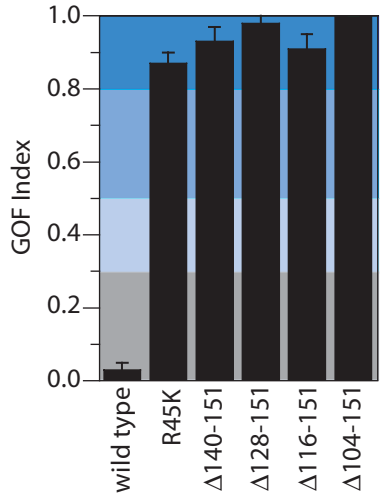

Figure 5.2: GOF index for carboxyl terminal deletion mutants of Tb-MscL.

Since the gross structural changes resulting from carboxyl terminus deletions induced hyperactivity, the effects of more subtle mutations were investigated. Initial studies focused on the negatively charged residues, since previous work had pointed to the significant charge concentration of this region (Elmore and Dougherty, 2001). Charge neutralization was undertaken by substitution of negatively charged amino acids with their neutral isosteric amide analogs; glutamic acid was replaced with glutamine and aspartic acid was replaced with asparagine. In most cases, these mutations resulted in channels that exhibited a GOF phenotype (Figure 5.3).

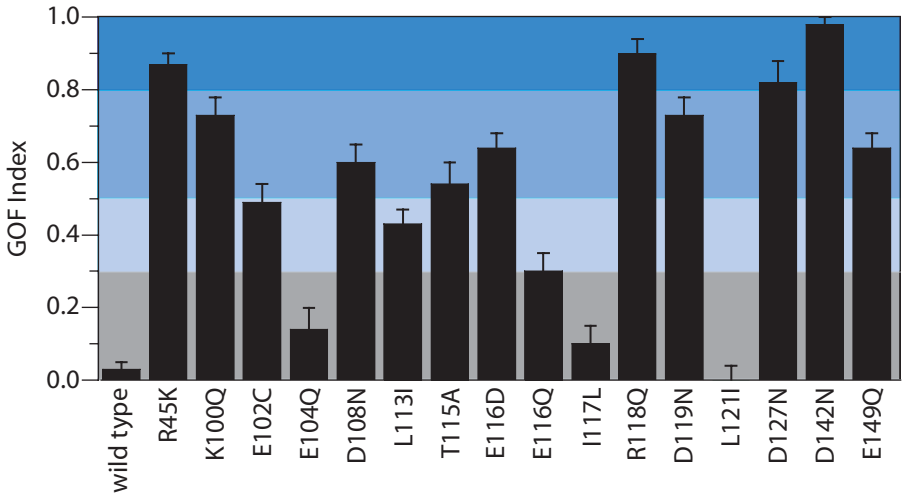

Figure 5.3: GOF index for single-site mutations in the carboxyl terminal region of Tb-MscL.

Following initial neutralization studies, mutation of some positive and neutral residues in this region was undertaken to explore the mutagenic landscape of the carboxyl terminus. Positive residues were mutated to glutamine, since this is the natural polar amino acid closest in volume. Mutations of leucine to isoleucine and isoleucine to leucine were performed as negative controls. In addition all residues of the almost universally

conserved TIERD domain that we previously identified were mutated (Maurer et al., 2000).

5.2.1.2 Ec-MscL Single-Site Mutations.

Analogous mutations to the negatively charged Tb-MscL single-site mutations were made in Ec-MscL as a control. Sites which were neutralized were Glu 107, Glu 108, Glu 118, Glu 119, Glu 124, Asp 127, and Glu 131. All of these muations showed phenotypically wild type behavior, as expected from the previous cleavage studies of the Ec-MscL carboxyl terminus.(Blount et al., 1996; Hase et al., 1997) The data are summarized in Figure 5.4.

5.2.2 Circular Dichroism Studies

Thermal denaturation was used to investigate if the Tb-MscL carboxyl terminus mutants caused structural perturbations in addition to inducing functional changes. Denaturation was monitored by the circular dichroism ellipticity at 220 nm. The denaturation curve for wild type Tb-MscL shows a single melting transition (T_m) around 60°C (Figure 5.5). A reduction of 35% in the CD signal is observed between 25°C to 95°C. Thus, significant helicity remains in the sample even after the observed transition, which most likely corresponds to the transmembrane domains. After melting, Tb-MscL regains the majority (>90%) of it original elipticity upon returning to 25°C.

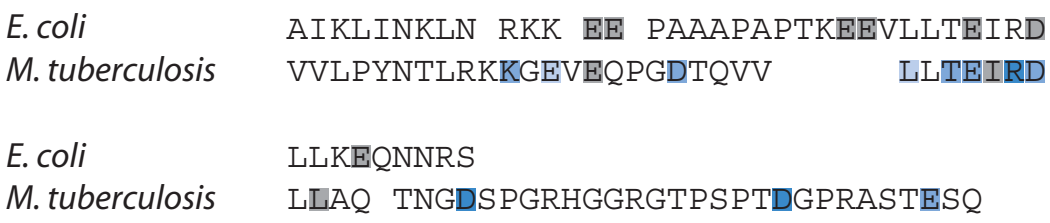

Figure 5.4: Sequence alignment of the carboxyl terminal regions of Tb-MscL and Ec-MscL. Sites at which mutation resulted in a GOF phenotype are shown in blue. The intensity of blue coloring corresponds to the GOF plots, with light blue signifying a slight GOF, medium blue indicating moderate GOF, and dark blue indicating major GOF. Sites at which mutations were phenotypically wild type channel are shown in gray.

The denaturation curves for the Tb-MscL carboxyl terminus mutants were qualitatively similar to that of wild type. However, changes in T_m arose for some mutants (Figure 5.5). In particular, major shifts in T_m to lower temperatures were noted for E116D and D142N. Conversely, the T_m shifted moderately to a higher temperature for D127N, and to slightly higher temperatures for E102C, E104Q, and D149N. Other carboxyl terminus single-point mutations showed no significant deviation in T_m from wild type Tb-MscL.

5.3 Discussion

5.3.1 Tb-MscL and Ec-MscL Are Different

Significant differences exist between the MscL homologues of *E. coli* and *M. tuberculosis*. The deletion profiles of the carboxyl terminal tail of these homologues are massively different. Additionally, we have shown that analogous single-point mutations in the carboxyl terminal region result in dramatically different phenotypic profiles for the two channels. Previously, similar results were obtained for mutations in the

transmembrane helices (Maurer et al., 2000). Recently, gating models have been proposed for both Tb-MscL and Ec-MscL by Sukharev and Guy (Sukharev et al., 2001a; Sukharev et al., 2001b.) These models do not reflect the observed differences in either the carboxyl termini or the transmembrane helices.

Additionally, these data clearly show that the Tb-MscL carboxyl terminal region plays an integral role in gating. Conversely, our controls in Ec-MscL confirm the previous observations that its carboxyl terminal region is not functionally relevant (Blount et al., 1996; Hase et al., 1997). The Sukharev/Guy model for Tb-MscL gating assigns no role to the carboxyl terminus and only includes residues 1-122. Clearly modifications of the current Tb-MscL gating model are needed to incorporate the entire carboxyl terminus and explain its functional role.

5.3.2 Structure-Function Studies of Tb-MscL

The combination of functional data with measures of structural stability for multiple mutations provides a unique opportunity to consider channel structure-function. In this study, some point mutations that exhibit an altered phenotype also exhibit changes in structural stability, however a correlation between altered phenotypic behavior and changes in structural stability is not always observed. This implies that altered phenotypic behavior does not result from the same structural phenomenon for all the mutations studied.

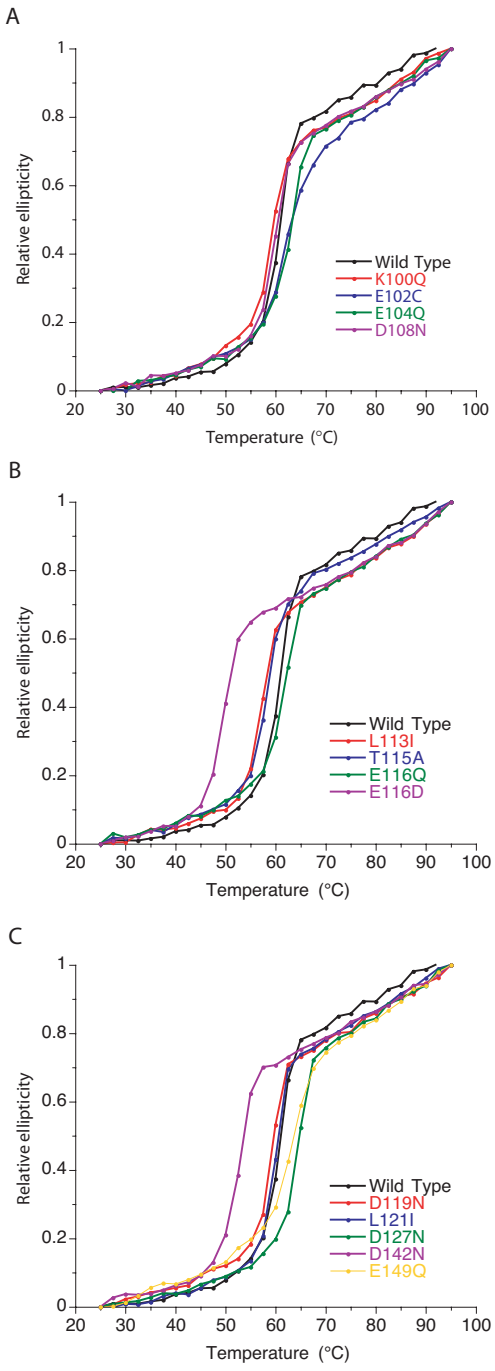

Figure 5.5: Circular dichroism thermal denaturation curves are shown for wild type Tb-MscL and a series of single-site carboxyl terminal mutations. A) Mutations in the upper portion of the crystal structure carboxyl terminal region. B) Mutations in the lower portion of the crystal structure carboxyl terminal region. C) Mutations to residues not in the crystal structure.

5.3.2.1 Upper portion of the crystal structure carboxyl terminal helix.

Only minor changes in structural stability were observed upon mutation of this region of the carboxyl terminus. However, significant functional differences are observed for mutations to this region. Most notably, Glu 104 and Asp 108 exhibit significant differences upon charge neutralization. This implies that these residues have different structural roles. However, the crystal structure proposes a similar enviroment for these residues, with both pointing toward the center of the carboxyl terminal bundle (Chang et al., 1998). Taken together, these data suggest that residues 104 and 108 may adopt slightly different conformations *in vivo* than those observed in the crystal structure.

Electrophysiological analysis of E104Q suggests that it has a lower gating tension threshold than wild type Tb-MscL. (Shapovalov, G., Bass, R., Rees, D. C., Lester, H. A., submitted.) However, one would not expect E104Q to exhibit a gain of function phenotype in our assay because its reduced gating tension is still similar to that observed for Ec-MscL. This confirms that mutations characterized as GOF in this study represent severely hyperactive MscL channels.

5.3.2.2 Lower portion of the crystal structure carboxyl terminal helix.

Mutations to all of the charged and polar residues in this region have significant functional consequences. However, changes in structural stability are only observed for E116D.

At position Glu 116 both structural and functional data were intriguing. Neutralization of Glu 116 by mutation to glutamine had no apparent effect on channel structure or

function. In striking contrast, shortening the carboxylic acid side chain by one methylene unit resulted in dramatic changes in both structural stability and channel function. Thus, residue 116 plays an important steric role in the carboxyl terminus.

Additionally, since the glutamic acid at position 116 can be mutated to the corresponding amide, this suggests that residue 116 either has a shifted pKa or that the negative charge is not important at this position. Position 108 may also exhibit a shifted pKa, since it is the only other residue in this region not to show a phenotypic effect upon charge neutralization.

Suprisingly, although no gross structural differences were observed, the apparently subtle L113I mutation shows a slight GOF phenotype. This may be explained by the lower helical propensity of isoleucine compared to leucine. As expected, the I117L mutation showed no effect.

5.3.2.3 Residues outside the crystal structure.

The structural and functional role of the Tb-MscL carboxyl terminal region is not limited to residues in the crystal structure. Mutation of residues missing from the Tb-MscL crystal structure produced channels with significant gain of function phenotypes. Specifically, the neutralization of any negatively charged residue in this region (Asp 119, Asp 127, Asp 142, or Glu 149) resulted in altered channel function. This was particularly remarkable for E149Q, which is only two residues from the end of the Tb-MscL protein.

Significant structural differences were also observed for mutations in this region. Most notably, D142N, which is only nine residues from the protein terminus, exhibited a massive shift in T_m to lower temperatures. Slight shifts to higher melting temperatures were observed for D127N and E149Q.

5.3.2.4 Speculation on the role of the Tb-MscL carboxyl terminal region.

Clearly, the Tb-MscL carboxyl terminal region plays an important role in gating. Our current data allow us to begin to create a crude working model of this region of the channel. Previous modeling has proposed a generally helical structure for the carboxyl terminus of many MscL homologues, including coiled coil regions for some species (Hamill and Martinac, 2001; Sukharev et al., 2001b). As well, TASP studies have implied that the assembled Tb-MscL carboxyl terminal region is highly helical (Kochendoerfer et al., 2002). This agrees with our observation that mutations to the carboxyl terminal region affect the thermal stability of a helical domain.

Mapping functional and structural stability data onto a helical wheel gives different results (Figure 5.6). Although the functional data show little discernable helical dependence, the structural stability data are consistent with a helical model of this region. In particular, all mutations that showed shifts in the thermal denaturation profile lie on one face of the helix.

However, we are not inclined to believe that the carboxyl terminus forms a long extended helix. This is because two different mutations separated by 25 residues both significantly

lower the melting temperature of the same transition. It seems unlikely that changing one residue on a long extended helical structure would cause such a notable change in stability, which we observe at two relatively distant sites. As well, it is less likely that helix stability would be severly compromised by single residue changes if the carboxyl terminal region primarily interacts with the membrane. Instead, it seems more reasonable that such mutations would be affecting interactions essential to the stability of a structural domain.

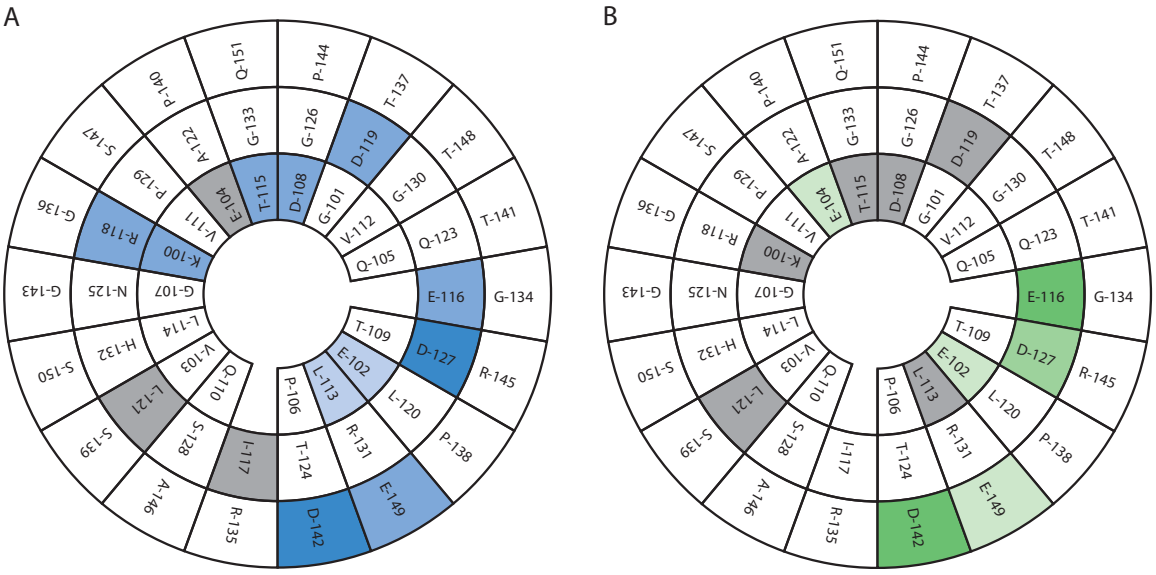

Figure 5.6: A) Helical wheel showing observed GOF phenotype for mutations in the carboxyl terminal region of Tb-MscL. Coloring corresponds to Figure 2. B) Helical wheel showing observed shifts in thermal stability for mutations in the carboxyl terminal region of Tb-MscL. Gray coloring indicates no shift, light green indicates a slight shift, medium green indicates a moderate shift, and dark green indicates a major shift.

Thus, we speculate that the carboxyl terminal region folds into a distinct subdomain such that the distal region interacts with the cytoplasmic helix visible in the crystal structure. A cartoon of such an interaction is shown in Figure 5.7. In this cartoon, the distal portion of

the carboxyl terminal region is depicted as an □-helix, based on the previously implied helicity of this region and the correspondence of our structural stability data to a helical model. However, it is quite possible that this portion of the structure adopts another well-defined conformation. In fact, secondary structure prediction programs, such as Jpred, only predict □-helicity for the upper portion of the carboxyl terminus.(Cuff et al., 1998) The high density of proline and glycine residues between sites 116 and 142 (32% of residues) would allow for the conformational arrangement needed for interactions between regions separated in sequence space. These residues may also imbue the region with the flexibility necessary for it to play an active role in the gating process. High-resolution electrophysiology on wild type and mutant channels may be extremely helpful in further refining the role this region plays during gating. For example, these techniques may be able to distinguish whether conformational changes in this region occur early or late in the gating process.

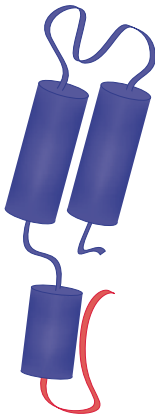

Figure 5.7: A cartoon depicted one possible conformation of a Tb-MscL single subunit. The residues in the crystal structure are shown in blue and the carboxyl terminus, which could not be resolved in the crystal structure, is shown in red.

5.3.2.5 Analogies to other ion-channel regulatory domains.

The carboxyl terminal domain of Tb-MscL plays a similar role to regulatory domains found in other eukaryotic ion channels and transporters. Similar carboxyl terminal regulation has been observed in TREK-1, a mammalian mechanosenstive ion-channel, despite low sequence homology between MscL and TREK-1 (Maingret et al., 1999; Maingret et al., 2000). This implies that perhaps carboxyl terminal regions commonly serve as regulatory domains in mechanosensitve channels.

Regulatory domains in bacterial ion channels provide useful models for understanding general aspects of eukaryotic ion-channel regulation. Intracellular regulation is common for eukaryotic ion-channels. For example, the Shaker B potassium channel exhibits amino terminus regulation, where cleavage of the regulatory domain results in a hyperactive channel (England et al., 1997; MacKinnon et al., 1993). Since bacterial channels can be easily modified and produced in very large quantities, their regulatory domains are amenable to a vast array of biochemical and biophysical techniques that are generally inaccessible to eukaryotic ion channels.

5.4 Conclusions

Here, we have further elucidated differences between homologues of the mechanosensitive channel of large conductance from *M. tuberculosis* and *E. coli*. In particular, the carboxyl terminus of Tb-MscL is an important regulatory domain, while this region has essentially no functional role in Ec-MscL. It is interesting to note that even the very end of the Tb-MscL carboxyl terminus appears critical for normal channel

regulation. This motif of intracellular regulation seems common between prokaryotic and eukaryotic ion channels.

Previously developed gating models for Tb-MscL and Ec-MscL assign no role to the carboxyl terminal domain of the channel (Sukharev et al., 2001a; Sukharev et al., 2001b). Our results support this assertion for Ec-MscL. However, these results clearly indicate that the carboxyl terminus plays a large role in Tb-MscL gating, which needs to be incorporated into future gating models.

The Tb-MscL carboxyl terminal region has provided a unique opportunity to obtain structural and functional data on a wide range of site-directed mutants of an ion channel. Currently, these sorts of studies are only feasible for bacterial ion channels, because unlike eukaryotic channels they can routinely be expressed on the scale required for many biochemical and biophysical studies.

5.5 Materials and Methods

5.5.1 *Plasmids and Strains.*

As previously described, Tb-MscL was encoded in the pET 19b vector; growth studies and protein expression were performed in MscL null *E. coli* BL21 (Chang et al., 1998; Maurer et al., 2000). Ec-MscL constructs were in the pB10b vector (Blount et al., 1996), and assays of Ec-MscL mutant function utilized the MJF465 *E. coli* strain, which is MscL, MscS, and KefA null (Levina et al., 1999). Both the pET 19b and PB10b vectors provide ampilicin resistance and IPTG control over protein expression. Site-directed

mutagenesis of both channels was performed using the QuikChange protocol (Stratagene, La Jolla, CA); all mutants were verified by sequencing and enzymatic digestion.

5.5.2 Bacterial Growth Studies.

Ec-MscL phenotypical characterization was carried out as previously described (Maurer and Dougherty, 2001). Bacterial growth studies for Tb-MscL were performed as previously described with slight modifications as noted below (Maurer et al., 2000). Frozen permastocks of Tb-MscL or Tb-MscL mutations were used to inoculate 2 mL cultures and the cultures were grown with shaking at 37˚C for 14 hours in LB media with 100 μg/mL ampicillin. The cultures were then diluted 1:10 in fresh LB media with ampicillin and grown for 1 h. Serial dilutions were performed to give dilutions of 1:10 through 1:1,000,000 in LB with ampicillin. The 1:1,000, 1:10,000, 1:100,000, and 1:1,000,000 dilutions were spotted (5 μL) onto 12-well LB agar plates with ampicillin and with or without 1 mM IPTG. The plates were grown for 20 h at 37˚C and scored as previously described. The reported GOF index was calculated by subtracting the ratio of the induced score to uninduced score from 1.

5.5.3 Protein Expression and Purification.

Frozen permastocks of Tb-MscL or Tb-MscL mutations were used to inoculate 25 mL of LB media with 100 μg/mL ampicillin. The cultures were grown overnight at 37˚C with shaking. LB cultures were used to inoculate 500 mL of TB media with ampicillin. The resulting TB cultures were grown to mid-log phase and then induced with 1 mM IPTG. After induction, the cultures were grown for an additional 2 hours at 37˚C or in some

cases for 3 hours at 30˚C. Bacteria were then pelleted, and resuspended in 50 mM Tris / 75 mM NaCl / 1% □-dodecyl maltoside (DDM) at pH 7.5 (10 mL) with Complete protease inhibitor cocktail (Roche, Indianapolis, IN). The suspensions were then probe sonicated (4 x 30 Sec.) and incubated with shaking for 1 hour at 37˚C. Following incubation, the suspensions were pelleted at 45,000 x g for 45 minutes and the resulting supernate was passed through a 0.2 μm filter. Difficulties were encountered when producing L117I and R118Q. These proteins showed extensive proteolysis of the carboxyl terminal tail that was not observed for other proteins.

All chromatography steps were carried out on a Vision Workstation (Applied Biosystems, Foster City, CA). The clarified supernate was subjected to two dimensional chromatography, using a POROS metal chelate affinity column (Applied Biosystems, Foster City, CA) charged with cobalt chloride in thebfirst dimension and a POROS HQ anion exchange column (Applied Biosystems, Foster City, CA) in the second dimension. Elution from the metal chelate column was achieved using an imidazole gradient (0.25 mM - 1 M at pH 7.5) with 0.05% DDM and elution from the HQ column was achieved using a sodium chloride gradient (0 mM – 1 M) in the presense of 10 mM Tris at pH 7.5 and 0.05% DDM. Buffer exchange and desalting were then performed using a HiPrep 26/10 desalting column (Amersham Pharmacia Biotech, Piscataway, NJ) charged with 1 mM phosphate buffer and 0.05% DDM at pH 7.2.

5.5.4 Circular Dichroism Thermal Denaturation.

All thermal denaturation was performed using an Aviv 62 DS circular dichroism spectrophotometer (Aviv Instruments, Lakewood, NJ). Purified Tb-MscL protein samples were diluted to approximately identical concentrations in 1 mM phosphate buffer (pH 7.2) for thermal denaturation. Circular dichroism scans (260-195 nm) showed equivalent helical propensities between samples. The denaturation consisted of heating from 25°C to 95°C, stepping every 2.5°C, and allowing the sample to equilibrate at each temperature for 5 min. After equilibration, the ellipticity of samples at 220 nm was measured, averaging the signal over 30 s.

5.6 Literature Cited

Blount, P., Schroeder, M. J., and Kung, C. (1997). Mutations in a bacterial mechanosensitive channel change the cellular response to osmotic stress. Journal of Biological Chemistry *272*, 32150-32157.

Blount, P., Sukharev, S. I., Schroeder, M. J., Nagle, S. K., and Kung, C. (1996). Single residue substitutions that change the gating properties of a mechanosensitive channel in *Escherichia coli*. Proceedings of the National Academy of Sciences of the United States of America *93*, 11652-11657.

Chang, G., Spencer, R. H., Lee, A. T., Barclay, M. T., and Rees, D. C. (1998). Structure of the MscL homolog from *Mycobacterium tuberculosis*: A gated mechanosensitive ion channel. Science *282*, 2220-2226.

Cuff, J. A., Clamp, M. E., Siddiqui, A. S., Finlay, M., and Barton, G. J. (1998). Jpred: A consensus secondary structure prediction server. Bioinformatics *14*, 892-893.

Denlinger, L. C., Fisette, P. L., Sommer, J. A., Watters, J. J., Prabhu, U., Dubyak, G. R., Proctor, R. A., and Bertics, P. J. (2001). Cutting edge: The nucleotide receptor P2X(7) contains multiple protein- and lipid-interaction motifs including a potential binding site for bacterial lipopolysaccharide. Journal of Immunology *167*, 1871-1876.

Elmore, D. E., and Dougherty, D. A. (2001). Molecular dynamics simulations of wild-type and mutant forms of the *Mycobacterium tuberculosis* MscL channel. Biophysical Journal *81*, 1345-1359.

England, P. M., Lester, H. A., Davidson, N., and Dougherty, D. A. (1997). Site-specific, photochemical proteolysis applied to ion channels *in vivo*. Proceedings of the National Academy of Science of the United States of America *94*, 11025-11030.

Hamill, O. P., and Martinac, B. (2001). Molecular basis of mechanotransduction in living cells. Physiological Reviews *81*, 685-740.

Hanlon, M. R., and Wallace, B. A. (2002). Structure and function of voltage-dependent ion channel regulatory beta subunits. Biochemistry *41*, 2886-2894.

Hase, C. C., LeDain, A. C., and Martinac, B. (1997). Molecular dissection of the large mechanosensitive ion channel (MscL) of *E. coli*: Mutants with altered channel gating and pressure sensitivity. Journal of Membrane Biology *157*, 17-25.

Kochendoerfer, G. G., Tack, J. M., and Cressman, S. (2002). Total chemical synthesis of a 27 kDa TASP protein derived from the MscL ion channel of *M. tuberculosis* by ketoxime-forming ligation. Bioconjugate Chemistry *13*, 474-480.

Levina, N., Totemeyer, S., Stokes, N. R., Louis, P., Jones, M. A., and Booth, I. R. (1999). Protection of *Escherichia coli* cells against extreme turgor by activation of MscS and MscL mechanosensitive channels: identification of genes required for MscS activity. Embo Journal *18*, 1730-1737.

MacKinnon, R., Aldrich, R. W., and Lee, A. W. (1993). Science *262*, 757-759.

Maingret, F., Patel, A. J., Lesage, F., Lazdunski, M., and Honore, E. (1999). Journal of Biological Chemistry *274*, 26691-26696.

Maingret, F., Patel, A. J., Lesage, F., Lazdunski, M., and Honore, E. (2000). Lysophospholipids open the two-pore domain mechano-gated K+ channels TREK-1 and TRAAK. Journal of Biological Chemistry *275*, 10128-10133.

Maurer, J. A., and Dougherty, D. A. (2001). A high-throughput screen for MscL channel activity and mutational phenotyping. Biochimica Et Biophysica Acta-Biomembranes *1514*, 165-169.

Maurer, J. A., Elmore, D. E., Lester, H. A., and Dougherty, D. A. (2000). Comparing and contrasting *Escherichia coli* and *Mycobacterium tuberculosis* mechanosensitive channels (MscL) - New gain of function mutations in the loop region. Journal of Biological Chemistry *275*, 22238-22244.

Ou, X. R., Blount, P., Hoffman, R. J., and Kung, C. (1998). One face of a transmembrane helix is crucial in mechanosensitive channel gating. Proceedings of the National Academy of Sciences of the United States of America *95*, 11471-11475.

Sandoz, G., Bichet, D., Cornet, V., Mori, Y., Felix, R., and De Waard, M. (2001). Distinct properties and differential beta subunit regulation of two C-terminal isoforms of the P/Q-type Ca2+-channel alpha(1A) subunit. European Journal of Neuroscience *14*, 987-997.

Sukharev, S., Betanzos, M., Chiang, C. S., and Guy, H. R. (2001a). The gating mechanism of the large mechanosensitive channel MscL. Nature *409*, 720-724.

Sukharev, S., Durell, S. R., and Guy, H. R. (2001b). Structural models of the MscL gating mechanism. Biophys J *81*, 917-936.

Trimmer, J. S. (1998). Regulation of ion channel expression by cytoplasmic subunits. Current Opinion in Neurobiology *8*, 370-374.

Vanoye, C. G., MacGregor, G. G., Dong, K., Tang, L. Q., Buschmann, A. S., Hall, A. E., Lu, M., Giebisch, G., and Hebert, S. C. (2002). The carboxyl termini of K-ATP channels bind nucleotides. Journal of Biological Chemistry *277*, 23260-23270.

Volk, K. A., Snyder, P. M., and Stokes, J. B. (2001). Regulation of epithelial sodium channel activity through a region of the carboxyl terminus of the alpha-subunit - Evidence for intracellular kinase-mediated reactions. Journal of Biological Chemistry *276*, 43887-43893.

Chapter 6: Introduction to Molecular Magnetism and Crystal Engineering

6.1 Introduction

The control of bulk magnetic properties has proven to be extremely difficult (Carlin, 1986; Kahn, 1993; Miller and Epstein, 1994; Turnbull et al., 1996). This is in part due to the many different types of magnetic behaviors that have been characterized. At least fourteen different magnetic behaviors have been identified in solids (Hurd, 1982). These different magnetic behaviors arise from the various spin-spin interactions observed in these materials. The complexity associated with controlling magnetic properties has arisen from difficulties in controlling the spatial arrangement of spin containing units. Here we provide an introduction to bulk magnetic behaviors, describe several strategies for controlling spin-spin organization, and expand on one of these strategies, crystal engineering. Later chapters and appendixes, in this section, provide examples of different magnetic materials that take advantage of the methods discussed here to control spin-spin interactions.

6.2 Magnetism

Magnetic materials play critical roles in our daily lives. Magnetism was first discovered by the ancient Greeks and used by the Chinese to create a “south pointing” compass (Mattis, 1981). Since the invention of the compass, the number of devices that use magnetic components has skyrocketed. A small number of the applications of magnetic materials include frictionless bearings, medical devices, magnetic separators, loudspeakers, microphones, switches, sensors, data storage devices, motors, and generators (Miller and Epstein, 1994). The extensive commercial viability of magnetic materials has driven research in this area.

Traditional magnetic materials are two- and three-dimensional arrays of inorganic atoms, composed of transition metal or lanthanide metal containing spin units. These materials are typically produced at very high temperatures using metallurgical methodologies. In contrast to traditional magnetic materials, molecular magnets are organic or inorganic/organic hybrid materials, comprised of either metal containing spin units or organic radical containing spin units. It has been postulated that these materials will allow for the low temperature synthesis of magnetic materials, materials with better optical properties, the combination of magnetic properties with mechanical, electrical, and/or optical properties, better control over a material's magnetic characteristics, and materials that can be easily processed (Miller and Epstein, 1994).

In order to design materials with interesting bulk magnetic properties it is necessary to understand how bulk magnetism arises in samples. A complete understanding of magnetism has not yet been formulated, however many of the general principles of magnetic behavior are well established. Some of those principles are reported here.

6.2.1 Diamagentism and Paramagnetism (Carlin, 1986; Kahn, 1993)

On the atomic level there exist two fundamental types of magnetism: diamagnetism and paramagnetism. All of the more complex magnetic behaviors which are observed evolve from these basic magnetic phenomena.

Diamagnetic behavior is characterized by repulsion of a substance out of an applied magnetic field. This behavior arises from the interaction of the applied magnetic field with molecular or atomic orbitals containing paired electrons. With the exception of the hydrogen radical, all atomic or molecular materials exhibit some diamagnetic behavior. This magnetic behavior is temperature independent, and the strength of the interaction is roughly proportional to the molecular weight of the material.

Paramagnetism is characterized by the attraction of a substance into an applied magnetic field. This behavior arises as a result of an interaction between the applied magnetic field and unpaired electrons in atomic or molecular orbitals. Typically, paramagnetic materials contain one or more unpaired electrons, and the strength of paramagnetic interactions are temperature dependant. However, some substances exhibit temperature independent paramagnetism (TIP) that arises as a result of a coupling between the magnetic ground state and non-thermally populated excited states. TIP has been observed for materials with both paramagnetic and diamagnetic ground states, and it is usually associated with electrically conducting materials.

Classically, the term magnetism refers to substances that at the atomic level exhibit temperature dependant paramagnetic behavior and will thus be used in this context. The non-zero spin angular moment associated with an unpaired electron gives rises to a magnetic moment. Upon pairing, electrons within an orbital exhibit opposing magnetic moments, resulting in no net magnetic moment. In general, bulk magnetic properties arise as a result of long-range interactions between unpaired electrons.

6.2.2 Cooperative Magnetism

Bulk magnetic behavior arises from interactions between paramagnetic atoms or molecules. These interactions can create materials that are either magnetic or non-magnetic, depending on how adjacent magnetic spins align with each other. Over 14 different possible magnetic interactions have been described in the literature (Hurd, 1982). Several of the important types of magnetic interactions are presented below.

6.2.2.1 Dimensionality

Although magnetic interactions occur in three dimensions, the type and strength of these interactions can be different in each dimension. This gives rise to magnetic materials with one cooperative interaction type in one dimension and different cooperative interaction types in the other two dimensions. Typically in cases where different magnetic interactions are observed due to dimensionality, the material is characterized by the strongest interaction.

6.2.2.2 Paramagnetism, Antiferromagnetism, Ferromagnetism, and Ferrimagnetism (Carlin, 1986; Kahn, 1993)

Generally, the bulk magnetic behavior of a material can be described by one of the four major classes of magnetism. The major classes of magnetism are paramagnetism, ferromagnetism, antiferromagnetism, and ferrimangetism. These classes of magnetic behavior describe how adjacent magnetic moments would interact with each other at absolute zero. The interactions are shown in Figure 6.1 and described below.

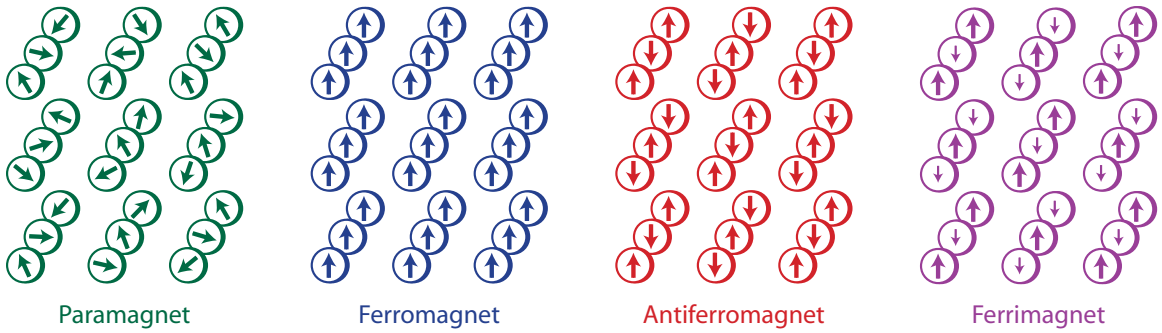

Figure 6.1: The alignment of magnetic moments at absolute zero for the four principle classes of magnetism. No alignment of adjacent magnetic moments is observed for paramagnets. Ferromagnets exhibit parallel alignment of adjacent magnetic moments. Antiferromagnets exhibit antiparallel of adjacent magnetic moments. Ferrimagnets are composed of two magnetic spins of different strength and exhibit antiparallel alignment.

Paramagnetism. In a paramagnetic material each individual electron spin is unaffected by its neighbors. The spins of a paramagnetic material can easily be aligned by an applied magnetic field. However the alignment is weak, and upon removal of the magnetic field the system relaxes back to a random distribution of magnetic moments. True paramagnetic materials are extremely rare, since most materials exhibit one of the other three principle classes of magnetism at very low temperatures.

Ferromagnetism. Ferromagnetism is characterized by parallel alignment of adjacent magnetic spins that results in a large net magnetic moment. Ferromagnetic alignment of adjacent magnetic spins is rare since it can only be achieved if there is zero quantum mechanical overlap between the spin-containing orbitals. In this case alignment of the spins, which correlates their motions and minimizes electron-electron repulsions, is the most stable state. Unlike paramagnets, ferromagnets exhibit a net magnetic moment in the absence of an applied magnetic field.

Antiferromagnetism. In an antiferromagnet, magnetic spins are aligned antiparallel, which results in a material with no net magnetic moment. At absolute zero, antiferromagnets exhibit a diamagnetic response to an applied magnetic field. The alignment of spins antiferromagnetically is analogous to the process of bonding and is thus favorable. Antiferromagnetism is the most commonly observed bulk mangnetic behavior, and long-range antiferromagnetism is even exhibited by materials that order locally ferromagnetically.

Ferrimagnetism. Ferrimagnetism is a special case of antiferromagnetism, where the material consists of a lattice of rigidly alternating spins of different magnitudes. As in antiferromagnetism, the adjacent magnetic spins align antiparellel. However, since the adjacent spins are of different magnitudes, the resulting material exhibits a net magnetic moment in the absence of an applied magnetic field. Ferrimagnetism is responsible for the magnetism in magnetite, where Fe(III) ions, S=5/2, are observed to alternate with Fe(II) ions, S=2.

Although the four major class of magnetism account for the majority of observed magnetic behaviors, many other classes of magnetism exist. Many of these classes are subtle variations of the previously described major classes of magnetism. For example, a three dimensional metamagnet is a two dimensional ferromagnet that orders antiferromagnetically in the third dimension upon application of low magnetic fields and ferromagnetically upon application of high magnetic fields.

6.2.2.3 Magnetic Frustration (Manson et al., 2000; Toulouse, 1977; Villain, 1977)

Magnetic frustration is typically the result of an antiferromagnetically ordered triangular lattice. If there is quantum mechanical overlap between adjacent magnetic moments, the spins align antiparallel, however if the spins are on a triangular lattice this is unattainable. As illustrated in Figure 6.2 it is impossible to align a triangular arrangement of spins, such that all spins interact antiferromagnetically. This has been termed spin frustrations, since if two of the spins align antiferromagnetically a third spin cannot be aligned antiferromagnetically with both of the spins.

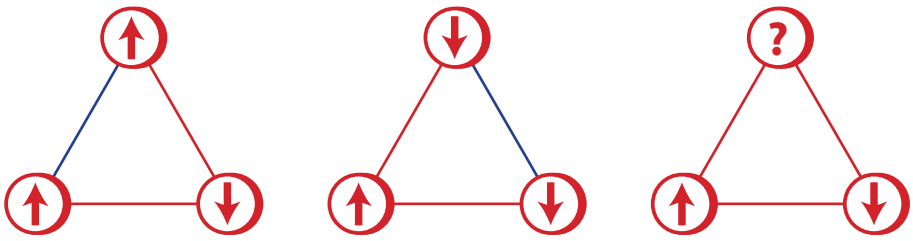

Figure 6.2: Magnetic frustration is illustrated. In the case of magnetically frustrated systems it is impossible for all spins to be align antiparellel.

6.2.2.4 Domain Structure (Bertotti, 1998; Carlin, 1986; Kahn, 1993)

Materials that exhibit a net magnetic moment, such as ferromagnets and ferrimagnets, often exist as a series of magnetic domains. Typically in the absence of an applied magnetic field, no magnetization is observed for ferromagnetic or ferrimagnetic materials. These materials generally consist of series of magnet domains with each magnetic domain having a net magnetization in the absence of an applied magnetic field. However, random orientation of the magnetic domains within a sample results in the apparent lack of magnetization in the absence of an applied magnetic field. Figure 6.3

illustrates a domain structure for a two dimensional ferromagnet. The domain structure of a sample is rearranged by application of an external magnetic field. The results of applied magnetic fields on materials that exhibit bulk magnetism is further discussed in section 6.2.3.2.

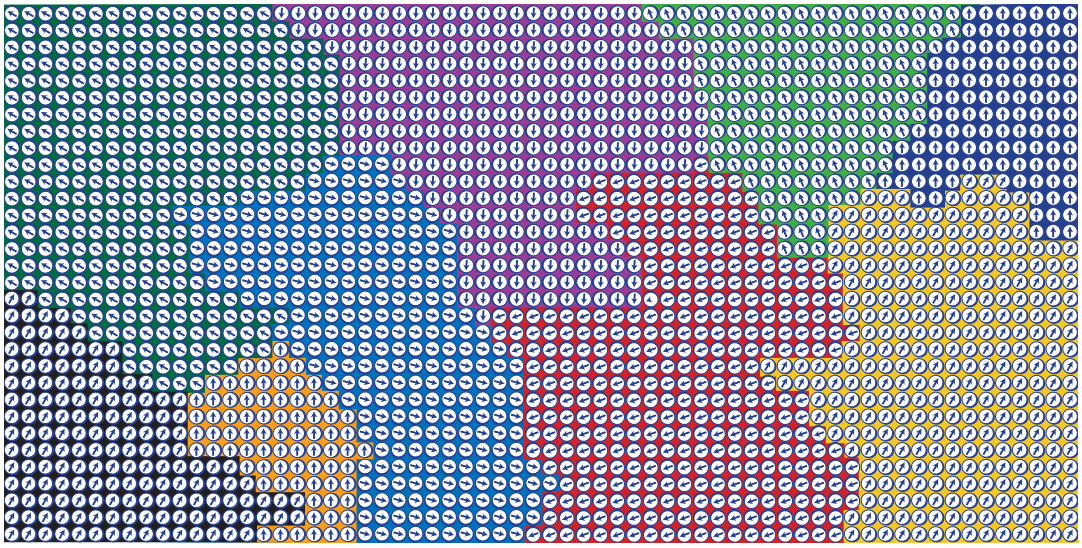

Figure 6.3: The random orientation of domains within a two dimensional ferromagnetic is shown. This random orientation gives rise to an apparent lack of magnetization for these samples in the absence of an applied magnetic field.

6.2.3 Temperature and Field Dependance (Carlin, 1986; Kahn, 1993; Miller and Epstein, 1994; Turnbull et al., 1996)

Magnetic interactions are typically characterized by their responses to variations in temperature and applied magnetic field. Each of the different types of magnetic interactions described above has a characteristic response to temperature and applied magnetic field. These responses are used to determine the specific type and strength of a

magnetic interaction. The temperature and field dependence of the general classes of magnetic interactions are reviewed here.

6.2.3.1 Paramagnets

The temperature and field dependent behavior of an ideal paramagnet is well described and is useful in magnetic characterization. Paramagnets are composed of many independently acting magnetic spins. In a sample, the magnitude of the magnetic spin (S) is the molecular spin state of the paramagnetic molecule or atom. Temperature dependence in paramagnetic materials is described by the Curie law, and field dependence is described by the Brillouin function. A brief description of each of these functions is give below.

Curie Law. Before considering the temperature dependence of a paramagnetic material the concept of magnetic susceptibility (χ) must be defined. Magnetic susceptibility is the quantitative measure of the response of a material to an applied magnetic field. The definition of magnetic susceptibility is given in equation 6.1, where M is magnetization, and H is applied magnetic field.

$$\chi = \frac{M}{H} \qquad \textbf{(6.1)}$$

The Curie law (6.2) describes the temperature dependence of an ideal paramagnet, where χ_m is molar magnetic susceptibly, N is Avagadro's number, g is the "spectroscopic

splitting factor" (Landé g factor), μ_β is the Bohr magneton, and k is the Boltzman constant.

$$\chi_m = \frac{Ng^2\mu_\beta^2}{3kT} S(S+1) \qquad (6.2)$$

This equation is usually reduced to the form in equation 6.3, where C is the Curie constant. It is important to note that the Curie law is only valid when H/kT is small.

$$\chi_m = \frac{C}{T} \qquad (6.3)$$

Brillouin Function. The Brillouin Function describes the magnetization of an ideal paramagnet without regard to the magnitude of H/kT. In practice this function is used to determine the spin state of a paramagnet by varying applied magnetic field at constant temperature. The function is given below, where the variables are as defined above or by the subsequent equations 6.5 and 6.6.

$$M = Ng\mu_\beta S \bullet B_S(y) \qquad (6.4)$$

$$B_s(y) = \frac{2S+1}{2S}\coth\left(\frac{2S+1}{2S}y\right) - \frac{1}{2S}\coth\left(\frac{1}{2S}y\right) \qquad (6.5)$$

$$y = \frac{g\mu_\beta SH}{kT} \qquad (6.6)$$

Figure 6.4 shows a plot of the Brillouin function for various magnetic spin states. Using a Brillouin analysis the spin state of a material can be determined without knowing the exact chemical composition of the material, since it can be determined from the magnetization as a function of applied field and the saturation magnetization of the sample.

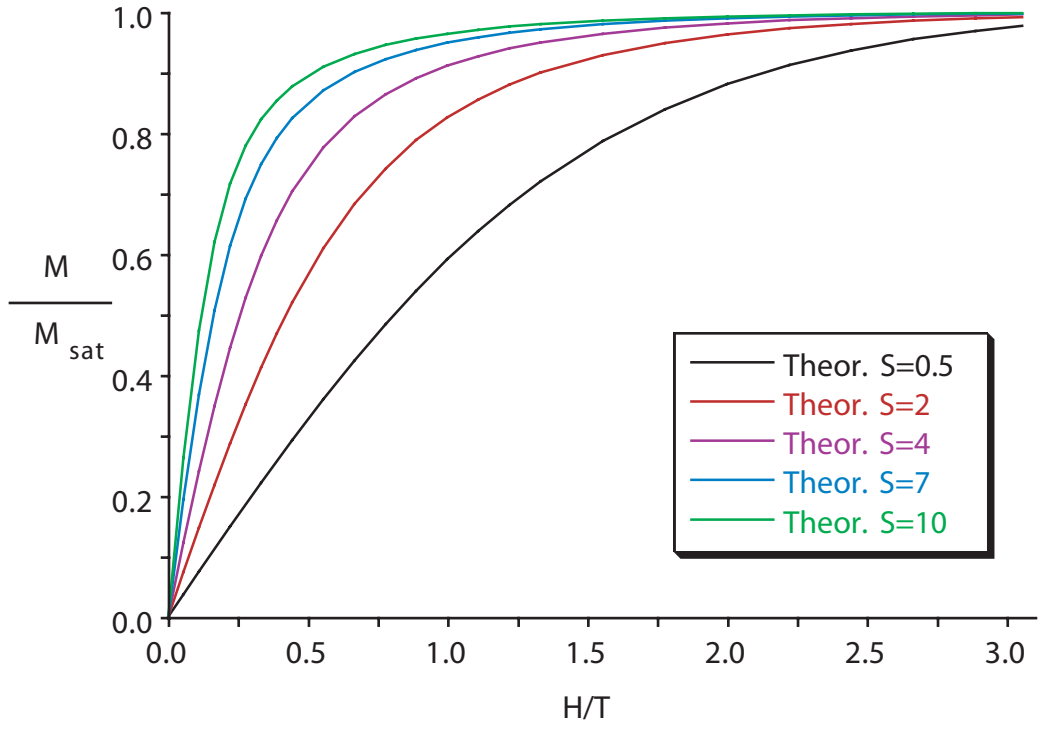

Figure 6.4: Brillouin curves for ideal paramagnets with various S values are shown. Magnetization normalized to the saturation magnetization is plotted against H/T. Systems with large S values saturate more quickly in response to increasing magnetic field than those with low values of S.

6.2.3.2 Temperature Dependence of Cooperative Magnetic Effects.

All magnetic materials behave as paramagnets at high temperatures, because thermal energy over comes the alignment and tosses the spins about randomly. The critical temperature of a material is the onset temperature for magnetic order. For a particular material the high and low temperature regimes are defined relative to the critical temperature, with the high temperature region lying above the critical temperature and the low temperature region lying below the critical temperature. A material does not exhibit bulk magnetism until well below its critical point.

Typically, temperature dependant magnetism is observed by examining the susceptibility of a material as a function of temperature. Analysis of the properties of a particular material is carried out by examining the temperature dependence as a function of susceptibility, a function of the susceptibility temperature product, and a function of the inverse susceptibility. Each of these analyses provides slightly different information about the bulk magnetism of the material.

Susceptibility vs. Temperature. Typical plots for magnetic susceptibility as a function of temperature for ferromagnetic, paramagnetic, and antiferromagnetic materials are shown in Figure 6.5. In general, it is difficult to determine the type of magnetic interactions occurring in a sample from the plot of susceptibility as a function of temperature. The most useful information can be obtained for antiferromagnetic materials, which exhibit a maximum at low temperature. The temperature at which the maximum is observed provides information on the strength of the magnetic interactions, with stronger

antiferromagnetic interactions occurring at higher temperatures. The shape of the maximum suggests the dimensionality of interactions, with one and two dimensional antiferromagnets marked by a rounded maximum and three dimensional antiferromagnets marked by a sharp peek.

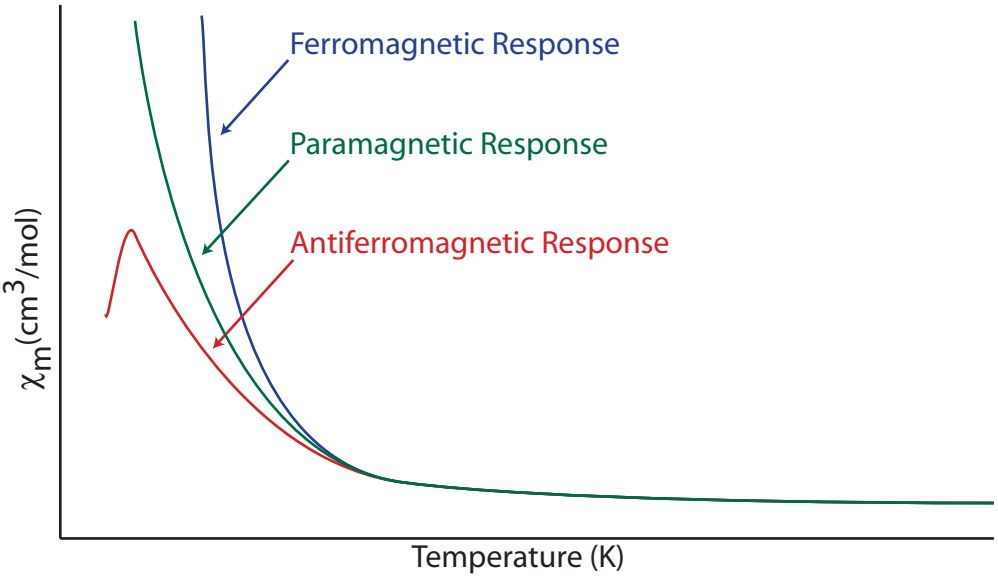

Figure 6.5: Magnetic susceptibility as a function of temperature for paramagnetic, ferromagnetic, and antiferromagnetic materials.

Susceptibility Temperature Product vs. Temperature. Analysis of the susceptibility temperature product as a function of temperature provides information about the basic interactions occurring in magnetic materials. A typical plot of susceptibility temperature product as a function of temperature is shown for an ideal paramagnet, ferromagnet, antiferromagnet, and ferrimagnet in Figure 6.6.

The temperature susceptibility product of a true paramagnetic material does not vary with temperature, while variations are observed for other types of magnetism. The invariant portion of the temperature susceptibility product at high temperatures for all types of cooperative magnetism is due to the effective paramagnetic behavior of magnetic materials above their critical temperatures. Ferromagnetic materials display an upward deviation from the curve for an ideal paramagnet as the ferromagnetic interaction energy overcomes thermal energy. Conversely, antiferromagnetic interactions display downward curvature with decreasing temperature as the magnetic moment for the sample goes to zero. For ferrimagnetic materials a slight downward curvature is first observed, due to interactions between adjacent magnetic moments. Ferrimagnetic materials then display upward curvature due to an increasing correlation length within the system.

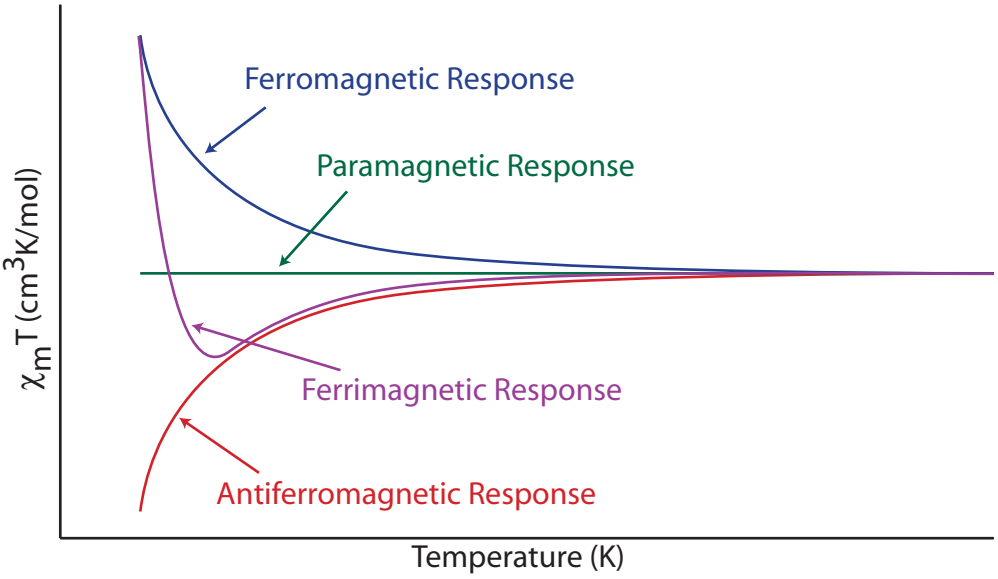

Figure 6.6: A typical plot for the susceptibility temperature product as a function of temperature is shown for paramagnetic, ferromagnetic, antiferromagnetic and ferrimagnetic materials.

Inverse Susceptibility vs. Temperature. An ideal paramagnet has a linear relationship between inverse susceptibility and temperature that intersects at zero as defined by the Curie law. Deviation from this linear relationship and the Curie law is observed for materials that exhibit cooperative magnetic effects. As seen in Figure 6.7, a ferromagnetic material exhibits an downward deviation, while an antiferromagnetic materials exhibits a upward deviations. In all cases the data at high temperature are linear, since thermal energy is greater than the energy of the magnetic interations.

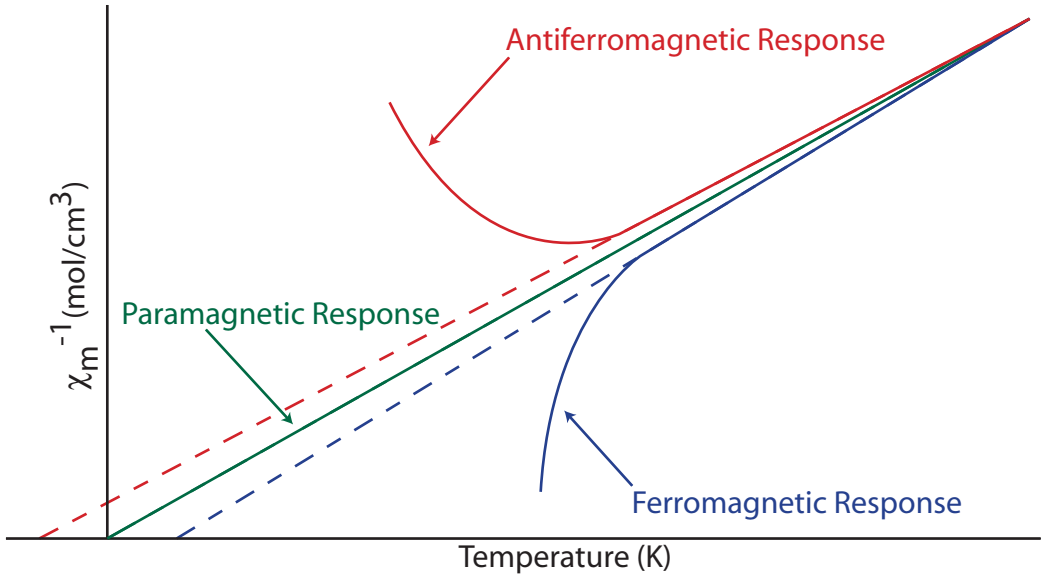

Figure 6.7: A pot of inverse susceptibility as a function of temperature is shown for a paramagnet, a ferromagnet, and an antiferromagent. The dotted lines indicate deviation of the high temperature data from the paramagnetic case.

A modification of the Curie law (1.3), known as the Curie-Weiss law (1.7), describes this deviation. The Weiss constant (Θ) is proportional to the strength of the magnetic interactions observed. Positive Weiss constants indicate ferromagnetic interactions, while negative Weiss constants indicate antiferromagnetic interactions. This framework

is useful for looking at the predominate interaction in the material and the strength of that interaction.

$$\chi_m = \frac{C}{T - \Theta} \qquad (6.7)$$

Hysteresis (Bertotti, 1998). One of the most distinctive features of materials with bulk magnetism is hysteresis. Hysteresis is observed for ferromagnetic and ferrimagnetic materials below their critical point and arises from rearrangement of domain walls within the material. The hysteresis of a sample is determined by looking at magnetization as a function of an applied magnetic field. A typical hysteresis curve for a bulk magnetic material is shown in Figure 6.8.

The hysteresis of a material is typically defined by two distinctive points; the remnant magnetization (M_r) and the coercive field (H_c). Remnant magnetization is obtained by applying and removing a large magnetic field and represents the extent to which a bulk magnetic material exhibits spontaneous magnetism. The coercive field of a sample is the magnetic field required to bring the magnetization of a sample to zero. Coercive fields from 0.01 G to 15,000 G have been observed for different materials. In general materials with low coercive fields (< 1 G) have been termed “soft” magnets, while materials with high coercive field (>500 G) have been termed “hard” magnets.

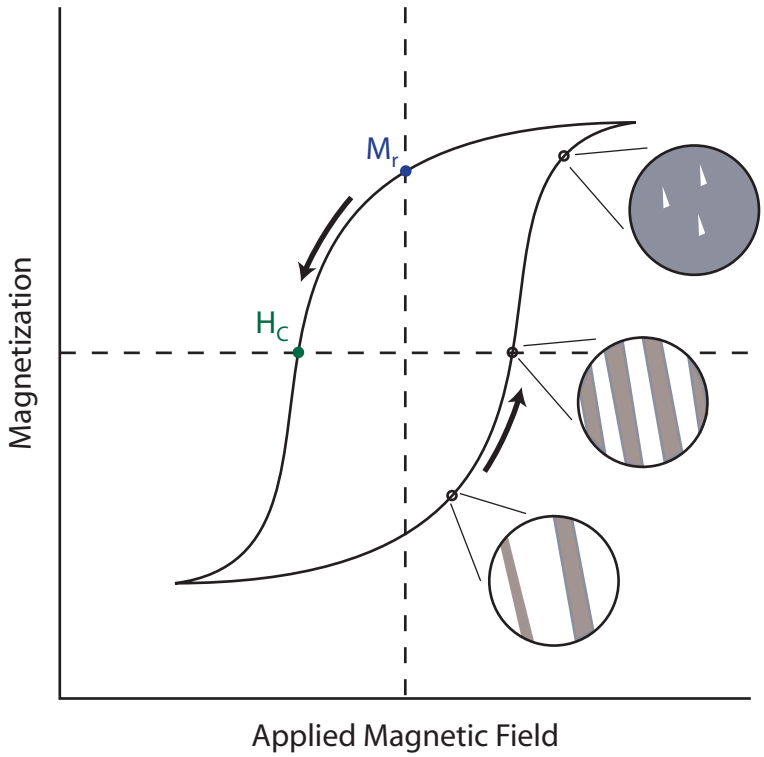

Figure 6.8: A typical hysteresis curve for a material with a bulk magnetic moment is shown. The domain structure for the material is indicated at several points along the curve, where the gray domains are aligned with each other and with the magnetic field and the white domains are aligned randomly.

6.2.4 Summary

In high-spin materials magnetic interactions are diverse and bulk magnetism is a complicated phenomenon. Materials composed of paramagnetic species exhibit a variety of responses to temperature and applied magnetic field. From these responses the interactions between adjacent magnetic spins can be determined and understood. Only a small number of the different types of magnetism and possible magnetic responses to either temperature or applied magnetic field have been explored here.

6.3 Design of Novel Magnetic Materials

The design of novel magnetic materials has focused on the development of ferromagnetic and ferrimagnetic materials, since these materials are useful for device design. Various antiferromagnetic materials have received limited attention over the years, principally as model systems for testing physical theories. In general, the design of novel magnetic materials can be broken into two broad classes, the design of organic ferromagnetic materials and the design of organic-inorganic hybrid ferromagnetic and ferrimagnetic materials.

Several different approaches have been applied in attempts to build both organic and organic-inorganic hybrid materials. These approaches include high-spin organic polymers, bimetallic ferrimagnets, and crystal packing. Application of each approach will be described in the remaining chapters and appendices of this section.

6.3.1 High-spin Organic Polymers

Our group has had a long-standing interest in understanding and applying the rules for ferromagnetic coupling of high-spin organic molecules (Anderson and Dougherty, 1998; Anderson et al., 1997; Dougherty, 1991; Jacobs et al., 1993; Kaisaki et al., 1991; Kearney et al., 1993; Murray et al., 1994; Silverman and Dougherty, 1993). Understanding these rules should allow for the creation of interesting magnetic organic materials. Figure 6.9 illustrates a useful model to generate a one-dimensional ferromagnet, where a ferromagnetic coupling unit enforces high-spin interactions between spin-containing units.

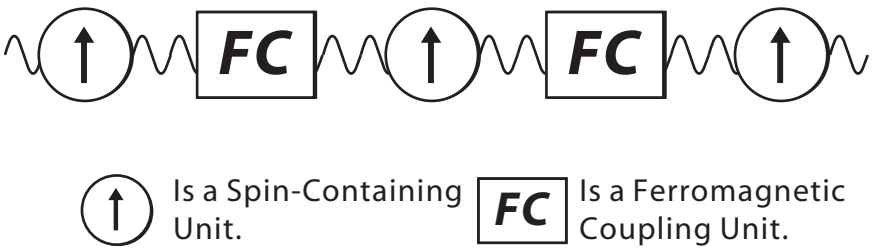

Figure 6.9: A schematic model for the design of high-spin organic molecules.

Ferromagnetic coupling units are structures that ferromagnetically couple any two spin containing units regardless of the structural details of the spin-containing unit. Potential ferromagnetic coupling units have been identified by considering organic radicals with triplet ground states and evaluated using triplet biradicals as spin containing units (Dougherty, 1991; Jacobs et al., 1993). Tetraradicals **1-4** represent four potential spin containing units, which were evaluated by Dougherty and co-workers. Of these spin containing units only *m*-phenylene (**1**) and 1,3-cyclobutane (**2**) were effective ferromagnetic coupling units.

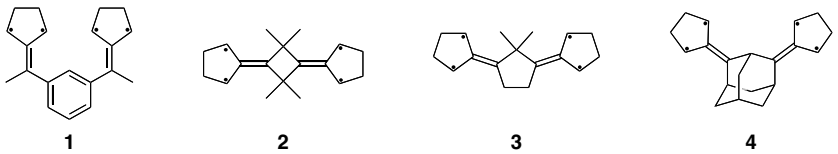

The smallest spin containing units for organic magnetic materials are charged or uncharged monoradicals. Although some monoradicals are stable, typically simple organic radicals are only stable at very low temperatures in solid matrices. Results from conducting polymers have shown that polarons, delocalized radical cations or radical anions, can be easily generated and are relatively stable at room temperature. A number

of prototypical one-dimensional polaronic ferromagnets were studied using oxidatively doped spin containing units to give poly radical cations (**8-11**) (Murray et al., 1994). The resulting materials did not exhibit unmistakable ferromagnetic interactions, however the results were encouraging.

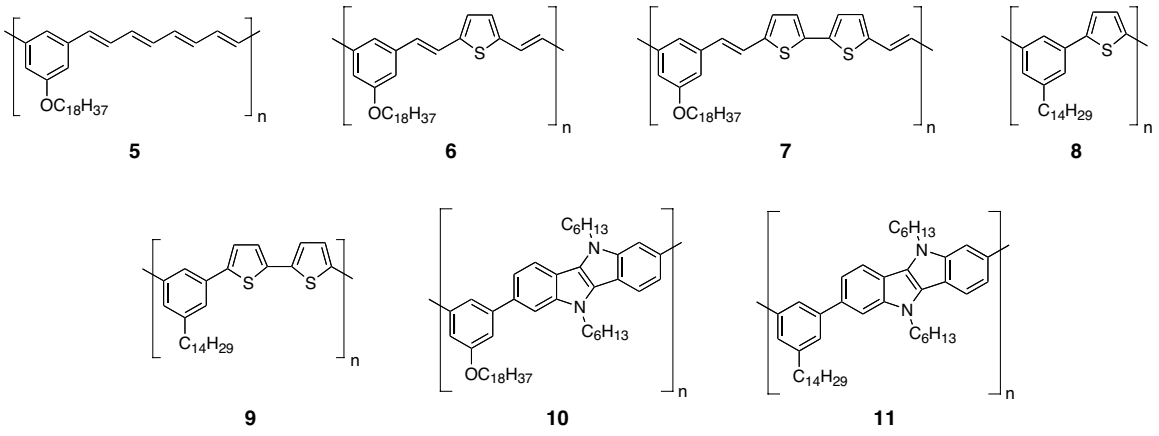

At low levels of doping, the materials displayed S values greater than one half. However at high levels of doping, these materials exhibited S values near one half, indicating no ferromagnetic interactions within the sample. Possible explanations for the lack of high-spin materials at high levels of doping include: intermolecular antiferromagnetic interactions, crosslinking, and bipolaron (spinless dication) formation from over oxidation.

To address these problems, a system based on the fuchone radical anion was designed (Anderson and Dougherty, 1998). This material, poly-*meta*-phenylenefuchsone (**12**), showed superior magnetic behavior to the oxidatively doped polymers. The material exhibited temperature dependant ferromagnetism with interactions beginning at about 40

K and an S value of 2 at a spin concentration of 60% of the theoretical maximum. Appendix II describes attempts to improve upon poly-meta-phenylenefuschone.

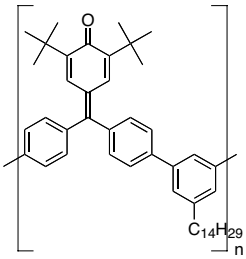

12

6.3.2 Bimetallic Ferrimagnets

A common approach to the development of molecular magnetic materials has been the creation of bimetallic ferrimagnetic materials. In these materials ridged alternation of metal atoms containing different spin states leads to a material with a bulk magnetic moment independent of how the spins are coupled. If adjacent magnetic spins couple antiferromagnetically than a ferrimagnet results, while if the spins couple ferromagnetically than a ferromagnet results. The popularity of this approach arises from the ability to develop high-spin materials without needing to control ferromagnetic coupling.

Classic examples of this strategy include Kahn's MnCu(pbaOH) ferromagnetic chains where pbaOH is 2-hydroxyl-1,3-propylenebis(oxamato) (Kahn et al., 1988; Pei et al., 1987), Caneschi and Gatteschi's metal-nitronyl nitroxide ferromagnetic chains (Caneschi et al., 1989a; Caneschi et al., 1989b; Caneschi et al., 1989c; Caneschi et al., 1988), and

Girolami's $Cs_2Mn[V(CN)_6]$ Prussian blue analog (Entley and Girolami, 1995). These materials all feature rigidly alternating magnetic spins of different magnitudes and all give rise to materials that exhibit bulk magnetic behavior. The ferrimagnetic critical temperature for $Cs_2Mn[V(CN)]_6$ is 230 K.

Attempts to design ferrimagnetic materials has created a host of interesting magnetic compounds. A series of novel bimetallic materials will be presented in Chapter 7.

6.3.3 Crystal Packing

A handful of stable crystalline organic radicals exhibit ferromagnetic behavior. Ferromagnetism in these materials arises from crystal packing. Galvinoxyl (**13**) shows ferromagnetic behavior between 300 K and 85 K, which arises due to parallel stacking between planar galvinoxyl radicals. Below 85 K galvinoxyl undegoes a phase transition, which results in antiferromagnetic behavior (Awaga et al., 1989; Awaga et al., 1987). Tanol radicals (**14**) exhibit two-dimensional ferromagnetism and order antiferromagnetically in the third dimension (Chouteau and Veyretjeandey, 1981). *p*-Nitrophenyl nitronyl nitroxide (**15**) is the first three dimensional organic ferromagnet and was discovered in 1991 (Tamura et al., 1991). This molecule orders ferromagnetically with a critical temperature of 0.60 K.

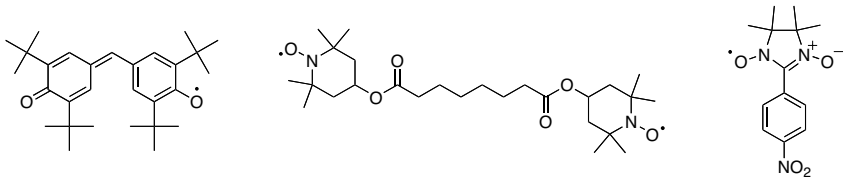

13 14 15

The ferromagnetic behavior observed for all these materials results from crystal packing. In these cases, the observed ferromagnetic behavior arose by chance. Strategies for designing ferromagnetic behavior into organic radicals have been proposed. The Cyclophane shown in Figure 6.10 represents one strategy that has been employed to design ferromagnetic packing (Izuoka et al., 1987). In this strategy two organic radicals are made to stack face-to-face, with regions of spin α on one molecule most closely positioned to regions of spin β on another, the antiferromagnetic interaction between those regions result in alignment of the spins on the two molecules.

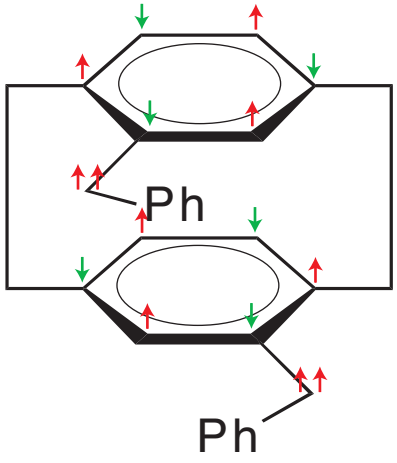

Figure 6.10: Spin interactions in a bis(diphenylcarbene)[2,2]paracyclophane system.

Previous work in our group has attempted to design ferromagnetic materials using the benzene-hexafluorobenzene crystal-engineering motif (Miller, 1998). Although interesting results were obtained using this motif, ferromagnetic packing was not achieved. Chapters 7 and Appendix III explore using the guanidinium sulfonate crystal engineering motif to design novel high-spin magnetic materials.

6.4 Crystal Engineering

Crystal engineering is the process of designing the three dimensional structure of solids, using non-covalent interactions. Most of the work in this area has focused on the design of organic materials. It is hoped that crystal engineering will produce materials with useful physical properties, such as non-linear optics, catalysis, and magnetism.

6.4.1 Macromolecular Synthons

In crystal engineering, as in conventional organic synthesis, conceptually a target structure can be broken down into smaller building blocks or synthons. The usefulness of a particular synthon depends on its generality. A large number of synthons for crystal engineering have been identified by searching small molecule structural databases and by rational design. Figure 6.11 shows 35 different molecular synthons that have been employed in crystal engineering (Desiraju, 1995).

One of the most robust synthons from Figure 6.11 is the carboxylic acid dimer. Of the small molecules examined by Desirajo, 85% of carboxylic acid groups dimerized (Desiraju, 1995). The robustness of a particular synthon for directing a molecule to

crystallize with a given pattern is a measure of its utility, in the same way that product yield is a measure of the utility of a particular sython in conventional organic synthesis.

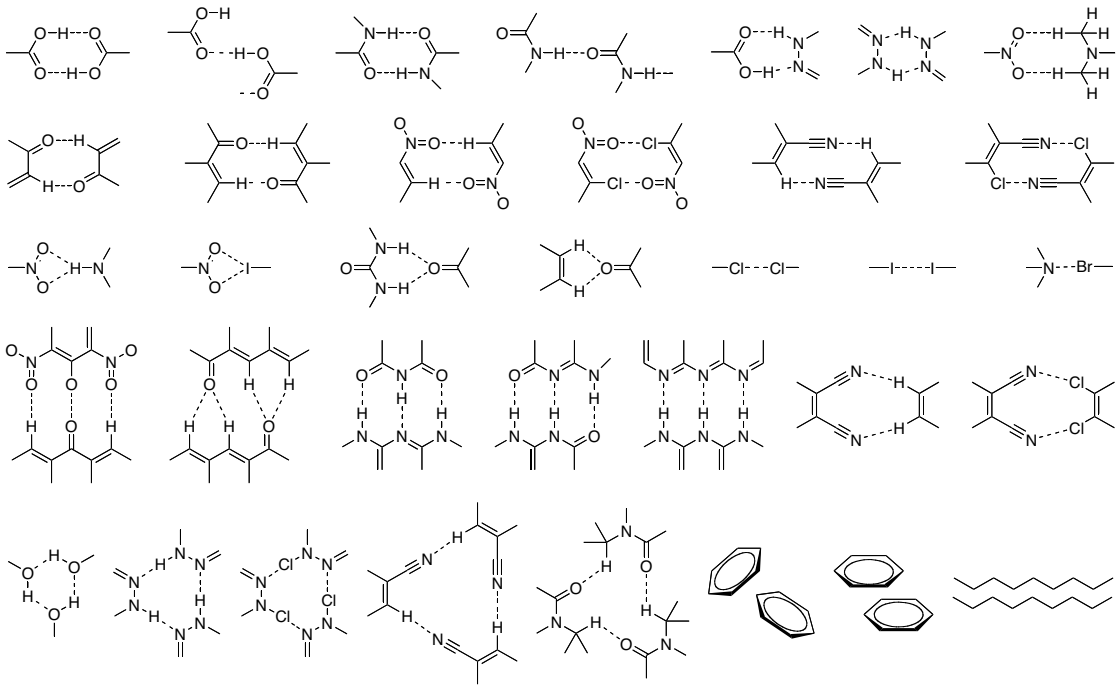

Figure 6.11: Molecular synthons that have been employed for crystal engineering.

6.4.2 Rules for Crystal Packing

In general the packing of small organic molecules is difficult to predict. The synthons described in section 6.4.1 provide one approach to controlling crystal packing, however these synthons only control packing in onedimension (Dunitz and Bernstein, 1995), while useful materials typically require a defined three-dimensional molecular structure. Three of the critical forces in three dimensional crystal packing are reviewed below.

Kitaigorodskii's principle of close packing (Kitaigorodskii, 1973). Small molecules tend to pack so as to minimize void volume in their three-dimensional structure. Typically, for an organic molecule the van der Waals radii of its component molecules encompass 60-77% of the total volume. This high density is a result of van der Waals forces accounting for most of the crystal packing enthalpy.

Satisfy hydrogen bond donors and acceptors (Kitaigorodskii, 1973). Hydrogen bonds tend to be a dominant force in crystal packing because they are highly directional and sensitive to small geometric perturbations. The need to satisfy hydrogen bond donors and acceptors can result in less dense packing of a molecular solid than of the same molecular liquid. This is observed when comparing ice with liquid water.

Minimize electrostatic energy (Kitaigorodskii, 1973). Weak electrostatic interactions, such as bond dipoles, can play important roles in crystal packing. Crystals pack so as to minimize the overall electrostatic energy of the three-dimensional crystal structure.

Using these principles and some of the molecular synthons shown in Figure 6.1 progress has been made towards being able to design three-dimensional molecular structure (Nangia and Desiraju, 1998; Sarma and Desiraju, 2002). However crystal engineering remains extremely difficult and very few motifs have been developed that provide three-dimensional molecular control. A three-dimensional crystal engineering motif based on guanidinium disulfonates (Russell et al., 1997). developed by Ward and co-worker, is

described in Chapter 7 and Appendix III along with its application for the development of novel molecular magnetic materials.

6.5 Literature Cited

Anderson, K. K., and Dougherty, D. A. (1998). An improved model for one-dimensional polaronic ferromagnetism: Electrochemically doped poly(m-phenylenefuchsone). Advanced Materials *10*, 688-692.

Anderson, K. K., Shultz, D. A., and Dougherty, D. A. (1997). Attempted synthesis of a stable, quintet, tetraphenoxyl tetraradical: Facile rearrangement of a substituted bicyclobutane. Journal of Organic Chemistry *62*, 7575-7584.

Awaga, K., Okamoto, H., Mitani, T., Maruyama, Y., Sugano, T., and Kinoshita, M. (1989). Spin-Soliton Excitation in One-Dimensional Alternating Antiferromagnetic System of Galvinoxyl Single-Crystal. Solid State Communications *71*, 1173-1177.

Awaga, K., Sugano, T., Kinoshita, M., Matsuo, T., and Suga, H. (1987). Thermodynamic Properties of the Mixed-Crystals of Galvinoxyl Radical and Its Precursory Closed Shell Compound - the Large Entropy Cooperating with the Spin System. Journal of Chemical Physics *87*, 3062-3068.

Bertotti, G. (1998). Hysteresis in magnetism. For physicists, material scientists, and engineers. (San Diego, Academic Press).

Caneschi, A., Gatteschi, D., Laugier, J., Rey, P., and Zanchini, C. (1989a). Synthesis, X-Ray Crystal-Structure, and Magnetic-Properties of 2 Dinuclear Manganese(Ii) Compounds Containing Nitronyl Nitroxides, Imino Nitroxides, and Their Reduced Derivatives. Inorganic Chemistry *28*, 1969-1975.

Caneschi, A., Gatteschi, D., Renard, J. P., Rey, P., and Sessoli, R. (1989b). Magnetic Phase-Transition and Low-Temperature Epr-Spectra of a One-Dimensional Ferrimagnet Formed by Manganese(Ii) and a Nitronyl Nitroxide. Inorganic Chemistry *28*, 1976-1980.

Caneschi, A., Gatteschi, D., Renard, J. P., Rey, P., and Sessoli, R. (1989c). Magnetic Phase-Transitions in Manganese(Ii) Pentafluorobenzoate Adducts with Nitronyl Nitroxides. Journal of the American Chemical Society *111*, 785-786.

Caneschi, A., Gatteschi, D., Sessoli, R., Hoffmann, S. K., Laugier, J., and Rey, P. (1988). Crystal and Molecular-Structure, Magnetic-Properties, and Electron-Paramagnetic-Res Spectra of a Trinuclear Copper(Ii) Complex with Bridging Nitronyl Nitroxides. Inorganic Chemistry *27*, 2390-2392.

Carlin, R. L. (1986). Magnetochemistry (Berlin, Springer-Verlag).

Chouteau, G., and Veyretjeandey, C. (1981). Metamagnetism in Tanol Suberate. Journal De Physique *42*, 1441-1444.

Desiraju, G. R. (1995). Supramolecular Synthons in Crystal Engineering - a New Organic- Synthesis. Angewandte Chemie-International Edition in English *34*, 2311-2327.

Dougherty, D. A. (1991). Spin Control in Organic-Molecules. Accounts of Chemical Research *24*, 88-94.

Dunitz, J. D., and Bernstein, J. (1995). Disappearing Polymorphs. Accounts of Chemical Research *28*, 193-200.

Entley, W. R., and Girolami, G. S. (1995). High-Temperature Molecular Magnets Based on Cyanovanadate Building-Blocks - Spontaneous Magnetization at 230-K. Science *268*, 397-400.

Hurd, C. M. (1982). Varieties of Magnetic Order in Solids. Contemporary Physics *23*, 469-493.

Izuoka, A., Murata, S., Sugawara, T., and Iwamura, H. (1987). Molecular Design and Model Experiments of Ferromagnetic Intermolecular Interaction in the Assembly of High-Spin Organic-Molecules - Generation and Characterization of the Spin States of Isomeric Bis(Phenylmethylenyl) 2.2 Paracyclophanes. Journal of the American Chemical Society *109*, 2631-2639.

Jacobs, S. J., Shultz, D. A., Jain, R., Novak, J., and Dougherty, D. A. (1993). Evaluation of Potential Ferromagnetic Coupling Units - the Bis(Tmm) Approach to High-Spin Organic-Molecules. Journal of the American Chemical Society *115*, 1744-1753.

Kahn, O. (1993). Molecular Magnetism (New York, VCH Publishers, Inc.).

Kahn, O., Pei, Y., Verdaguer, M., Renard, J. P., and Sletten, J. (1988). Magnetic-Ordering of Mniicuii Bimetallic Chains - Design of a Molecular-Based Ferromagnet. Journal of the American Chemical Society *110*, 782-789.

Kaisaki, D. A., Chang, W. H., and Dougherty, D. A. (1991). Novel Magnetic-Properties of a Doped Organic Polymer - a Possible Prototype for a Polaronic Ferromagnet. Journal of the American Chemical Society *113*, 2764-2766.

Kearney, P. C., Mizoue, L. S., Kumpf, R. A., Forman, J. E., McCurdy, A., and Dougherty, D. A. (1993). Molecular Recognition in Aqueous-Media - New Binding-Studies Provide Further Insights into the Cation-Pi Interaction and Related Phenomena. Journal of the American Chemical Society *115*, 9907-9919.

Kitaigorodskii, A. I. (1973). Molecular Crystal and Molecules (New York, Academic Press).

Manson, J. L., Ressouche, E., and Miller, J. S. (2000). Spin frustration in M(II) [C(CN)3]2 (M=V, Cr). A magnetism and neutron diffraction study. Inorg Chem *39*, 1135-1141.

Mattis, D. C. (1981). The theory of magnetism, Vol I (Berlin, Springer-Verlag).

Miller, J. S., and Epstein, A. J. (1994). Organic and Organometallic Molecular Magnetic-Materials - Designer Magnets. Angewandte Chemie-International Edition in English *33*, 385-415.

Miller, S. A. (1998) Magnetic Interactions in Molecular Materials, Doctoral, California Institute of Technology, Pasadena.

Murray, M. M., Kaszynski, P., Kaisaki, D. A., Chang, W. H., and Dougherty, D. A. (1994). Prototypes for the Polaronic Ferromagnet - Synthesis and Characterization of High-Spin Organic Polymers. Journal of the American Chemical Society *116*, 8152-8161.

Nangia, A., and Desiraju, G. R. (1998). Supramolecular synthons and pattern recognition. In Design of Organic Solids, pp. 57-95.

Pei, Y., Verdaguer, M., Kahn, O., Sletten, J., and Renard, J. P. (1987). Magnetism of Mniicuii and Niiicuii Ordered Bimetallic Chains - Crystal-Structure of Mncu(Pba)(H2o)3.2h2o (Pba = 1,3- Propylenebis(Oxamato)). Inorganic Chemistry *26*, 138-143.

Russell, V. A., Evans, C. C., Li, W. J., and Ward, M. D. (1997). Nanoporous molecular sandwiches: Pillared two-dimensional hydrogen-bonded networks with adjustable porosity. Science *276*, 575-579.

Sarma, J., and Desiraju, G. R. (2002). The supramolecular synthon approach to crystal structure prediction. Crystal Growth & Design *2*, 93-100.

Silverman, S. K., and Dougherty, D. A. (1993). Conformational Effects on High-Spin Organic-Molecules. Journal of Physical Chemistry *97*, 13273-13283.

Tamura, M., Nakazawa, Y., Shiomi, D., Nozawa, K., Hosokoshi, Y., Ishikawa, M., Takahashi, M., and Kinoshita, M. (1991). Bulk Ferromagnetism in the Beta-Phase Crystal of the Para- Nitrophenyl Nitronyl Nitroxide Radical. Chemical Physics Letters *186*, 401-404.

Toulouse, G. (1977). Physics *2*, 115.

Turnbull, M. M., Sugimoto, T., and Thompson, L. K., eds. (1996). Molecule-Based Magnetic Materials. Theory, Techniques, and Applications. (Washington, DC, American Chemical Society).

Villain, J. (1977). Jounral of Physics C *10*, 1717.

Chapter 7: Use of Crystal Engineering to Design a Novel Family of Frustrated Magnetic Materials based on Guanidinium 5,5'-Salen Disulfonate

7.1 Introduction

Molecular magnetic materials are a potential source of novel interesting magnetic materials, but the design of these materials has proven to be extremely difficult (Kahn, 1993; Miller and Epstein, 1994; Turnbull et al., 1996). One potential solution to the difficulties associated with designing magnetic materials is the use of organic crystal engineering. Organic crystal engineering provides a method with well-defined structural rules that can be used to template magnetic materials. Despite the identification of many organic crystal engineering motifs (Aakeroy, 1997; Desiraju, 1988), these motifs have not been applied successfully to the development of molecular magnetic materials.

7.1.1 The "Ward Lattice"

The guanidinium sulfonate motif developed by Ward and co-workers is one of the most resilient organic crystal engineering motifs (Evans et al., 1999; Russell et al., 1994a; Russell et al., 1994b; Russell et al., 1997; Russell and Ward, 1996; Russell and Ward, 1997; Russell and Ward, 1998; Swift et al., 1998a; Swift et al., 1998b; Swift et al., 1997; Swift and Ward, 2000). Generally, this motif consists of a triangular array of hydrogen bonded guanidinium cations and sulfonate anions (Figure 7.1A). It has also been shown that incorporation of disulfonates into this motif gives one of two three-dimensional structures: a pillared bilayer motif or a pillared brick motif. Each motif contains large cavities, and the motif obtained depends on the guest molecules around which the structure is templated (Russell et al., 1997; Swift et al., 1998a). The different motifs are illustrated in Figure 7.1B.

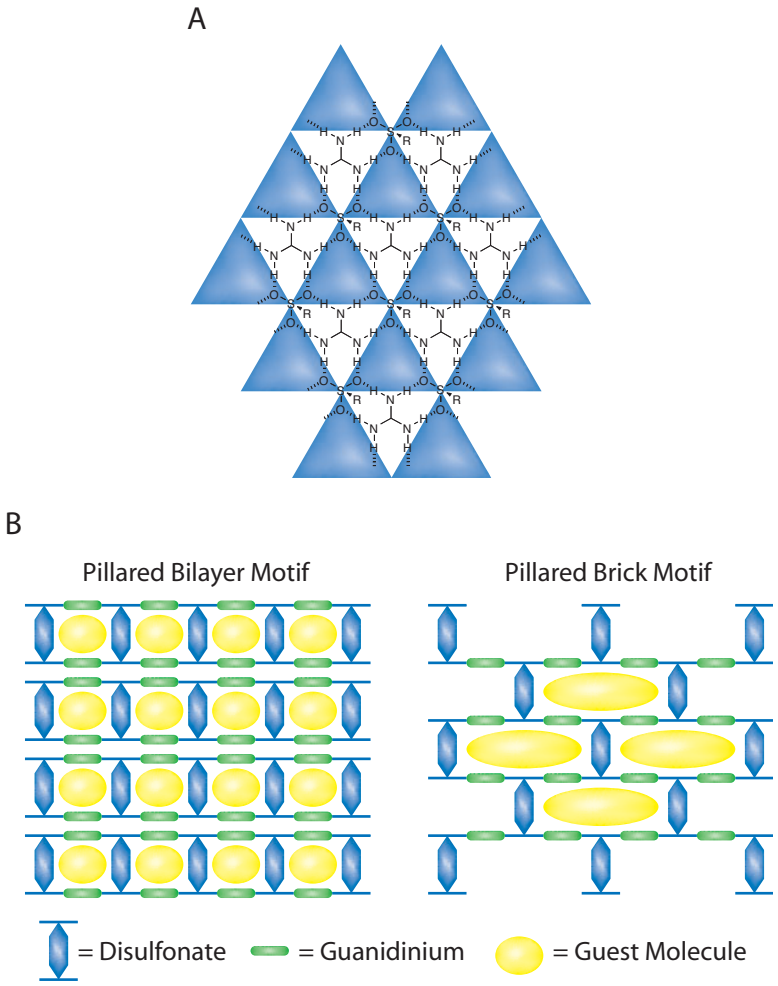

Figure 7.1: A) Schematic representation of the sheet-like hydrogen bonded networks formed from guanidinium cations and sulfonate anions. B) Schematic representation of layered materials synthesized from guanidinium cations and disulfonates, as viewed along the long axis of the hydrogen bonded ribbons contained in the nominal planar guanidinium sulfonate networks.

7.1.2 Design Strategy

Our strategy for preparing novel molecular magnetic materials was based on the pioneering work of Kahn. Mixed systems of alternating Cu(II) and Mn(II) have produced ferromagnetic and ferrimagnetic materials with relatively high critical temperatures, around 20 K (Kahn et al., 1988; Pei et al., 1987; Stumpf et al., 1993a; Stumpf et al., 1993b). When using first row transition metals to prepare mixed metal systems Cu(II)

and Mn(II) typically produce the best results, since antiferromagnetic coupling between adjacent metal ions is common and upon antiferromagnetic coupling a copper-manganese pair has the largest residual spin value (S=2). We reasoned that the "Ward lattice" might provide a means to specifically position rigidly alternating Cu(II) and Mn(II) ions, by binding one of the metal ions to the disulfonate pillar and incorporating the second metal ion into the structure as guest molecule.

The chemistry and magnetic properties of metal Schiff base complexes have been extensively studied (Holm et al., 1966). Additionally, copper salen complexes are well known and their magnetic behaviors are fully documented (O'Brian, 1984). One would expect a copper salen complex with appropriate sulfonic acid substituents could fit into a "Ward lattice," and leave open coordination sites. Using these open coordination sites bridging ligands could then be used to interact a second high spin metal with the first metal. This metal coordination strategy should give rise to ferromagnetic or ferrimagnetic linear chains (Figure 7.2).

In addition to the ability to orient bimetallic materials, the triangular nature of the "Ward lattice" suggested that it might be possible to engineer frustrated magnetic systems using this motif. Magnetic frustration has received a great deal of attention since its introduction in the late 1970's (Toulouse, 1977; Villain, 1977). Spin frustration arises in systems where competing interactions lead to a degenerate ground state (Kahn, 1993). Extensive work has led to the development of many theoretical and computational models to describe long-range spin frustration on extended lattices (Becca and Mila,

2002; Garcia-Adeva and Huber, 2002; Kruger and Richter, 2001; Siurakshina et al., 2001; Tsunetsugu, 2001; Zukovic et al., 2002), such as would be observed for a Kagomé lattice or a pyrochlore lattice. Despite theoretical interest in magnetic frustration, very few experimental examples of frustrated magnetic systems exits. However it is known that orientation of magnetic moments on a triangular lattice leads to spin frustration (Coey, 1987; Manson et al., 2000).

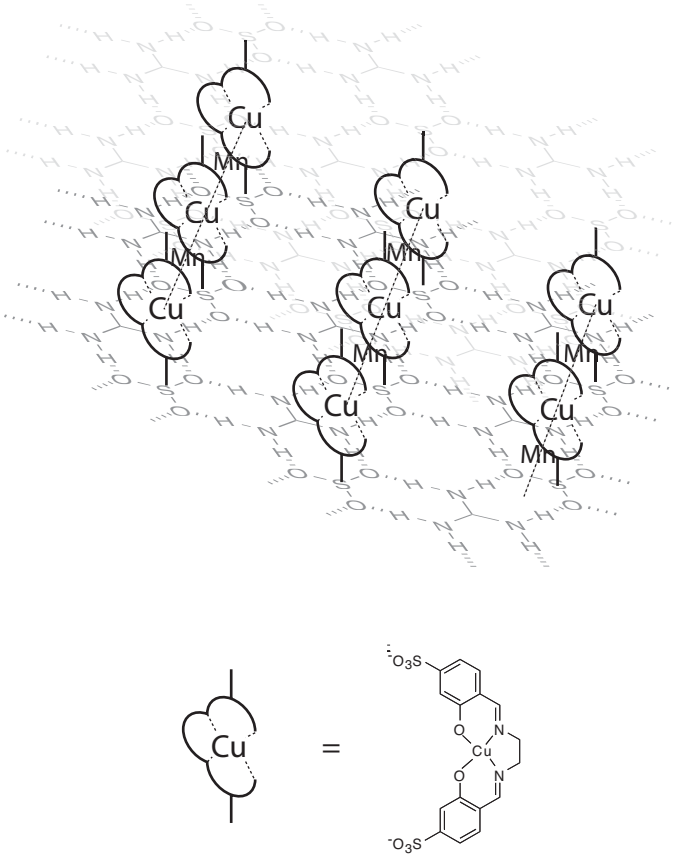

Figure 7.2: Schematic representation of copper-manganese ferromagnetic or ferrimagnetic linear chains in a guanidinium sulfonated crystal lattice.

Here we report a series of magnetically interesting complexes designed using the "Ward lattice." The majority of compounds are a novel family of magnetically frustrated

bimetallic solids designed using the guanidinium sulfonate crystal engineering motif with a 5,5'-salen disulfonic acid pillar. This pillar is capable of binding and positioning a metal ion within the triangular lattice of the guanidinium sulfonate motif. Although a number of different bimetal compounds were prepared, we focus here on dc magnetic analysis of the copper-manganese complex.

7.2 Results and Disscussion

7.2.1 Guanidium N-phenylsalicylidene sulfonate Complexes

The guanidinium complex of copper (II) bis(N-phenylsalicylidene sulfonate) (**1**) was prepared by mixing guanidinium acetate, copper acetate, and N-phenylsalicylidene sulfonic acid. The resulting complex was confirmed by elemental analysis and magnetically characterized. Figure 7.3 shows the susceptibility temperature product as a function of temperature for the complex.

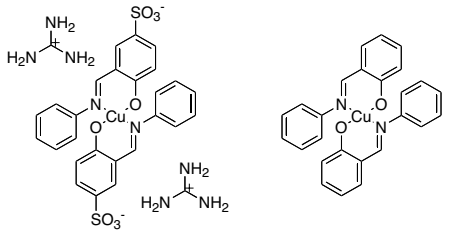

The magnetic data for compound **1** show a weak ferromagnetic interaction at very low temperature, as indicated by the slight up turn in the data. The strength of the interaction suggests that it is most likely a result of intramolecular ferromagnetic coupling.

Although long-range ferromagnetic interactions are not unprecedented, typically long range interactions in molecular solids are antiferromagnetic.

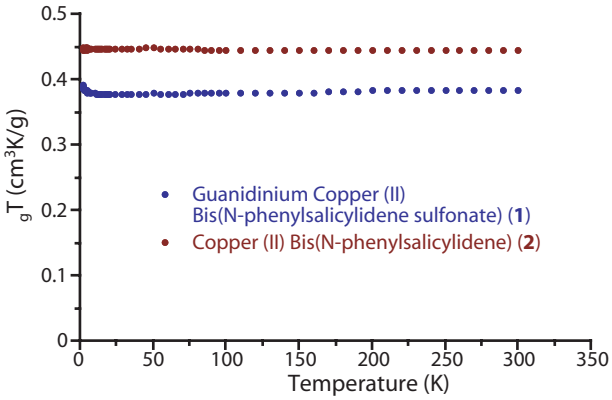

Figure 7.3: Variable temperature magnetic data for compounds **1** and **2**.

To verify if the intermolecular interaction was a result of crystal packing imposed on the structure by the "Ward lattice," copper (II) Bis(N-phenylsalicylidine) (**2**) was synthesized from copper acetate and N-phenylsalicylidene. The variable temperature magnetic data for **2** are also shown if Figure 7.3 . Compound **2** does not exhibit the ferromagnetic upturn at low temperature seen for compound **1**, suggesting that the ferromagnetic behavior observed for compound **1** is imposed as a result of the "Ward lattice."

Compound **1** was recrystallized from water to give small yellow crystals. A crystal structure of these crystals was obtained and stereoviews of the structure along the three principle crystallographic axes are show in Figure 7.4. Unfortunately the crystals obtained upon recrystallization lacked copper and the structure is therefore of

guanidinium N-phenylsalicylidene sulfonate. However, the crystal structure is an example of a "Ward lattice". The details of the crystal structure are given in Appendix II.

7.2.2 Guanidinum 5,5'-Salendisulfonic Acid Bimetallic Materials

7.2.2.1 The Copper-Manganese Complex

5,5'-Salendisulfonic acid (dss), manganese (II) acetate, copper (II) acetate, and guanidinium (gd) acetate were mixed to produce a solid to which we assign the molecular composition: $Mn_3[Cu(dss)]_3(gd)_4(OAc)_4$, based on quantitative and qualitative analysis. The molecular composition was determined from the copper-manganese, copper-sulfur, manganese-sulfur, sulfur-nitrogen, and carbon-nitrogen ratios. The copper to manganese ratio is 1.2:1.0. From the manganese-sulfur and the copper-sulfur ratios, disulfonate to metal ratios of 0.9:1.0 and 1.1:1.0 are obtained, respectively. The guanidinium to disulfonate ratio is 1.4:1.0, as determined from the nitrogen to sulfur ratio. Using these ratios the molecular formula of the complex was determined. Furthermore, the analytical data indicate that the purity of the desired material is approximately 90%. The magnetic and analytical data suggest that the observed impurity is an antiferromagnetic copper complex, given the excess of copper to manganese. The relative amount of this impurity is dependent on the reaction stoichiometry.

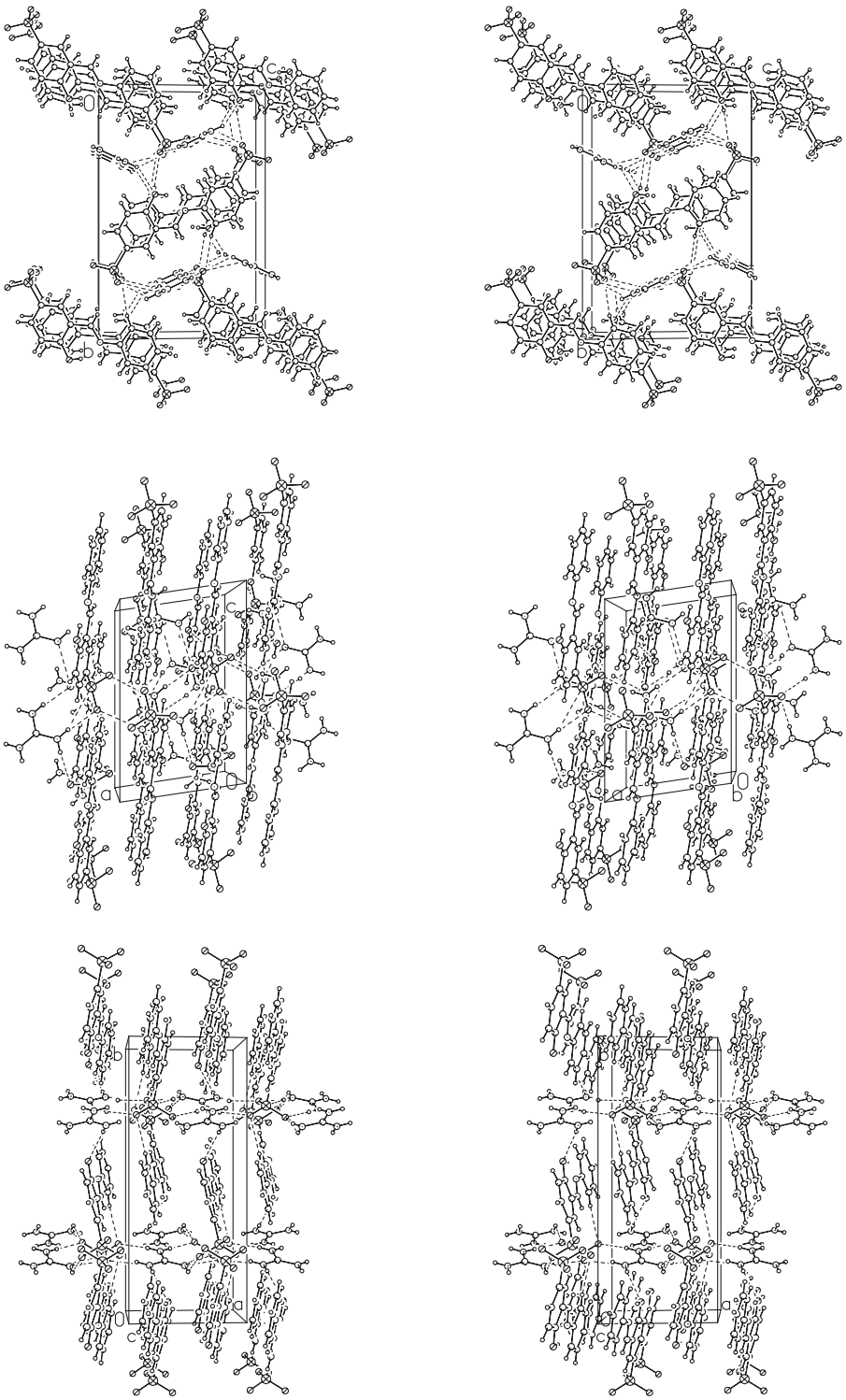

Figure 7.4: Stereo views of the guanidinium N-phenylsalicylidene sulfonate crystal structure as viewed along each of the principle crystallographic axes.

Using the optimal reaction stoichiometry described in the Methods section, we can reproducibly prepare large quantities of the copper-manganese complex whose materials we will now describe. All efforts at crystallization or further purification failed. As such, we feel there is value in reporting the intriguing magnetic behaviors of this material and several derivatives at this time, in the hope that it will spur further work.

Qualitative analysis of the copper-manganese complex indicated that the copper is bound to the salen ligand. Free copper in solution can be detected by the formation of a precipitate upon addition of either potassium iodide or potassium thiocyanate (Svehla, 1996). Addition of potassium iodide or potassium thiocyanate to the copper-manganese complex did not result in precipitation, indicating that the copper is tightly bound by the salen ligand.

On the face of it, the magnetic behavior of the copper-manganese complex appears to be ferromagnetic with a critical temperature of 42.4 K. Figure 7.5 shows field-cooled, zero-field-cooled, and remnant magnetization measurements collected with a 1 gauss magnetic field. The data suggest that the material orders ferromagnetically with a relatively high ordering temperature for a molecular magnetic material. Although in a small number of cases high temperature ferromagnetic ordering has been achieved, most molecular magnetic materials order ferromagnetically only below 10 K (Kahn, 1993; Turnbull et al., 1996).

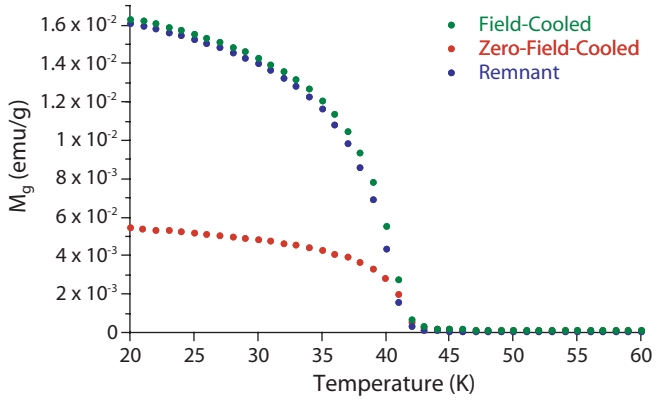

Figure 7.5: Field-cooled, zero-field-cooled, and remnant magnetization as a function of temperature for the copper-manganese complex.

The data of Figure 7.5 for the copper-manganese complex are as expected for a ferromagnetic material. In all cases the data show an abrupt transition around 42 K. Fitting the remnant magnetization near the critical temperature to a power law gives a critical temperature (T_c) of 42.4 K and a critical exponent (□) of 1.48. As expected for a ferromagnet, the zero-field-cooled magnetization is always lower than the field-cooled magnetization, since in this temperature range the applied magnetic field is too weak to move the domain walls.

In addition to exhibiting ferromagnetic field-cooled, zero-field-cooled, and remnant magnetic behavior, the copper-manganese complex also exhibits significant hysteresis, Figure 7.6. The copper manganese complex is a "hard" magnetic material and exhibits coercive fields of up to 2,500 G coupled with large remnant magnetizations. The magnitude of the observed values for coercive field and remnant magnetization are not atypical for molecular magnetic materials.

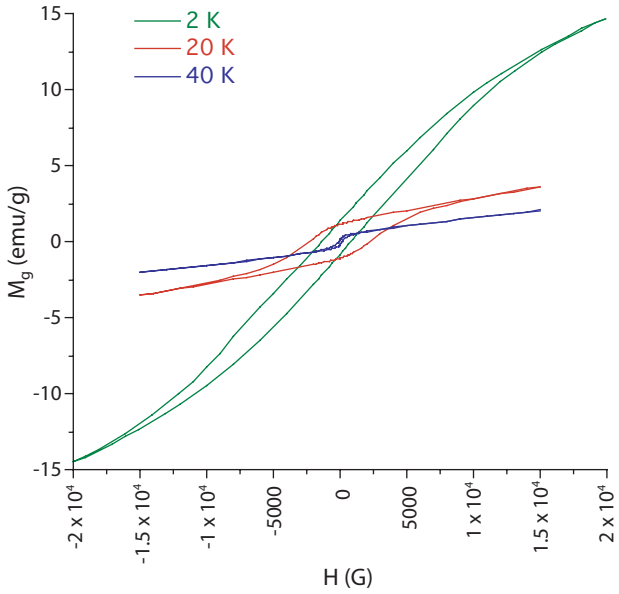

Figure 7.6: Hysteresis loops for the copper-manganese complex at 2 K, 20 K and 40 K.

The hysteresis data for the copper-manganese complex, however, exhibit unusual temperature dependence. The coercive field and remnant magnetization vary greatly with temperature (Figure 7.7). These changes are accompanied by changes in the shape of the hysteresis curve as can be seen in Figure 7.6. These findings indicated that a simple ferromagnetic model is not sufficient to describe the magnetic behavior of the copper-manganese complex.

Preliminary analysis of the temperature-dependent susceptibility data for the copper-manganese complex was in agreement with the previous suggestion of ferromagnetic behavior with a critical temperature around 42 K. The plot of the susceptibility temperature product, Figure 7.8, indicates a ferromagnetic ordering at around 42 K, followed by long range antiferromagnetic ordering at low temperature.

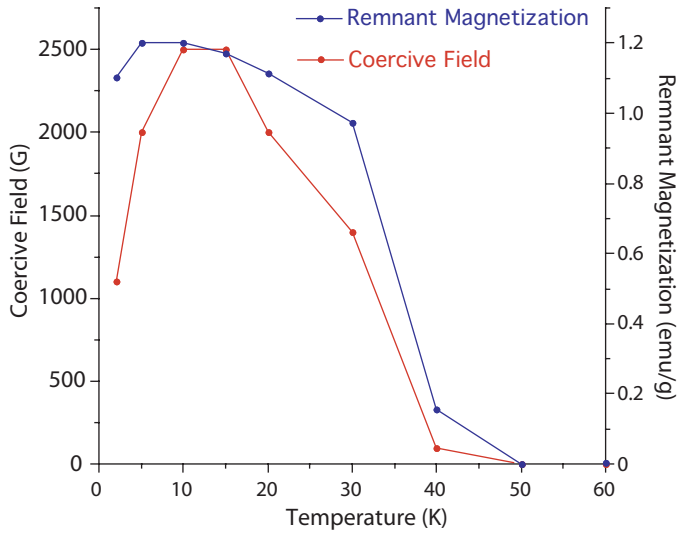

Figure 7.7: The temperature dependence of the coercive field and remnant magnetization of the copper-manganese complex is shown.

However, further analysis of the copper-manganese complex revealed that its susceptibility shows unusual field dependence (Figure 7.9). The copper-manganese complex exhibits increasing magnetic susceptibility as a function of decreasing magnetic field. This behavior is the exact opposite of the behavior typically observed for ferromagnetic materials. Close examination of the magnetic data suggest that magnetic responses observed for the copper-manganese complex are those of a frustrated magnetic material.

Magnetic frustration is not an experimentally well-characterized phenomenon and many different magnetic behaviors have been associated with frustration. As such, a comparison of the copper-manganese complex with several previously characterized frustrated materials has been used to assign frustration to this complex. In all cases the

behavior exhibited by the copper-manganese complex is slightly different than the previously characterized complexes, however it should also be noted that the behavior of these frustrated compounds is not self consistent. The compounds used here for comparison are $[NH_2(CH_2)_3NH_2](VO)_3(H_2O)_2(PO_4)_2$ (Soghomonian et al., 1993), $SrCr_9Ga_3O_{19}$ (Ramirez et al.,, 1990), $CsNiFeF_6$ (Alba et al., 1982), $LiNiO_2$ (Hirakawa et al., 1985; Yamaura et al., 1996), all of which are accepted to be frustrated magnetic systems.

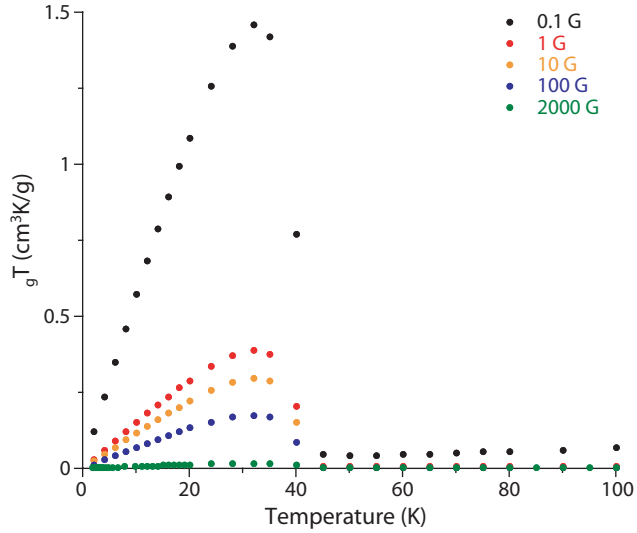

Figure 7.8: The susceptibility temperature product as a function of temperature for the copper-manganese complex measured at five different applied magnetic fields.

Similar field dependence of magnetic susceptibility has been observed for $[NH_2(CH_2)_3NH_2](VO)_3(H_2O)_2(PO_4)_2$ (Soghomonian et al., 1993). However, this material exhibits ferromagnetic behavior at low applied magnetic fields (10 G), antiferromagnetic behavior at moderate applied magnetic fields (500 G), and paramagnetic behavior at high

applied magnetic fields (2000 G), whereas the copper-manganese complex exhibits only ferromagnetic behavior with applied magnetic fields up to 2000 G (Figure 2b). $[NH_2(CH_2)_3NH_2](VO)_3(H_2O)_2(PO_4)_2$ exhibits pronounced local antiferromagnetic behavior at 50 K, which is not observed for our material, and only shows field dependant magnetization at 5.2 K. Additionally, $[NH_2(CH_2)_3NH_2](VO)_3(H_2O)_2(PO_4)_2$ has a Weiss constant of +20 K as opposed to the negative Weiss constant displayed by the copper-manganese material (Figure 7.10). Nevertheless, the inverse relationship between applied magnetic field and magnetic susceptibility has been termed a hallmark of magnetic frustration (Soghomonian et al., 1993) and serves as our first line of evidence that the copper-manganese complex is a frustrated magnetic material.

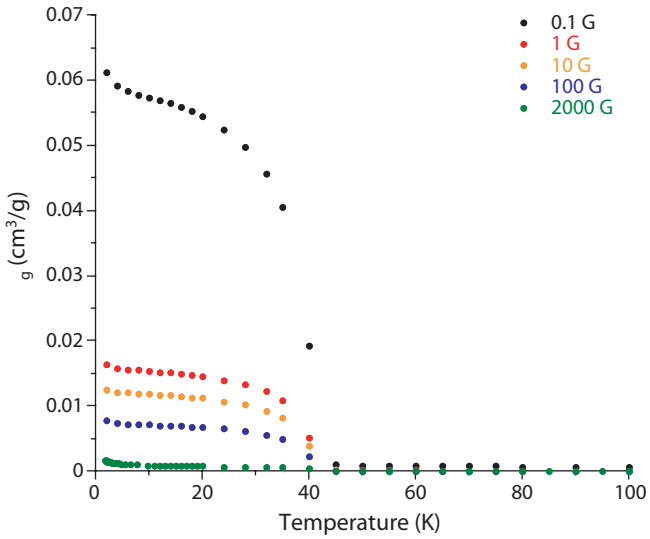

Figure 7.9: Susceptibility as a function of temperature for the copper-manganese complex. Increased susceptibility is observed as the applied magnetic field decreases.

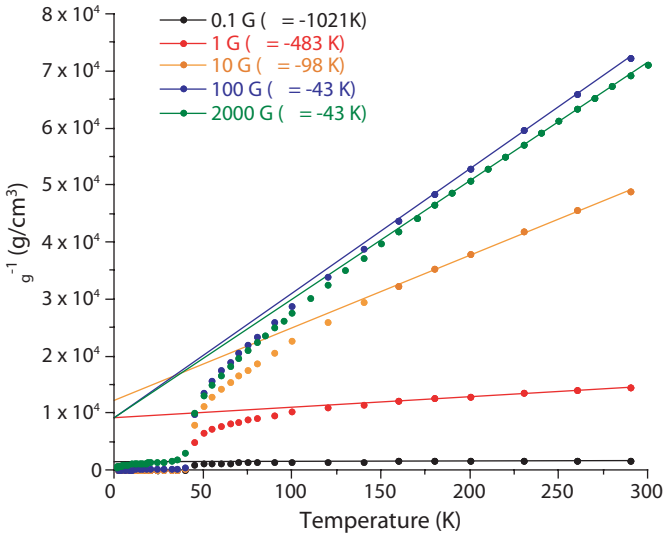

Figure 7.10: Inverse susceptibility as a function of temperature for the copper-manganese complex. The observed Curie-Wiess constant decreases as a function of increasing applied magnetic field.

The main evidence for a frustrated state comes from the disparity between the expected ordering temperature as predicted by the Curie-Weiss law, θ_{cw}, and the observed ordering temperature. The degree of frustration exhibited by a magnetic material has previously been characterized by the ratio of Weiss constant to the observed critical temperature. In this analysis if the ratio of θ_{cw} to T_c, is greater than one the material exhibits some degree of magnetic frustration. $SrCr_9Ga_3O_{19}$ and $CsNiFeF_6$ are thought of as strongly frustrated materials, and they exhibit θ_{cw} to T_c ratios of 150 and 45 respectively (Alba et al., 1982; Ramirez et al., 1990). Since the copper-manganese complex shows a ferromagnetic anomaly, as opposed to the antiferromagnetic anomalies observed for $SrCr_9Ga_3O_{19}$ and $CsNiFeF_6$, it is difficult to compare our θ_{cw} to T_c ratio to those previously observed. However, if we consider the absolute value of the ratio of θ_{cw}

to T_c, the value observed at 0.1 G, $\theta_{CW}/T_c = 24$, is substantial compared to $LiNiO_2$ where, $\theta_{CW}/T_c = 3$.

The magnitude of the ratio of θ_{CW} to T_c is a lower estimate for the copper-manganese system, since examination of the inverse dc susceptibility of the copper-manganese complex as a function of field shows magnetic interaction at high temperatures. Fitting the magnetic data above 150 K to the Curie law gives an observed θ_{CW} value for the complex that varies from –43 K at 2000 G to –1021 K at 0.1 G. Based on the observed trend in Figure 7.10, it seems likely that if the applied magnetic field were further decreased larger Weiss constants would be observed. Larger Weiss constants would give rise to a larger ratio of θ_{CW} to T_c.

All of the known frustrated magnetic materials examined here thus far have exhibited only antiferromagnetic ordering phenomena at some applied magnetic field, however the copper-manganese complex always exhibits a ferromagnetic ordering phenomenon. In the case of $LiNiO_2$ anomalous ferromagnetic ordering has been assigned to magnetic frustration (Hirakawa et al., 1985; Yamaura et al., 1996). However, in this case both the observed ordering and θ_{CW} suggest ferromagnetic behavior with T_c for the complex being 5 K and θ_{CW} being +29.5 K. Like the copper-manganese complex and $[NH_2(CH_2)_3NH_2](VO)_3(H_2O)_2(PO_4)_2$, $LiNiO_2$ exhibits inverse field dependence. Although the magnetic frustration observed for $LiNiO_2$ is not identical to the frustration observed in the copper-manganese complex, it does provide precedent for anomalous ferromagnetic ordering in frustrated magnetic materials.

The observed magnetic behavior for the copper-manganese complex clearly suggests magnetic frustration resulting in an anomalous ferromagnetic ordering. The evidence for magnetic frustration is not only the disparity between the predicted and observed ordering temperatures, but also the disparity in the predicted nature of magnetic ordering. The disparity in the predicted nature of magnetic ordering may imply that this material exhibits massive frustration relative to previously reported frustrated magnetic systems.

The observation of magnetic frustration for the copper-manganese complex is not consistent with the expected magnetic behavior for the system shown in Figure 7.2. Additionally, the molecular formula that has been assigned to the copper-manganese complex lacks sufficient guanidinium to form a bridging "Ward lattice". To form a proper "Ward lattice", two equivalents of guanidinum are required for each equivalent of disulfonate, while the copper-manganese complex only contains 1 and 1/3 equivalents of guanidinum per equivalent of 5,5'-salendisulfonic acid. As a result is seems likely that the structure of the copper-manganese complex is modified from that of a standard "Ward lattice".

One possible structure for copper-manganese complex, which would explain the magnetic data, is the modified "Ward lattice" shown in Figure 7.11. The proposed lattice maintains the same hydrogen-bonding pattern observed in a standard "Ward lattice", however it contains manganese atoms in addition to guanidinium and disulfonate. In this structure the manganese atoms lie on a bridged triangular lattice that could give rise to

the observed magnetic frustration. The salen bond copper atoms would not contribute significantly to the variable temperature magnetism as is observed for compound **2**.

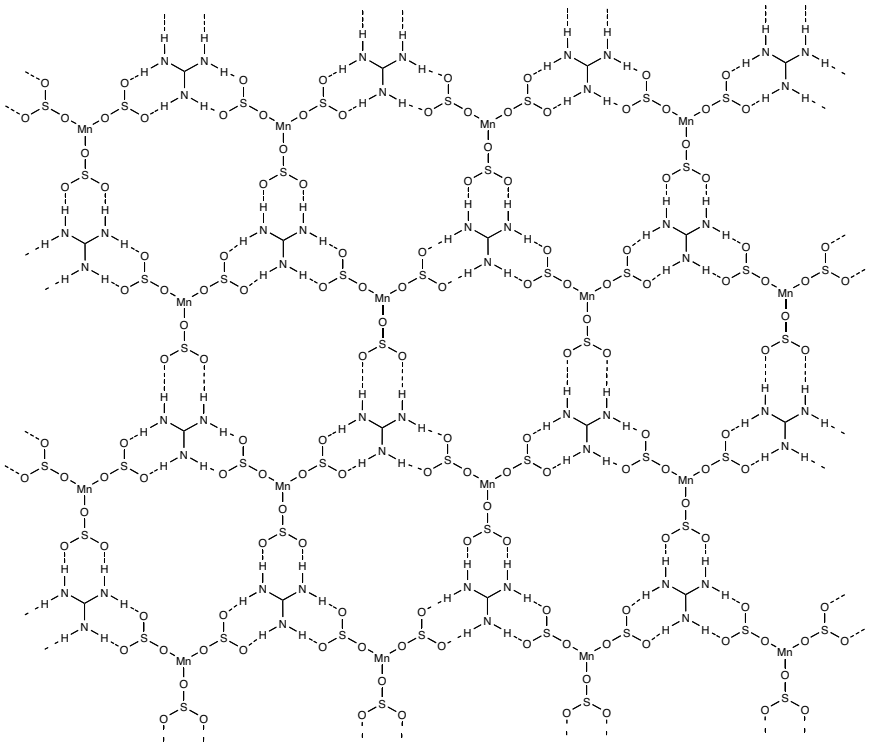

Figure 7.11: A modified "Ward lattice" that would explain the observed magnetic data for the copper manganese complex.

7.2.2.2 Other Bimetallic Complexes

Having observed anomalous ferromagnetic ordering for the copper-manganese system, the generality of using the pillared guanidinium 5,5'-salen disulfonate lattice for the generation of frustrated magnetic materials with anomalous magnetic ordering was examined. Bimetallic complexes containing manganese-iron, cobalt-copper, cobalt-iron, iron-copper, nickel-copper, nickel-manganese, nickel-iron, nickel-cobalt, and manganese-zinc were prepared using the method described for the copper-manganese complex. Anomalous ferromagnetic ordering was observed for the cobalt-copper, nickel-copper,

nickel-manganese, nickel-iron, and nickel-cobalt complexes (Figure 7.12), while the remaining complexes exhibited antiferromagnetic ordering at low temperature.

Despite exhibiting apparent ferromagnetic ordering, the bimetallic complexes all have negative Weiss constants and thus should exhibit antiferromagnetic ordering. At 100 G all materials except the nickel-iron complex exhibit relatively small Weiss constants with values ranging from -0.6 K to –17 K, however even the copper-manganese complex exhibits a relatively small Weiss constant, -43 K, at 100 G. One would expect, based on the behavior of the copper-manganese complex, that larger Weiss constants will be observed for these complexes at low magnetic fields. The nickel-iron complex exhibits a much larger Weiss constant of –1571, however it is evident from the susceptibility temperature data that this material interacts antiferromagnetically at high temperature.

Compared to the copper-manganese complex, the anomalous ferromagnetic orderings of the other metal complexes occurs at lower temperatures. The critical temperatures for the cobalt-copper and nickel-copper complexes are around 8 K and the critical temperatures for the nickel-manganese, nickel-iron, and nickel-cobalt complexes are around 20 K. In addition to showing lower critical temperatures, the maxima in $\chi_g T$ for these complexes are significantly reduced when compared with the copper-manganese complex. As with the critical temperature, the nickel-copper and cobalt-copper complexes show lower maxima in the susceptibility temperature product than the other three metal combinations.

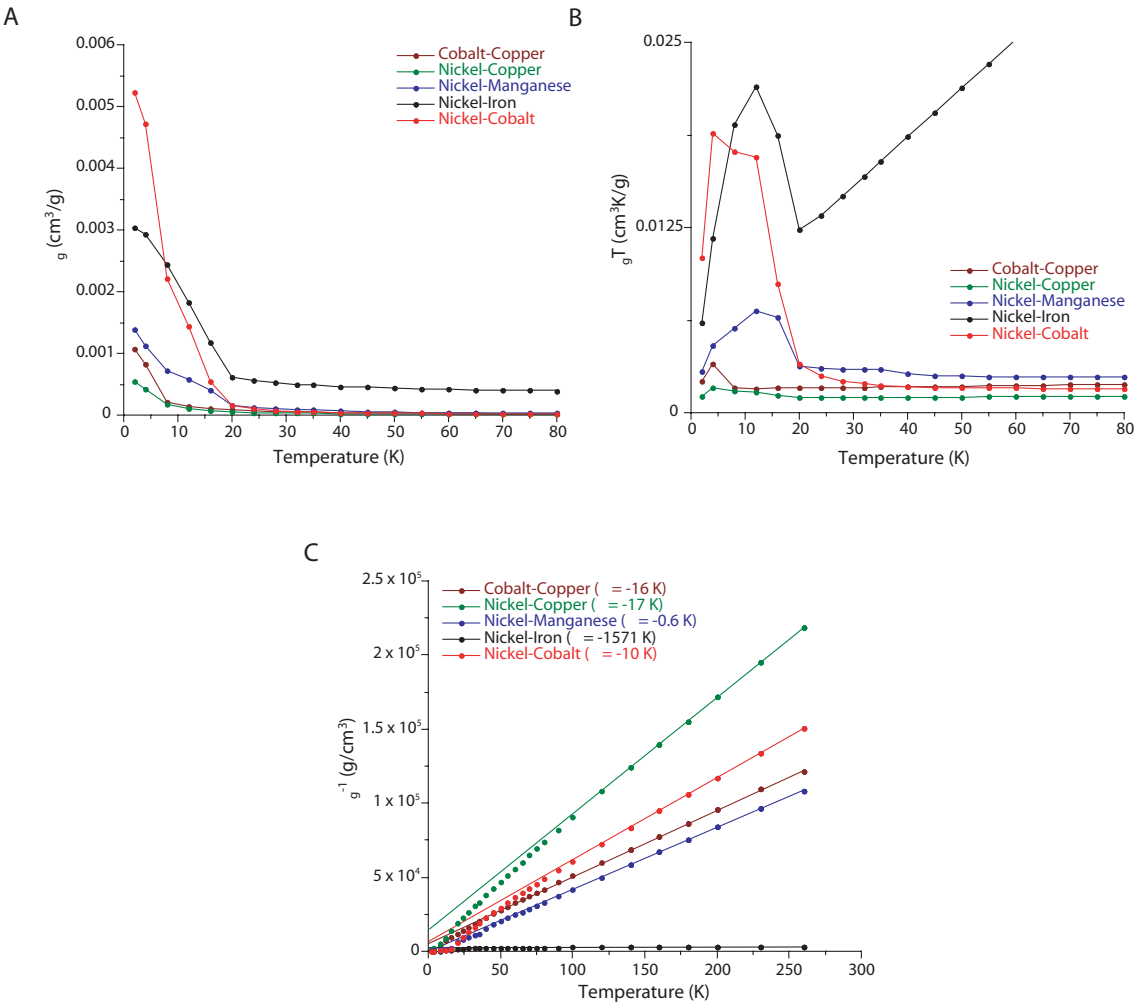

Figure 7.12: Susceptibility (A), susceptibility temperature product (B), and Curie (C) plots for the family of frustrated magnetic material obtained with an applied magnetic field of 100 G.

The creation of a family of complexes that exhibit frustrated magnetic behavior based on the guanidinium disulfonate crystal-engineering motif indicates the resilience of this motif. Although the copper manganese material is by far the most frustrated of this family, many of the materials seem to exhibit some degree of magnetic frustration.

7.3 Conclusions

The creation of interesting magnetic materials using the guanidinium sulfonate organic crystal-engineering motif establishes the potential of this approach. Well-defined organic crystal engineering motifs provide ways to rigidly control spin containing units and design novel magnetic materials.

The new class of magnetic materials that has been prepared using the guanidinium sulfonate motif and 5,5'-salendisulfonic acid exhibits massive magnetic frustration. The copper-manganese material has been extensively characterized using dc magnetic analysis and displays the classic signs of magnetic frustration. Although it is difficult to quantitate the extent of frustration in this system, the copper-manganese complex seems to display significant long-range frustration. The generality of the guanidinium sulfonate motif, using 5,5'-salen disulfonic acid as a bridging sulfonate, for the formation of magnetically frustrated materials was verified by the creation of family of six different magnetically frustrated bimetallic complexes.

7.4 Materials and Methods

Infrared Spectroscopy. Infrared spectra were recorded using a Perkin Elmer Paragon 1000 FT-IR between 4000 and 500 cm^{-1}. The spectra were obtained as KBr pellets.

Elemental Analysis. Carbon, hydrogen, nitrogen, and sulfur analysis was performed by Quantitative Technologies Inc. of Whitehouse, NJ. Copper and magnesium analysis was

performed using an Elan 5000A inductively coupled plasma mass spectrometer standardized with NIST traceable standards.

Magnetic Measurements. DC magnetization was measured using a Quantum Design MPMS-5 SQUID magnetometer from 1.8 to 300 K and between 0 and 5.5 T. All measurements were made on powdered samples in Delron screw-cap holders or gelatin capsules. The diamagnetic correction for the copper-manganese complex was obtained from the high temperature / high field data using the intercept of magnetic susceptibility vs. inverse temperature, as previously described and applied to the data for analysis of the susceptibility and the susceptibility temperature product (Murray et al., 1994). For other plots raw dc magnetization was used without correction.

Synthesis.

5,5'-Salen Disulfonic Acid. 5,5'-Salen disulfonic acid was prepared as previously described (Mukherjee and Ray, 1955).

Metal Complexes. Bimetallic metal complexes were prepared as described below for the Cu/Mn complex.

To a flask equipped with a reflux condenser and a stir bar was added 5,5'-salendisulfonic acid (0.250 g; 0.518 mmol), manganese (II) acetate (0.090 g; 0.518 mmol), copper (II) acetate monohydrate (0.103g; 0.518 mmol), and guanidinium acetate (0.246 g; 2.06 mmol). Distilled water (10 mL) and acetonitrile (40 mL) were added and the mixture

was allowed to reflux for 3 hours. The reaction mixture was hot filtered to give a pink/purple precipitate and a dark blue solution. The solid was washed with acetonitrile and acetone and allowed to air-dry (0.191 g). FTIR, KBr, n = IR 3406.4(vs,Broad), 3257.3(s), 3184.9(s), 3030.9(m), 2922.2(m), 2849.8(w), 1640.9(vs), 1601.4(s), 1535.0(m), 1492.1(w), 1465.8(m), 1380.8(m), 1333.6(w), 1302.9(m), 1189.8(s), 1116.3(s), 1084.5(m), 1052.8(w), 1032.1(vs), 971.3(w), 930.5(w), 898.9(w), 831.1(m), 749.7(w), 737.0(m), 697.5(m), 670.1(m), 621.3(s) cm^{-1}. XRD, Cu, 2q(counts/sec) = 5.0(540), 16.9(530), 19.4(340), 20.2(320), 25.4(400), 25.7(400), 26.0(400), 32.0(400), 36.0(430). Elemental analysis. Found: C, 29.82; H, 3.46; N, 11.45; S, 8.68; Cu, 9.28; Mn, 6.68.

7.5 Literature Cited

Aakeroy, C. B. (1997). Crystal Engineering: Strategies and Architectures. Acta Crystalographic *B53*, 569-586.

Alba, M., Hamman, J., Jacobini, C., and Pappa, C. (1982). Physical Letters *89A*, 423.

Becca, F., and Mila, F. (2002). Peierls-like transition induced by frustration in a two-dimensional antiferromagnet. Physical Review Letters *89*, art. no.-037204.

Coey, J. M. (1987). Noncollinear spin structures. Canadian Journal of Physics *65*, 1210-1232.

Desiraju, G. R. (1988). Angewandte Chemie International Edition English *34*, 2311.

Evans, C. C., Sukarto, L., and Ward, M. D. (1999). Sterically controlled architectural reversion in hydrogen- bonded crystalline clathrates. Journal of the American Chemical Society *121*, 320-325.

Garcia-Adeva, A. J., and Huber, D. L. (2002). Classical generalized constant-coupling method for geometrically frustrated magnets: Microscopic formulation and effect of perturbations beyond nearest-neighbor interactions. Physical Review B *65*, art. no.-184418.

Hirakawa, K., Kadowaki, H., and Ubukoshi, K. (1985). Journal of the Physical Society of Japan *54*, 3526.

Holm, R. H., Everett, G. W., and Chakravorty, A. (1966). Metal Complexes of Schiff Bases and beta-Ketoamines. In Progressin in Inorganic Chemistry, F. a. Cotton, ed. (New York, Interscience Publishers), pp. 83-214.

Kahn, O. (1993). Molecular Magnetism (New York, VCH Publishers, Inc.).

Kahn, O., Pei, Y., Verdaguer, M., Renard, J. P., and Sletten, J. (1988). Magnetic-Ordering of Mniicuii Bimetallic Chains - Design of a Molecular-Based Ferromagnet. Journal of the American Chemical Society *110*, 782-789.

Kruger, S. E., and Richter, J. (2001). Influence of quantum fluctuations on zero-temperature phase transitions between collinear and noncollinear states in frustrated spin systems. Physical Review B *6402*, art. no.-024433.

Manson, J. L., Ressouche, E., and Miller, J. S. (2000). Spin frustration in M(II) [C(CN)3]2 (M=V, Cr). A magnetism and neutron diffraction study. Inorganic Chemistry *39*, 1135-1141.

Miller, J. S., and Epstein, A. J. (1994). Orgainc and Organometallic Molecular Magnetic Materials - Designer Magnets. Angewandte Chemie International Edition English *33*, 385-415.

Mukherjee, A. K., and Ray, P. (1955). Metal chelate complexes of sulfosalicylaldhyde with polycyclic rings. Journal of the Indian Chemical Society *32*, 633-643.

Murray, M. M., Kaszynski, P., Kaisaki, D. A., Chang, W., and Dougherty, D. A. (1994). Prototypes for the Polaronic Ferromagnet. Synthesis and characterization of high-spin orgainc polymers. Journal of the American Chemical Society *116*, 8152-8161.

O'Brian, P. (1984). Copper. Coordination Chemistry Reviews *58*, 169-214.

Pei, Y., Verdaguer, M., Kahn, O., Sletten, J., and Renard, J. P. (1987). Magnetism of Mniicuii and Niiicuii Ordered Bimetallic Chains - Crystal-Structure of Mncu(Pba)(H2o)3.2h2o (Pba = 1,3- Propylenebis(Oxamato)). Inorganic Chemistry *26*, 138-143.

Ramirez, A. P., Espinosa, G. P., and Cooper, A. S. (1990). Strong Frustration and Dilution-Enhanced Order in a Quasi-2D Spin Glass. Physical Reviews Letters *64*, 2070-2073.

Russell, V. A., Etter, M. C., and Ward, M. D. (1994a). Guanidinium Parasubstituted Benzenesulfonates - Competitive Hydrogen-Bonding in Layered Structures and the Design of Nonlinear-Optical Materials. Chemistry of Materials *6*, 1206-1217.

Russell, V. A., Etter, M. C., and Ward, M. D. (1994b). Layered Materials by Molecular Design - Structural Enforcement by Hydrogen-Bonding in Guanidinium Alkanesulfonate and Arenesulfonate. Journal of the American Chemical Society *116*, 1941-1952.

Russell, V. A., Evans, C. C., Li, W. J., and Ward, M. D. (1997). Nanoporous molecular sandwiches: Pillared two-dimensional hydrogen-bonded networks with adjustable porosity. Science *276*, 575-579.

Russell, V. A., and Ward, M. D. (1996). Solid-state structure of a layered hydrogen-bonded salt: Guanidinium 5-benzoyl-4-hydroxy-2-methoxybenzenesulfonate methanol solvate. Acta Crystallographica Section B-Structural Science *52*, 209-214.

Russell, V. A., and Ward, M. D. (1997). Two-dimensional hydrogen-bonded assemblies: The influence of sterics and competitive hydrogen bonding on the structures of guanidinium arenesulfonate networks. Journal of Materials Chemistry *7*, 1123-1133.

Russell, V. A., and Ward, M. D. (1998). Interweaving of two-dimensional hydrogen-bonded networks directed by chloride ions. New Journal of Chemistry *22*, 149-153.

Siurakshina, L., Ihle, D., and Hayn, R. (2001). Magnetic order and finite-temperature properties of the two- dimensional frustrated Heisenberg model. Physical Review B *6410*, art. no.-104406.

Soghomonian, V., Chen, Q., Haushalter, R. C., Zubieta, J., O'Connor, C. J., and Lee, Y.-S. (1993). Organically Templated Open-Framework Vanadium Phosphates: Hydrothermal Synthesis, Structure, and Magnetic Properties of H3N(CH2)3NH3[(VO)3(OH)2(H2O)2(PO4)2]. Chemistry of Materials *5*, 1690-1691.

Stumpf, H. O., Ouahab, L., Pei, Y., Grandjean, D., and Kahn, O. (1993a). A Molecular-Based Magnet with a Fully Interlocked 3-Dimensional Structure. Science *261*, 447-449.

Stumpf, H. O., Pei, Y., Kahn, O., Sletten, J., and Renard, J. P. (1993b). Dimensionality of Mn(Ii)Cu(Ii) Bimetallic Compounds and Design of Molecular-Based Magnets. Journal of the American Chemical Society *115*, 6738-6745.

Svehla, G. (1996). Vogel's Qualitative Inorganic Analysis, seventh edn (Essex, Longman).

Swift, J. A., Pivovar, A. M., Reynolds, A. M., and Ward, M. D. (1998a). Template-directed architectural isomerism of open molecular frameworks: Engineering of crystalline clathrates. Journal of the American Chemical Society *120*, 5887-5894.

Swift, J. A., Reynolds, A. M., and Ward, M. D. (1998b). Cooperative host-guest recognition in crystalline clathrates: Steric guest ordering by molecular gears. Chemistry of Materials *10*, 4159-4168.

Swift, J. A., Russell, V. A., and Ward, M. D. (1997). Organoporous hosts with adjustable molecular environments. Advanced Materials *9*, 1183-&.

Swift, J. A., and Ward, M. D. (2000). Cooperative polar ordering of acentric guest molecules in topologically controlled host frameworks. Chemistry of Materials *12*, 1501.

Toulouse, G. (1977). Physics *2*, 115.

Tsunetsugu, H. (2001). Antiferromagnetic quantum spins on the pyrochlore lattice. Journal of the Physical Society of Japan *70*, 640-643.

Turnbull, M. M., Sugimoto, T., and Thompson, L. K., eds. (1996). Molecule-Based Magnetic Materials. Theory, Techniques, and Applications. (Washington, DC, American Chemical Society).

Villain, J. (1977). J Phys C *10*, 1717.

Yamaura, K., Takano, M., Hirano, A., and Kanno, R. (1996). Mangetic Properties of Li(1-x)Ni(1+X)O2(0<x<0.08). Journal of Solid State Chemistry *127*, 109-118.

Zukovic, M., Idogaki, T., and Takeda, K. (2002). Histogram Monte Carlo simulation of the geometrically frustrated XY antiferromagnet with biquadratic exchange. Physical Review B *65*, art. no.-144410.

Appendix I : Supplementary Data for the Crystal Structure of N-phenylsalicylidene sulfonic acid guanidinium

I.1 Tables

Table 1. Crystal data and structure refinement for JEM1.

Empirical formula	$C_{14}H_{16}N_4O_4S$
Formula weight	336.37

Data Collection

Type of diffractometer	CCD area detector
Wavelength	0.71073 Å MoKα
Data Collection Temperature	293 K
θ range for reflections used in lattice determination	2.10 to 23.34°
Unit cell dimensions	a = 7.3650(15) Å b = 17.578(4) Å β= 98.48(3)° c = 11.727(2) Å
Volume	1501.7(5) $Å^3$
Z	4
Crystal system	Monoclinic
Space group	$P2_1/c$
Density (calculated)	1.488 Mg/m^3
F(000)	704
θ range for data collection	2.10 to 23.34°
Completeness to θ = 23.34°	99.1 %
Index ranges	$-8 \le h \le 8, -18 \le k \le 19, -11 \le l \le 13$
Data collection scan type	ω scans at 3 ϕ settings
Reflections collected	6820
Independent reflections	2168 [R_{int}= 0.0805]
Absorption coefficient	0.243 mm^{-1}
Absorption correction	None

Table 1 (cont.)

Structure solution and Refinement

Structure solution program	SHELXS-97 (Sheldrick, 1990)
Primary solution method	Direct methods
Secondary solution method	Difference Fourier map
Hydrogen placement	Geometric positions
Structure refinement program	SHELXL-97 (Sheldrick, 1997)
Refinement method	Full matrix least-squares on F^2
Data / restraints / parameters	2168 / 0 / 209
Treatment of hydrogen atoms	Riding
Goodness-of-fit on F^2	3.704
Final R indices [I>2□(I)]	R1 = 0.1101, *w*R2 = 0.1841
R indices (all data)	R1 = 0.1350, *w*R2 = 0.1858
Type of weighting scheme used	Sigma
Weighting scheme used	$w=1/□^2(Fo^2)$
Max shift/error	0.000
Average shift/error	0.000
Largest diff. peak and hole	1.188 and -0.381 e.Å^{-3}

Special Refinement Details

These crystals of N-phenylsalicylidene sulfonic acid guanidinium are twinned. It was not possible to obtain satisfactory refinement results when applying the twinning algorithms. Therefore the twinning was ignored. The overall structure is correct but is not of sufficient quality to publish.

Refinement of F^2 is against ALL reflections. The weighted R-factor (*w*R) and goodness of fit (S) are based on F^2, conventional R-factors (R) are based on F, with F set to zero for negative F^2. The threshold expression of $F^2 > 2□(F^2)$ is used only for calculating R-factors(gt) etc. and is not relevant to the choice of reflections for refinement. R-factors based on F^2 are statistically about twice as large as those based on F, and R-factors based on ALL data will be even larger.

All esds (except the esd in the dihedral angle between two l.s. planes) are estimated using the full covariance matrix. The cell esds are taken into account individually in the estimation of esds in distances, angles and torsion angles; correlations between esds in cell parameters are only used when they are defined by crystal symmetry. An approximate (isotropic) treatment of cell esds is used for estimating esds involving l.s. planes.

Table 2. Atomic coordinates (x 10^4) and equivalent isotropic displacement parameters (Å^{2}x 10^3) for JEM1. U(eq) is defined as the trace of the orthogonalized U^{ij} tensor.

	x	y	z	U_{eq}
S(1)	2243(3)	7275(1)	894(2)	46(1)
O(1)	3405(8)	4325(3)	3275(4)	56(2)
O(2)	1770(7)	7079(3)	-322(4)	56(2)
O(3)	3937(7)	7703(3)	1071(4)	57(1)
O(4)	768(7)	7644(3)	1338(4)	60(2)
N(1)	2543(8)	4956(3)	5072(4)	45(2)
C(1)	3173(11)	4999(4)	2766(7)	48(2)
C(2)	3504(11)	5081(4)	1660(7)	47(2)
C(3)	3213(11)	5757(4)	1081(6)	52(2)
C(4)	2643(10)	6409(4)	1643(6)	43(2)
C(5)	2397(10)	6342(4)	2775(6)	45(2)
C(6)	2652(10)	5661(4)	3339(6)	41(2)
C(7)	2360(10)	5587(5)	4531(6)	49(2)
C(8)	2224(11)	4861(4)	6242(7)	50(2)
C(9)	1695(11)	5455(4)	6931(6)	51(2)
C(10)	1433(11)	5250(5)	8033(7)	57(2)
C(11)	1642(12)	4550(6)	8466(7)	62(2)
C(12)	2165(12)	3963(5)	7772(7)	68(3)
C(13)	2454(11)	4130(5)	6676(6)	53(2)
N(20)	7078(9)	7606(4)	4961(6)	66(2)
N(21)	8097(10)	8069(4)	3347(6)	64(2)
N(22)	5016(9)	8089(4)	3501(5)	60(2)
C(20)	6747(13)	7925(4)	3936(8)	52(2)

Table 3. Bond lengths [Å] and angles [°] for JEM1.

S(1)-O(4)	1.427(5)	C(2)-C(1)-C(6)	117.5(7)
S(1)-O(3)	1.445(5)	C(1)-C(2)-C(3)	121.7(7)
S(1)-O(2)	1.459(5)	C(1)-C(2)-H(2B)	119.1
S(1)-C(4)	1.761(8)	C(3)-C(2)-H(2B)	119.1
O(1)-C(1)	1.327(8)	C(2)-C(3)-C(4)	120.4(7)
O(1)-H(1A)	0.8200	C(2)-C(3)-H(3B)	119.8
N(1)-C(7)	1.276(8)	C(4)-C(3)-H(3B)	119.8
N(1)-C(8)	1.436(8)	C(5)-C(4)-C(3)	118.1(7)
C(1)-C(2)	1.363(9)	C(5)-C(4)-S(1)	121.5(6)
C(1)-C(6)	1.424(10)	C(3)-C(4)-S(1)	120.4(6)
C(2)-C(3)	1.370(10)	C(6)-C(5)-C(4)	121.1(7)
C(2)-H(2B)	0.9300	C(6)-C(5)-H(5A)	119.5
C(3)-C(4)	1.416(10)	C(4)-C(5)-H(5A)	119.5
C(3)-H(3B)	0.9300	C(5)-C(6)-C(1)	120.9(7)
C(4)-C(5)	1.372(8)	C(5)-C(6)-C(7)	121.0(7)
C(5)-C(6)	1.366(10)	C(1)-C(6)-C(7)	118.0(7)
C(5)-H(5A)	0.9300	N(1)-C(7)-C(6)	122.5(7)
C(6)-C(7)	1.452(9)	N(1)-C(7)-H(7A)	118.8
C(7)-H(7A)	0.9300	C(6)-C(7)-H(7A)	118.8
C(8)-C(13)	1.382(10)	C(13)-C(8)-C(9)	120.4(7)
C(8)-C(9)	1.410(10)	C(13)-C(8)-N(1)	115.5(7)
C(9)-C(10)	1.382(10)	C(9)-C(8)-N(1)	124.0(7)
C(9)-H(9A)	0.9300	C(10)-C(9)-C(8)	115.5(8)
C(10)-C(11)	1.330(11)	C(10)-C(9)-H(9A)	122.2
C(10)-H(10A)	0.9300	C(8)-C(9)-H(9A)	122.2
C(11)-C(12)	1.403(11)	C(11)-C(10)-C(9)	125.0(8)
C(11)-H(11A)	0.9300	C(11)-C(10)-H(10A)	117.5
C(12)-C(13)	1.365(9)	C(9)-C(10)-H(10A)	117.5
C(12)-H(12A)	0.9300	C(10)-C(11)-C(12)	119.0(8)
C(13)-H(13A)	0.9300	C(10)-C(11)-H(11A)	120.5
N(20)-C(20)	1.316(10)	C(12)-C(11)-H(11A)	120.5
N(20)-H(20A)	0.8600	C(13)-C(12)-C(11)	118.7(8)
N(20)-H(20B)	0.8600	C(13)-C(12)-H(12A)	120.6
N(21)-C(20)	1.316(9)	C(11)-C(12)-H(12A)	120.6
N(21)-H(21A)	0.8600	C(12)-C(13)-C(8)	121.3(8)
N(21)-H(21B)	0.8600	C(12)-C(13)-H(13A)	119.4
N(22)-C(20)	1.333(10)	C(8)-C(13)-H(13A)	119.4
N(22)-H(22A)	0.8600	C(20)-N(20)-H(20A)	120.0
N(22)-H(22B)	0.8600	C(20)-N(20)-H(20B)	120.0
O(4)-S(1)-O(3)	113.5(3)	H(20A)-N(20)-H(20B)	120.0
O(4)-S(1)-O(2)	112.3(3)	C(20)-N(21)-H(21A)	120.0
O(3)-S(1)-O(2)	109.9(3)	C(20)-N(21)-H(21B)	120.0
O(4)-S(1)-C(4)	106.9(3)	H(21A)-N(21)-H(21B)	120.0
O(3)-S(1)-C(4)	107.5(3)	C(20)-N(22)-H(22A)	120.0
O(2)-S(1)-C(4)	106.4(3)	C(20)-N(22)-H(22B)	120.0
C(1)-O(1)-H(1A)	109.5	H(22A)-N(22)-H(22B)	120.0
C(7)-N(1)-C(8)	123.8(6)	N(21)-C(20)-N(20)	120.6(9)
O(1)-C(1)-C(2)	119.5(7)	N(21)-C(20)-N(22)	120.7(8)
O(1)-C(1)-C(6)	122.9(7)	N(20)-C(20)-N(22)	118.7(8)

Table 4. Anisotropic displacement parameters ($Å^2 x\ 10^4$) for JEM1. The anisotropic displacement factor exponent takes the form: $-2\pi^2 [h^2 a^{*2} U^{11} + ... + 2 h k a^* b^* U^{12}]$

	U^{11}	U^{22}	U^{33}	U^{23}	U^{13}	U^{12}
S(1)	582(13)	425(12)	370(12)	26(10)	35(9)	-42(12)
O(1)	940(40)	360(30)	370(30)	-40(30)	50(30)	70(30)
O(2)	700(40)	540(40)	400(30)	0(30)	-30(30)	-50(30)
O(3)	670(30)	570(30)	470(30)	70(30)	40(30)	-240(30)
O(4)	750(40)	480(30)	590(30)	90(30)	230(30)	180(30)
N(1)	750(50)	300(40)	270(40)	10(30)	10(30)	0(40)
C(1)	550(50)	370(50)	520(50)	80(40)	50(40)	0(40)
C(2)	640(50)	370(50)	390(50)	-90(40)	60(40)	50(40)
C(3)	640(50)	500(60)	430(50)	-90(40)	100(40)	-50(50)
C(4)	500(50)	390(50)	390(50)	-40(40)	20(40)	-60(40)
C(5)	600(50)	350(50)	400(50)	-40(40)	70(40)	-60(40)
C(6)	540(50)	400(50)	280(40)	-50(40)	10(40)	-50(40)
C(7)	590(50)	440(50)	440(50)	-60(40)	20(40)	-10(40)
C(8)	570(50)	380(50)	510(50)	90(40)	-10(40)	-80(40)
C(9)	860(60)	400(50)	270(40)	-150(40)	90(40)	-80(50)
C(10)	690(60)	640(60)	350(50)	-100(40)	-60(40)	10(50)
C(11)	720(60)	790(70)	360(50)	-90(50)	100(40)	-180(60)
C(12)	850(70)	620(60)	550(60)	190(50)	0(50)	-120(50)
C(13)	710(60)	420(50)	410(50)	20(40)	-30(40)	20(40)
N(20)	620(40)	610(50)	760(50)	60(40)	140(40)	80(40)
N(21)	700(50)	690(50)	550(40)	40(40)	130(40)	0(40)
N(22)	650(50)	720(50)	430(40)	20(30)	60(30)	0(40)
C(20)	640(60)	270(50)	670(60)	-100(40)	150(50)	-40(40)

Table 5. Hydrogen coordinates (x 10^4) and isotropic displacement parameters ($Å^2$x 10^3) for JEM1.

	x	y	z	U_{iso}
H(1A)	3177	4357	3937	84
H(20A)	8183	7488	5251	79
H(20B)	6188	7514	5340	79
H(21A)	9207	7954	3631	77
H(21B)	7870	8278	2678	77
H(22A)	4771	8291	2827	72
H(22B)	4144	7993	3893	72
H(2B)	3940	4667	1288	56
H(3B)	3390	5789	313	62
H(5A)	2051	6766	3166	54
H(7A)	2028	6017	4916	59
H(9A)	1534	5952	6662	61
H(10A)	1083	5630	8508	69
H(11A)	1444	4452	9217	74
H(12A)	2312	3468	8053	82
H(13A)	2811	3745	6212	63

Table 6. Hydrogen bonds for JEM1 [Å and °].

D-H...A	d(D-H)	d(H...A)	d(D...A)	<(DHA)
O(1)-H(1A)...N(1)	0.82	1.81	2.543(7)	147.9
N(20)-H(20A)...O(4)#1	0.86	2.14	2.983(9)	165.5
N(20)-H(20B)...O(3)#2	0.86	2.01	2.868(8)	174.1
N(21)-H(21A)...O(2)#1	0.86	2.10	2.928(8)	162.9
N(21)-H(21B)...O(1)#3	0.86	2.28	3.017(8)	143.3
N(22)-H(22A)...O(3)	0.86	2.31	2.923(7)	128.8
N(22)-H(22B)...O(2)#2	0.86	2.10	2.947(8)	169.6

Symmetry transformations used to generate equivalent atoms:
#1 x+1,-y+3/2,z+1/2 #2 x,-y+3/2,z+1/2 #3 -x+1,y+1/2,-z+1/2

I.2 Figures

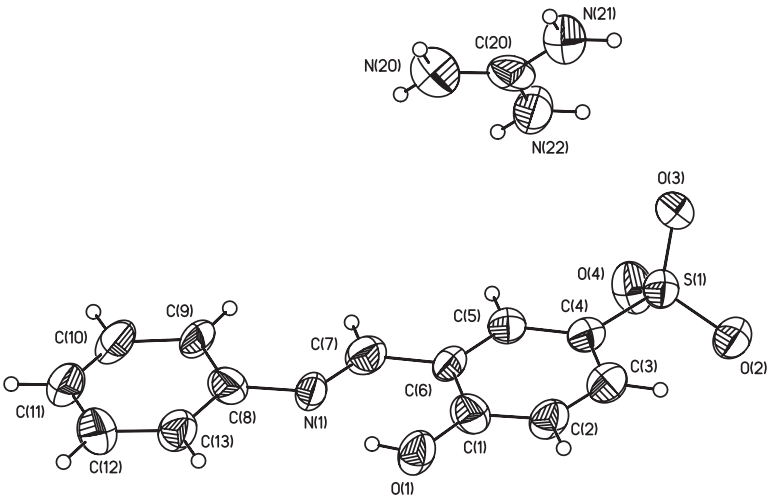

Figure I.1: Structural components of N-phenylsalicylidene sulfonic acid guanidinium.

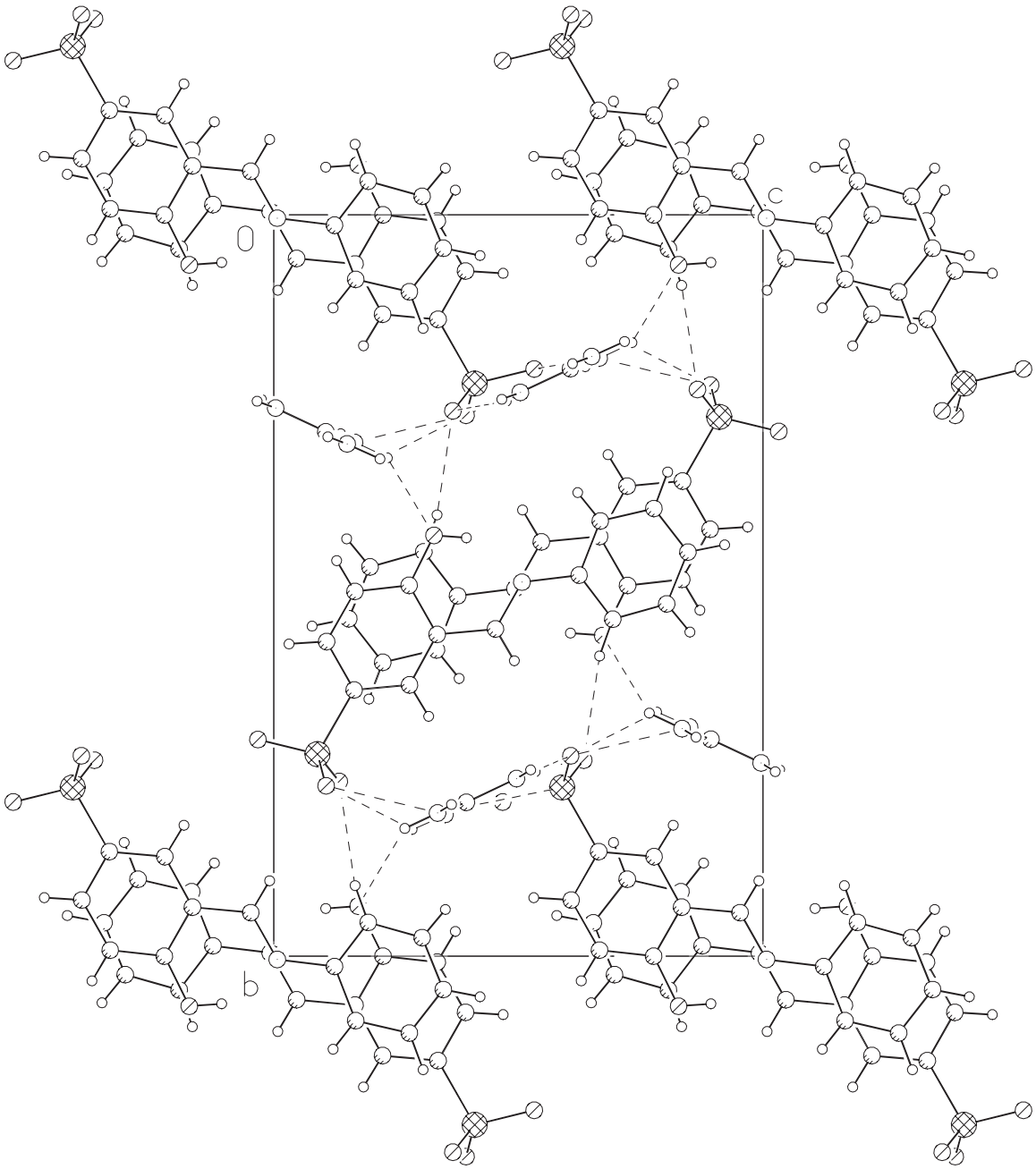

Figure I.2: View of N-phenylsalicylidene sulfonic acid guanidinium along the bc plane.

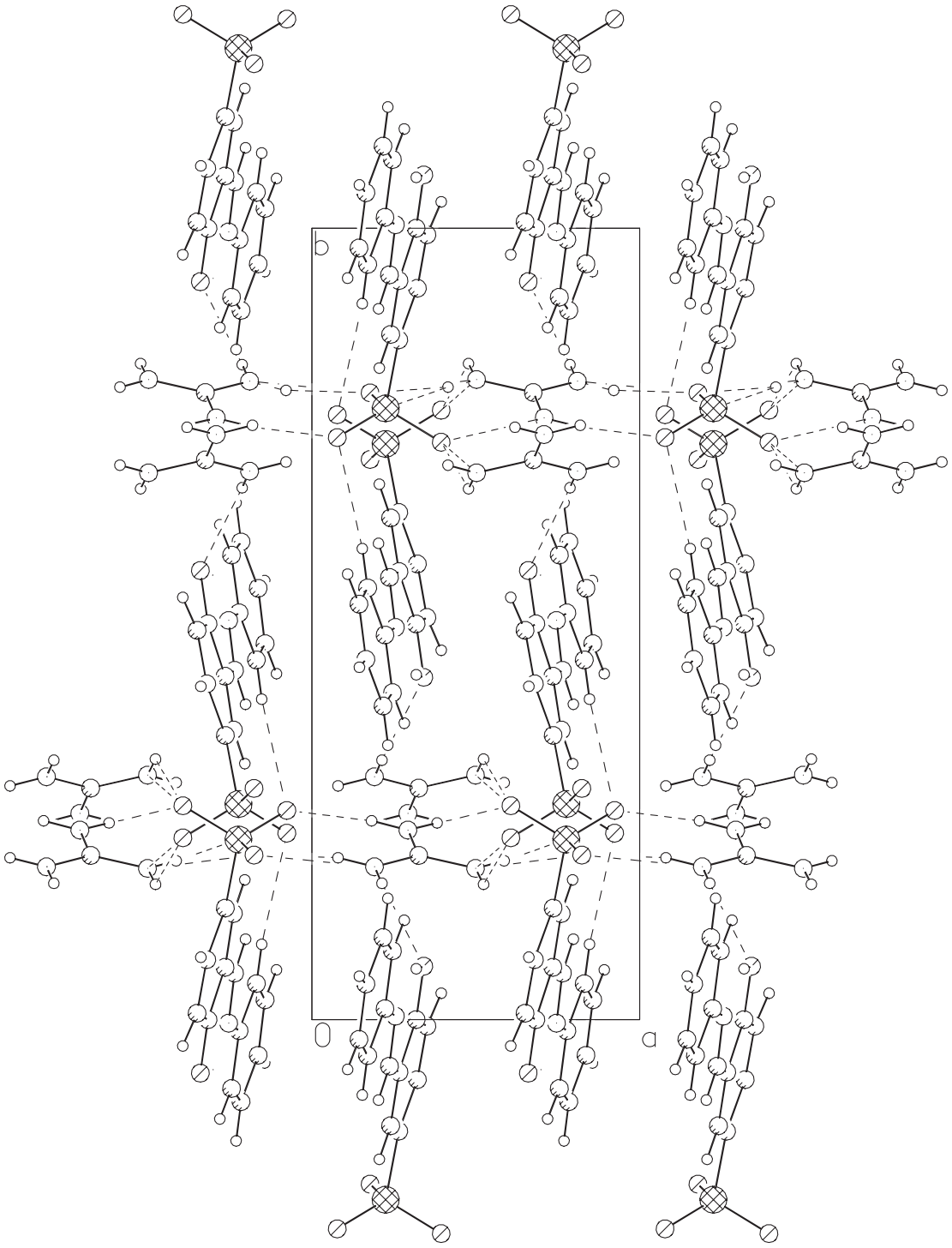

Figure I.3: View of the N-phenylsalicylidene sulfonic acid guanidinium structure along the ab plane.

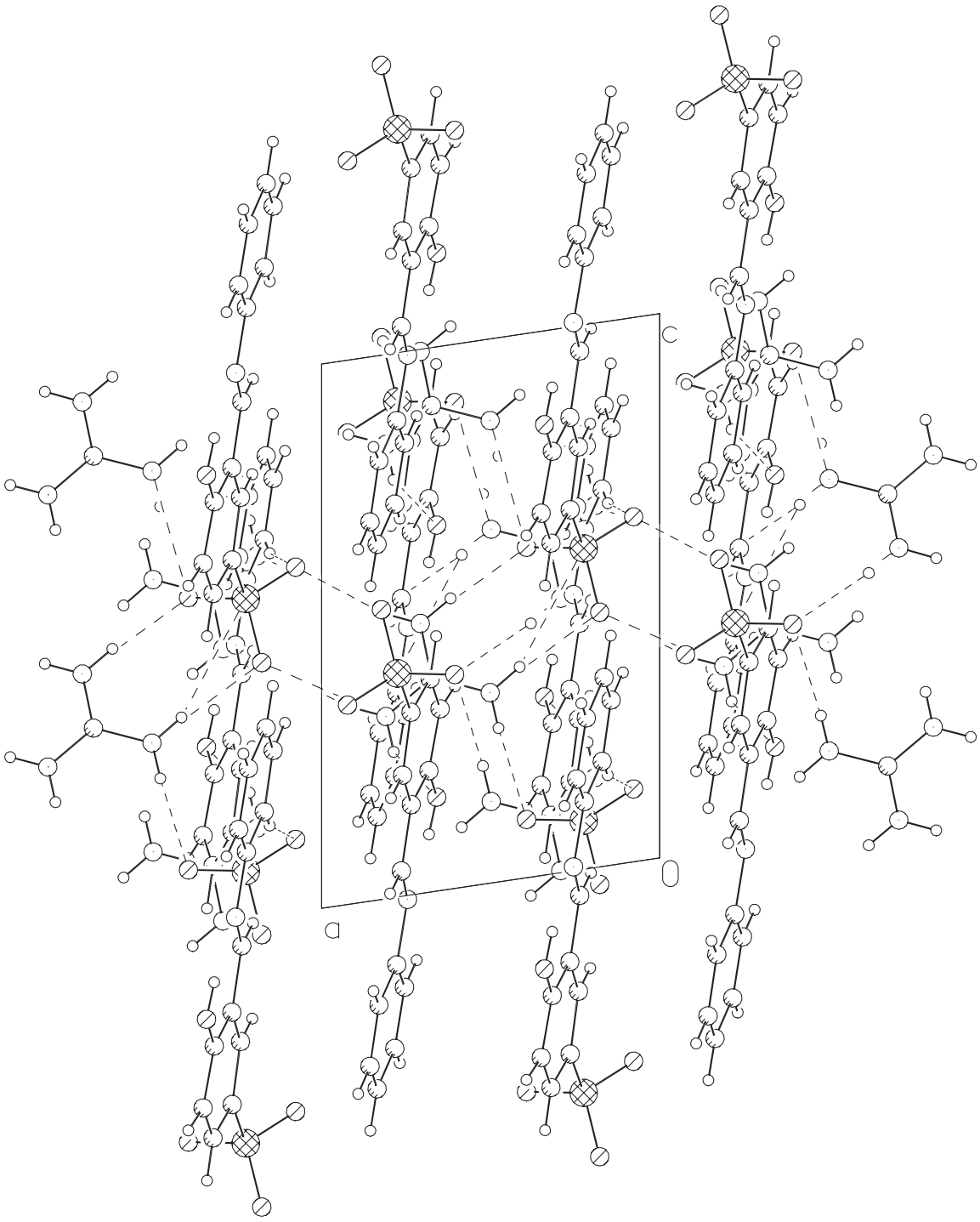

Figure I.4: View of the N-phenylsalicylidene sulfonic acid guanidinium structure along the ac plane.

Appendix II: Towards the Development of a High-spin Organic Polymer

II.1 Introduction

The development of pure organic materials with ferromagnetic properties is of long standing theoretical and experimental interest. To obtain high-spin organic materials, it is necessary to control spin-spin interactions of organic radicals. Spin control in organic radicals can be divided into intermolecular control and intramolecular control. Chapter 7 and Appendix III deal with controlling intermolecular interactions using crystal engineering, and here we discuss control of intramolecular interactions using organic polymers.

The model shown in Figure II.1 describes the simplest high-spin organic polymer (Dougherty, 1991). This system can be broken down into two pieces: a spin containing unit and a ferromagnetic coupling unit. For development of organic ferromagnets, organic radicals serve as spin containing units. The ferromagnetic coupling unit is responsible for ensuring that adjacent spins align parallel with respect to each other.

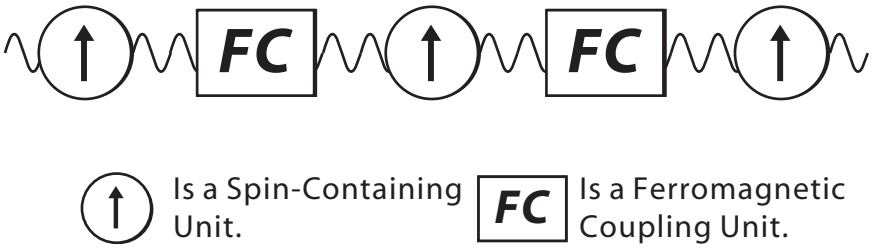

Figure II.1: Schematic for a one-dimensional ferromagnetic polymer.

Previous work from our group has identified three ferromagnetic coupling units, *meta*-phenylene, 1,1-ethylene, and substituted 1,3-cyclobutanediyls (Jacobs et al., 1993). Of these, the most robust ferromagnetic coupling unit is *meta*-phenylene, with a singlet-triplet gap of around 10 kcal/mol. The work described here will utilize the *meta*-phenylene coupling unit with two different spin containing units.

The smallest spin containing units for organic magnetic materials are charged or uncharged monoradicals. Although some monoradicals are stable, typically simple organic radicals are only stable at very low temperatures in solid matrices. Results from conducting polymers have shown that polarons, delocalized radical cations or radical anions, can be easily generated and are relatively stable at room temperature. For this reason, this work and previous work has employed polarons as the spin containing units for the development of ferromagnetic organic polymers.

Traditionally, work in our group has focused on the use of oxidatively doped radical cations as spin containing units (Murray et al., 1994). Figure II.2 shows a series of polymers that have been oxidatively doped to produce radical cations. All of these polymers showed spin values greater than one half at very low spin concentrations, suggesting parallel alignment between adjacent radicals. However, at high-spin concentrations, above one percent, typically the spin values observed were well below one, which is most likely indicative of bipolaron (spinless dication) formation and/or decomposition of the material. In these systems it was thus impossible to generate the large number of aligned spins needed to achieve long-range magnetic behavior.

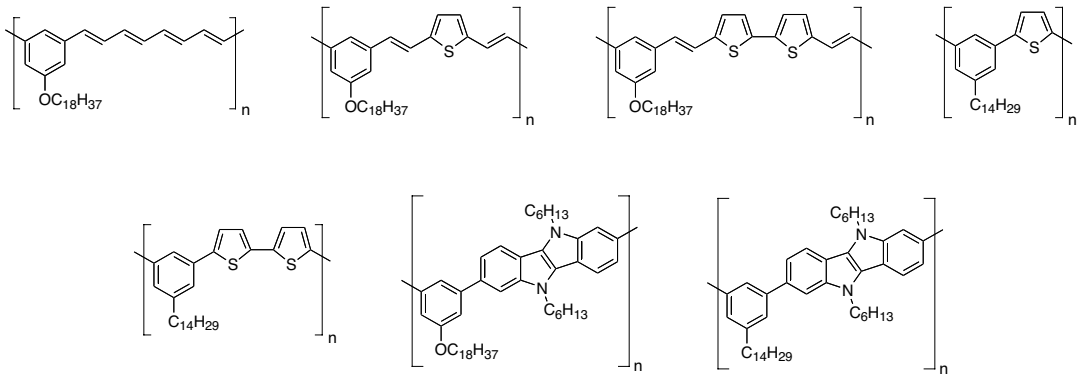

Figure II.2: Model one-dimensional oxidatively doped polaronic ferromagnets.

Many of the problems associated with the early prototypical oxidatively doped radical cation systems were resolved by introduction of a reductively doped radical anion spin containing unit (Anderson and Dougherty, 1998). 2,6-di-□□□-butylfuchsone was chosen, since its radical anion is readily generated electrochemically in solution and the second reduction potential is sufficiently removed (~ 400 mV) to prevent formation of large amounts of bipolarons. Using this spin containing unit, polymer **1** was produced.

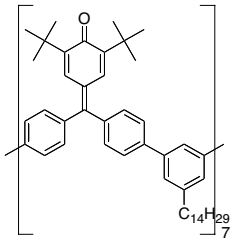

1

Polymer **1** showed improved magnetic properties upon electrochemical reduction between –1.0 V and –1.4 V verses Ag(s)/AgCl(s). With this material a spin value of 2.0 at a spin concentration of 58% was achieved. Additionally, analysis of the susceptibility

temperature product as a function of temperature showed a ferromagnetic transition at around 40 K followed by an antiferrromagnetic transition around 3 K. Presumably the observed antiferromagnetic transition arises from weak antiferromagnetic intermolecular interactions.

Despite significantly improved magnetic behavior, reductive doping of polymer **1** remained problematic. For solubility reasons, electrochemistry of **1** had to be carried out in tetrahydrofuran. Tetrahydrofuran is a poor solvent for electrochemistry since it requires high electrolyte concentrations to achieve usable electrochemical cell resistances. As a result during bulk electrolysis decomposition of the electrolyte solution in the counter cell was observed along with corrosion of the Ag(s)/AgCl(s) working electrode. Here we describe modification of polymer **1** to increase its solubility in good electrochemical solvents, such as acetonitrile. It was hoped that such a polymer might increase the efficiency of the electrochemical reduction, thus giving high-spin values and higher spin concentrations.

In addition to modifying the solubility of polymer **1**, it was hope that analogous polymers could be produced in which ferromagnetic behavior was observed at higher temperatures. Theoretically, the ferromagnetic critical temperature is simply a consequence of the singlet-triplet gap for the coupling unit and the spin density of the spin containing unit at the connection point. Since *meta*-phenylene already has the largest singlet-triplet gap of the identified ferromagnetic coupling units, modulation of ferromagnetic critical temperature was attempted by modulation of the spin density at the connection point.

Figure II.3 shows the spin density at the central carbon of 2,6-di-*tert*-butylfuchsone and the spin density at the connection point between 2,6-di-*tert*-butylfuchsone and *meta*-phenylene in polymer **1**. The calculated spin densities shown are from Huckel calculations, and the experimental spin density is from EPR measurements. The theoretical coupling strength for polymer **1** can be calculated by scaling the singlet triplet gap for *meta*-xylene (10 kcal/mol) by the square of the spin density at the connection point (0.066 or 0.09). A resulting coupling strength of 40-90 cal/mol is obtained, which corresponds to ferromagnetic critical temperature between 20 and 45 K. The predicted ferromagnetic critical temperature is in good agreement with observed critical temperature for polymer **1**.

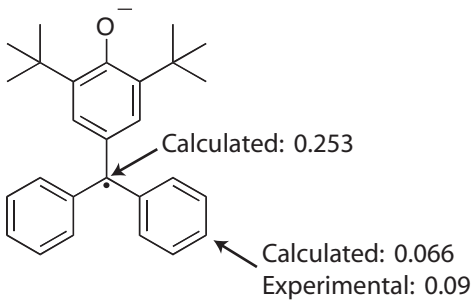

Figure II.3: Selected spin densities are shown from the 2,6-di-*tert*-butylfuchsone radical anion.

Based on these considerations polymers **2** and **3** were designed to have increased spin density at the connection point between the spin containing unit and the ferromagnetic coupling unit. Calculating the theoretical coupling strength as above, polymers **2** and **3** have coupling strength of 170 cal/mol and 640 cal/mol respectively. These correspond to

ferromagnetic critical temperatures of 85 K and 320 K. The synthesis and electrochemical characterization of polymer **2** are described here.

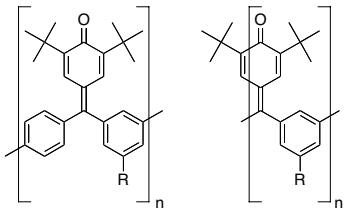

2 **3**

II.2 Results and Discussion

*II.2.1 Increasing the Solubility of Polymer **1***

Polymer **1** contains a long alkyl chain to confer solubility in organic solvent. In an attempt to increase the solubility of polymer **1** in polar solvents suitable for electrochemisty, the alkyl chain was modified to a poly(ethylene)glycol chain to give polymer **4**. The synthesis of polymer **4** is described in Scheme II.1.

The resulting polymer was characterized by gel permiation chromatography in methylene chloride. An apparent molecular weight of 5,690 g/mol and a polydispersity index of 2.4 was obtained. This corresponds to an oligomer consisting of approximately 11 monomer units.

Polymer **4** was only sparingly soluble in pure acetonitrile, but it showed increased solubility in acetonitrile over polymer **1** and readily dissolved in 1:1 acetonitrile:THF. Cyclic voltammetry was perfomed on polymer **4** in acetonitrile, 1:1 acetonitrile:THF, and

pure THF. Figure II.4 shows a comparison of the results of obtained from cyclic votammetry on polymer **4**.

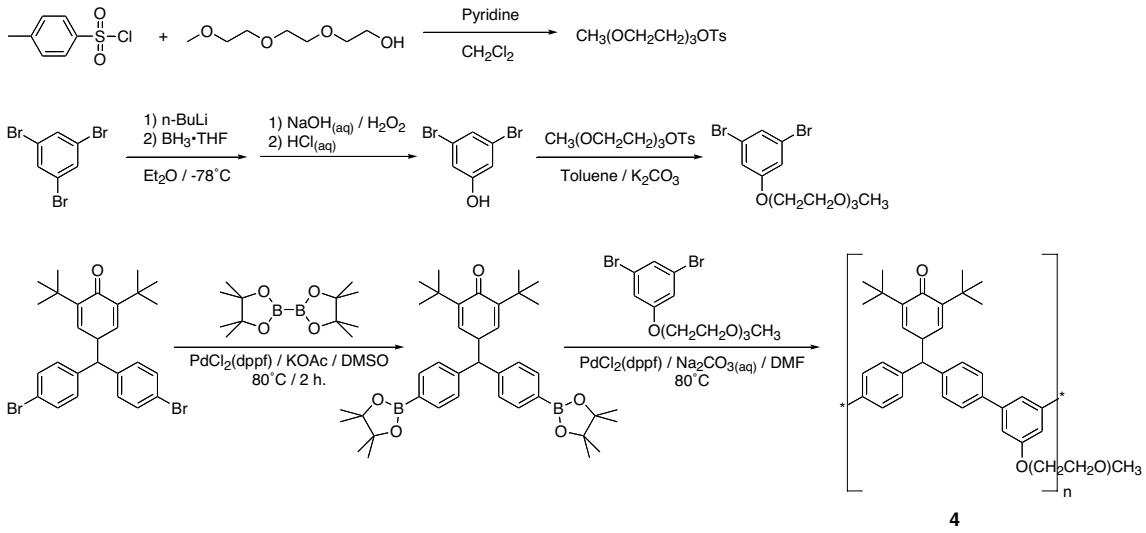

Scheme II.1: Synthesis of polymer **4**.

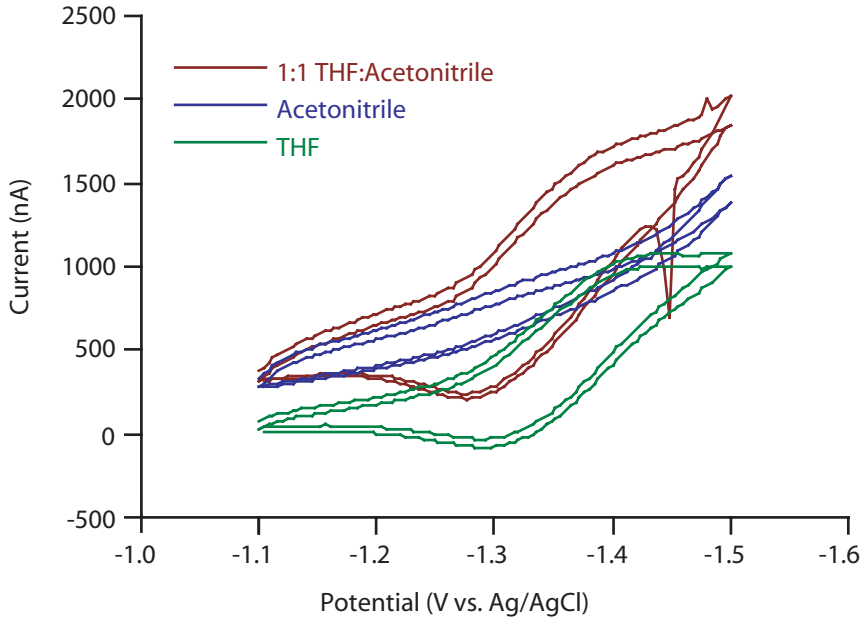

Figure II.4: Cyclic voltammograms for polymer 3 in THF, acetonitrile, and 1:1 THF:acetonitrile.

The cyclic voltammograms obtained in acetonitrile were essentially shapeless, due to the poor solubility of polymer **4** in acetonitrile. The curves obtained for cyclic voltammetry in THF and 1:1 acetonitrile:THF were qualitatively similar to each other. Additionally, the cyclic voltammogram for polymer **4** was qualitatively similar to that of polymer **1**.

Since in principle 1:1 acetonitrile:THF is a better solvent mixture for electrochemistry than THF, bulk electrolysis of polymer **4** was attempted in 1:1 acetonitrile:THF using 0.3 M tetrabutyl ammonium perchlorate as electrolyte. Over the course of the electrical reduction, rapid degradation of the solid Ag/AgCl reference electrode was observed at the potentials necessary for reduction of the polymer **4**. Solid Ag/AgCl reference electrodes are also known to lack stability in other good electrochemistry solvents (such as DMF or DMSO). To resolve this problem a different reference electrode is needed, such as a solution Ag/AgCl electrode, a saturated calomel electrode, or a dropping mercury electrode. However, it is not obvious that the gains from electrochemistry in a higher dielectric solvent would be significant to merit further investigation.

*II.2.2 Synthesis and Electrochemical Characterization of Polymer **2***

The synthesis of polymer **2** was carried out as described in Scheme II.2. This synthetic strategy takes advantage of the selectivity of the diboron reaction for iodide over bromide when installing the boric ester necessary for the final polymerization. Additionally, since the poly(ethyleneglycol) tail is installed towards the end of the synthesis, variation of polymer solubility, by variation of this tail, should be straight forward.

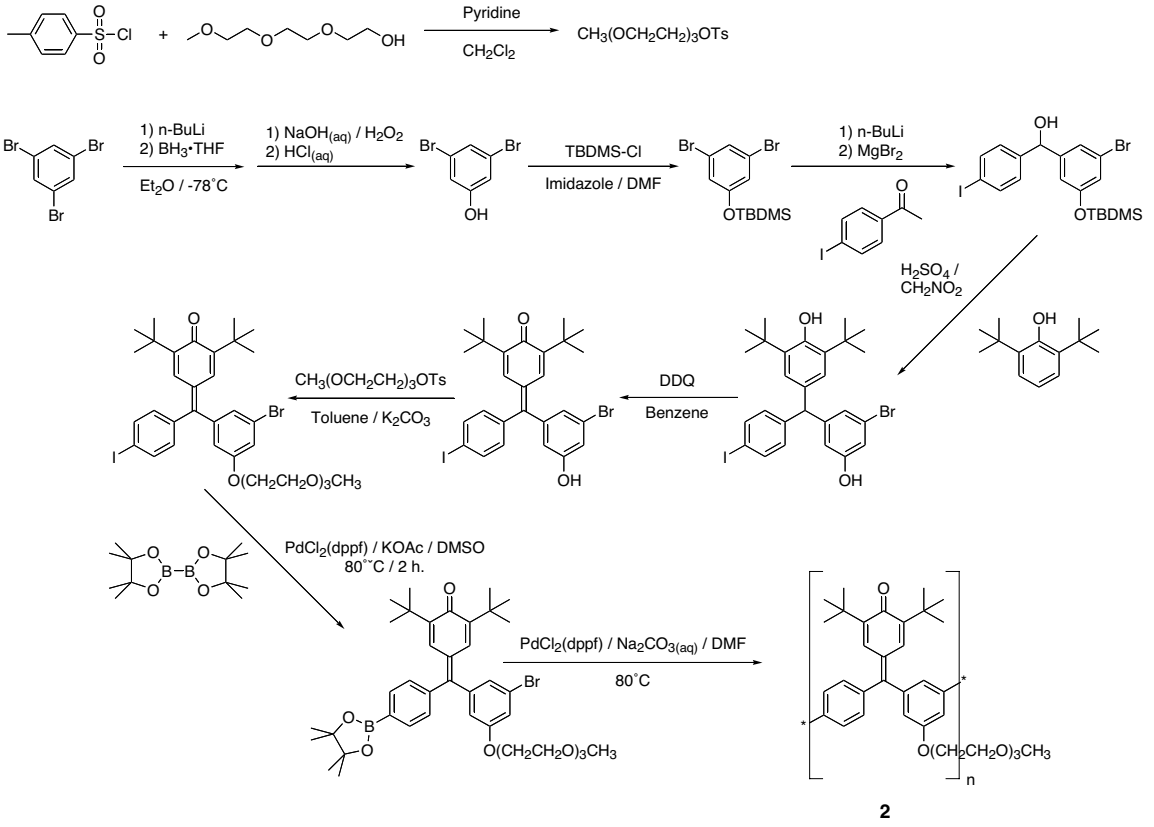

Scheme II.2: Synthesis of polymer **2**.

Gel permeation chromatography of polymer **2** was carried out in methylene chloride. Polymer 2 showed an apparent molecular weight of 21,708 g/mol and a polydispersity index of 1.9. This corresponds to an approximate oligomerization state of 41 monomers per polymer unit.

A cyclic voltammogram of polymer **2** was obtained in THF (Figure II.5). As expected the general shape of the voltammogram was similar to that polymers for **1** and **4**. The first reduction potential for the fuschone was observed around –1.3 V versus silver/silver chloride.

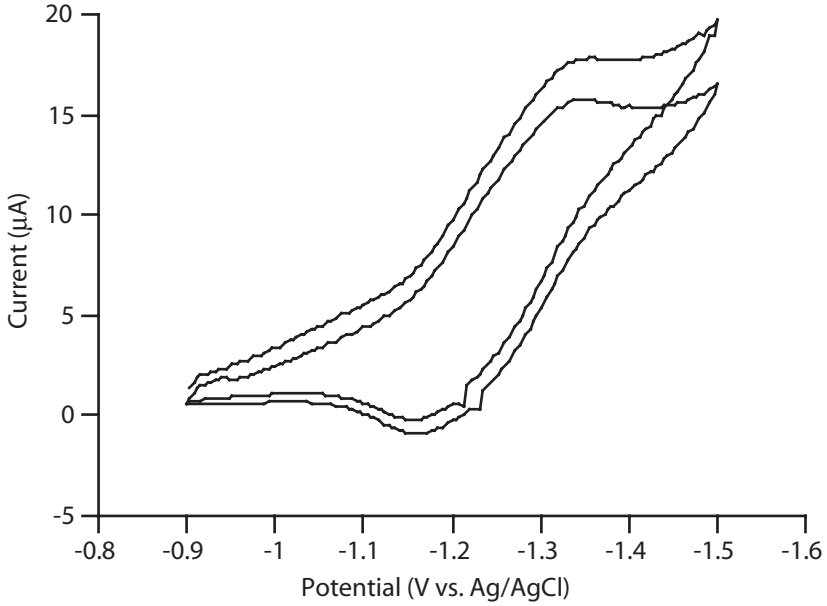

Figure II.5: Cyclic voltammogram for polymer **2** in THF.

Bulk electrolysis of polymer **2** at –1.3V versus silver/silver chloride was attempted in THF with tetrabutyl ammonium electrolyte. The resulting product showed no paramagnetic species by SQUID magnetometry. The lack of fuschone radical formation may be due to problems encountered during the bulk electrolysis or may be due to issues of sample handling. The electrochemical reduction of polymer **2** merits further investigation as it may be possible to achieve good electrochemistry, using a more ideal electrochemical setup than the one employed here.

II.3 Literature Cited.

Anderson, K. K., and Dougherty, D. A. (1998). An improved model for one-dimensional polaronic ferromagnetism: Electrochemically doped poly(m-phenylenefuchsone). Advanced Materials□□□, 688-692.

Dougherty, D. A. (1991). Spin Control in Organic-Molecules. Accounts of Chemical Research *24*, 88-94.

Jacobs, S. J., Shultz, D. A., Jain, R., Novak, J., and Dougherty, D. A. (1993). Evaluation of Potential Ferromagnetic Coupling Units - the Bis(Tmm) Approach to High-Spin Organic-Molecules. Journal of the American Chemical Society *115*, 1744-1753.

Murray, M. M., Kaszynski, P., Kaisaki, D. A., Chang, W. H., and Dougherty, D. A. (1994). Prototypes for the Polaronic Ferromagnet - Synthesis and Characterization of High-Spin Organic Polymers. Journal of the American Chemical Society *116*, 8152-8161.

Appendix III: Using the "Ward lattice" for Matrix Isolated EPR Spectroscopy of a Triplet Biradical

III.1 Introduction

Matrix isolated EPR spectroscopy of biradicals is of long standing interest to the Dougherty group (Anderson et al., 1997; Jacobs et al., 1993; Silverman and Dougherty, 1993; Snyder and Dougherty, 1989). Typically simple biradicals are measured using cryogenic matrix isolated EPR spectroscopy at 4 K. However, it is not certain how relevant information obtained at 4 K in a frozen solvent is to conventional mechanistic or synthetic conditions of fluid media a room temperature. We postulated that the "Ward lattice" (See Chapters 6 and 7 for discussions of this structure) (Evans et al., 1999; Russell et al., 1994a; Russell et al., 1994b; Russell et al., 1997; Russell and Ward, 1996; Russell and Ward, 1997; Russell and Ward, 1998; Swift et al., 1998a; Swift et al., 1998b; Swift et al., 1997; Swift and Ward, 2000), might be capable of sufficiently isolating biradicals so as to allow room temperature EPR in a guanidinium sulfonate matrix.

To evaluate the potential of the "Ward lattice" as a room temperature matrix for EPR spectroscopy, we choose the well studied 2-isopropylidne-1,3-cyclopentanediyl, the "Berson biradical". The diazene precursor of the Berson biradical (**1**) is easily prepared, and photolysis of the precursor between 310 and 380 nm in a frozen matrix readily affords the biradical (**2**).

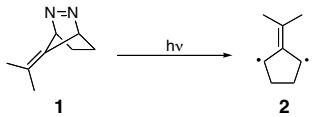

Figure III.1: Photolysis of the diazene precursor of the dimethyl Berson biradical (**1**) readily affords the biradical (**2**)

A “Ward lattice” consisting of guanidinium and 4,4’-biphenyldisulfonic acid was chosen to serve as the isolation matrix, since formation of this lattice has been observed with a variety of guest molecules. Our strategy was to first encapsulate the diazene precursor (**1**) into a guandinium 4,4’-biphenyldisulfonate matrix, followed by irradiation of this matrix to give biradical. The results of incorporation and irradiation are described here.

III.2 Results and Discusssion

The diazene (**1**) was prepared as previously described. Encapsulation in a guandinium 4.4’-Biphenyldisulfonate matrix was achieved by slow evaporation of a 2:1 methanol: water solution containing one equivalent of diazene (**1**), one equivalent 4,4’-biphenyldisulfonic acid, and two equivalents of guanidinium cabonate under argon flow. The guanidinium sulfonate matrix containing diazene was obtained as a white solid.

Photolysis of the sample was carried out in a vacuum-sealed EPR tube at 77 K. Sample photolysis between ~307 and 386 nm was performed for 25 minutes, and biradical formation was monitored by EPR spectroscopy at 77K. EPR spectra after 0, 5, and 25 minutes of photolysis are shown in Figure III.2. A small amount of biradical was observed prior to photolysis, most likely due to exposure of the sample to ambient light.

Following photolysis, the matrix encapsulated sample was allowed to warm to room temperature. A strong EPR signal persisted for the guanidium sulfonate matrix encapsulated biradial at room temperature. To confirm the triplet state of the radical, the

half field transition measured and is shown in Figure III.3. The observed half field transition is as expected for this biradical.

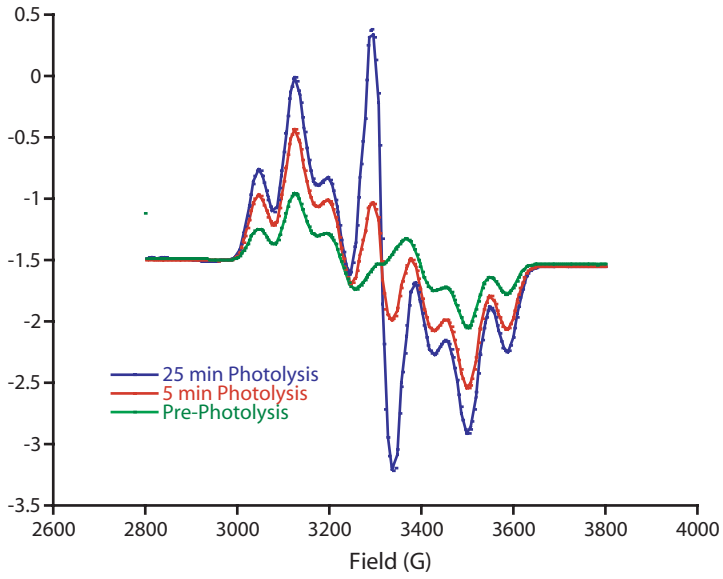

Figure III.2: Photolysis of the diazene precursor to dimethyl Berson (**1**) at 77 K in a guanidinium 4.4'-biphenyldisulfonate matrix.

The stability at room temperature and protected from light of the Berson biradical in the guanidinium 4,4'-biphenyldisulfonate matrix was monitored as a function of time. The spectra at 0, 1, 18, 67.5, 192, 355 hours are shown in Figure III.4. The observed EPR signal is stable with little to no degradation for 192 hours. Between the $_{192}$ hour time point and the 355 hour time point complete decay of the signal to pre-photolysis levels is observed. It seems likely that the rapid degradation of the signal between 192 and 355 hours resulted from a leak in the vacuum seal of the EPR tube.

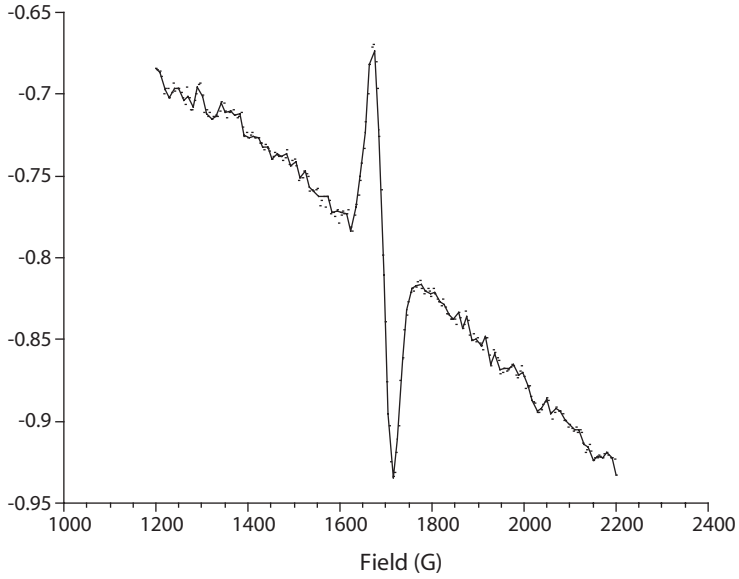

Figure III.3: Half field transition for the dimethyl Berson radical measured at room temperature in a guandinium 4,4'-biphenyldisulfonate matrix.

III.3 Conclusion

Preliminary results suggest that the "Ward lattice" is useful as a room temperature EPR matrix. Matrix encapsulation of radical precursors is trivial, photolysis of the radical precursors can be carried out in the matrix, and EPR measurements can be obtained at room temperature. The ability to study biradicals by EPR at room temperature may provide useful mechanistic information.

Photolysis of the diazene precusor (**1**) was carried out in a guanidinium sulfonate matrix, and the resulting triplet biradical was observed at 77 K and room temperature. Stability of the biradical within the matrix was determined to be at least 192 hours. Further work is needed to determine the actually decay kinetics of the biradical in the guanidinum sulfonate matrix.

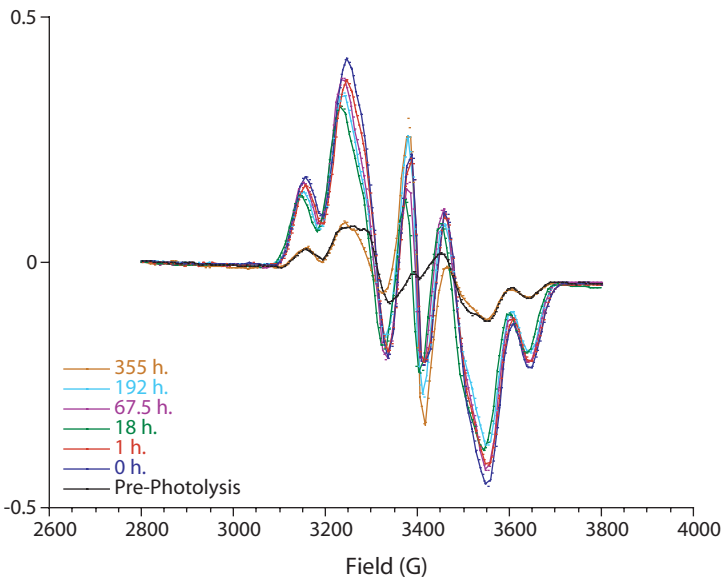

Figure III.4: EPR spectra of the dimethyl Berson radical measured at room temperature in a guandinium 4,4'-biphenyldisulfonate matrix. This series of spectra indicate that the radical is stable for at least 192 hours.

III.4 Literature Cited

Anderson, K. K., Shultz, D. A., and Dougherty, D. A. (1997). Attempted synthesis of a stable, quintet, tetraphenoxyl tetraradical: Facile rearrangement of a substituted bicyclobutane. Journal of Organic Chemistry *62*, 7575-7584.

Evans, C. C., Sukarto, L., and Ward, M. D. (1999). Sterically controlled architectural reversion in hydrogen- bonded crystalline clathrates. Journal of the American Chemical Society *121*, 320-325.

Jacobs, S. J., Shultz, D. A., Jain, R., Novak, J., and Dougherty, D. A. (1993). Evaluation of Potential Ferromagnetic Coupling Units - the Bis(Tmm) Approach to High-Spin Organic-Molecules. Journal of the American Chemical Society *115*, 1744-1753.

Russell, V. A., Etter, M. C., and Ward, M. D. (1994a). Guanidinium Parasubstituted Benzenesulfonates - Competitive Hydrogen-Bonding in Layered Structures and the Design of Nonlinear-Optical Materials. Chemistry of Materials *6*, 1206-1217.

Russell, V. A., Etter, M. C., and Ward, M. D. (1994b). Layered Materials by Molecular Design - Structural Enforcement by Hydrogen-Bonding in Guanidinium Alkanesulfonate and Arenesulfonate. Journal of the American Chemical Society *116*, 1941-1952.

Russell, V. A., Evans, C. C., Li, W. J., and Ward, M. D. (1997). Nanoporous molecular sandwiches: Pillared two-dimensional hydrogen-bonded networks with adjustable porosity. Science *276*, 575-579.

Russell, V. A., and Ward, M. D. (1996). Solid-state structure of a layered hydrogen-bonded salt: Guanidinium 5-benzoyl-4-hydroxy-2-methoxybenzenesulfonate methanol solvate. Acta Crystallographica Section B-Structural Science *52*, 209-214.

Russell, V. A., and Ward, M. D. (1997). Two-dimensional hydrogen-bonded assemblies: The influence of sterics and competitive hydrogen bonding on the structures of guanidinium arenesulfonate networks. Journal of Materials Chemistry *7*, 1123-1133.

Russell, V. A., and Ward, M. D. (1998). Interweaving of two-dimensional hydrogen-bonded networks directed by chloride ions. New Journal of Chemistry *22*, 149-153.

Silverman, S. K., and Dougherty, D. A. (1993). Conformational Effects on High-Spin Organic-Molecules. Journal of Physical Chemistry *97*, 13273-13283.

Snyder, G. J., and Dougherty, D. A. (1989). 2,4-Dimethylene-1,3-Cyclobutanediyl, the Non-Kekule Isomer of Benzene - Synthesis, Epr, and Electronic Spectroscopy. Journal of the American Chemical Society *111*, 3927-3942.

Swift, J. A., Pivovar, A. M., Reynolds, A. M., and Ward, M. D. (1998a). Template-directed architectural isomerism of open molecular frameworks: Engineering of crystalline clathrates. Journal of the American Chemical Society *120*, 5887-5894.

Swift, J. A., Reynolds, A. M., and Ward, M. D. (1998b). Cooperative host-guest recognition in crystalline clathrates: Steric guest ordering by molecular gears. Chemistry of Materials *10*, 4159-4168.

Swift, J. A., Russell, V. A., and Ward, M. D. (1997). Organoporous hosts with adjustable molecular environments. Advanced Materials *9*, 1183.

Swift, J. A., and Ward, M. D. (2000). Cooperative polar ordering of acentric guest molecules in topologically controlled host frameworks. Chemistry of Materials *12*, 1501.